Hydrogel Actuated Carbon Fiber Microelectrode Array

Oliver Chen
Michel Maharbiz, Ed.
Kristofer Pister, Ed.
Michael DeWeese, Ed.

Electrical Engineering and Computer Sciences
University of California, Berkeley

Technical Report No. UCB/EECS-2023-59
http://www2.eecs.berkeley.edu/Pubs/TechRpts/2023/EECS-2023-59.html

May 1, 2023

Acknowledgement

There have been so many colleagues, friends, and family that have played an integral part in helping me complete my academic journey.

Of course, an enormous thank you to my advisors, Michel Maharbiz, who guided me for the entirety of my PhD, and Kristofer Pister, who graciously became my co-advisor at
the tail end of my graduate program.

Thank you Michael DeWeese and Mekhail Anwar for serving on my qualification committee, and Mike again for serving on my dissertation committee as well.

To the staff at Berkeley who made my journey significantly less stressful and at times shared my burdens, thank you so much.

Most importantly, thank you to my parents, Yunyu Zhou and Liangyu Chen. You have sacrificed so much to watch me grow, and I hope I made you proud of your son.

Hydrogel Actuated Carbon Fiber Microelectrode Array

by

Oliver Chen

A dissertation submitted in partial satisfaction of the

requirements for the degree of

Doctor of Philosophy

in

Electrical Engineering and Computer Science

in the

Graduate Division

of the

University of California, Berkeley

Committee in charge:

Professor Michel M. Maharbiz, Co-chair
Professor Kristofer Pister, Co-chair
Professor Michael DeWeese

Summer 2022

Hydrogel Actuated Carbon Fiber Microelectrode Array

Abstract

Hydrogel Actuated Carbon Fiber Microelectrode Array

by

Oliver Chen

Doctor of Philosophy in Electrical Engineering and Computer Science

University of California, Berkeley

Professor Michel M. Maharbiz, Co-chair

Professor Kristofer Pister, Co-chair

Glial passivation and subsequent electrical insulation of implantable microelectrodes is a major bottleneck for long-term viability of neural probes. Self-deploying microelectrodes have been developed to minimize glial scarring and adverse biological effects near neural recording sites, but typically suffer from low electrode densities and deployment distance. In this dissertation, we propose and evaluate a large displacement, self-deploying architecture using a water absorbing hydrogel to extrude a high density carbon fiber array out of a microfabricated shuttle.

To enable mm-scale displacements, this device records electrical signals via mechanically unanchored carbon fiber microelectrodes and couples them through a physiological electrolyte to the backend metal electrodes. A hydrogel-compatible silicon microfabrication and assembly process for a high density microelectrode array is presented, and mechanical insertion into a tissue phantom is demonstrated. An equivalent circuit model and multichannel recording capability are validated using electrochemical impedance and crosstalk measurements.

This hydrogel actuation mechanism can provide sufficient force to push at least 66 fibers concurrently in one direction while achieving tissue phantom penetration depths up to 2.5 mm. The physiological electrolyte bridge used for recording marginally increases total signal path impedance up to 10%, but does not significantly affect recording capabilities nor multichannel crosstalk. This novel mechanical insertion and electrical recording architecture enables deep tissue penetration while simultaneously recording from a dense array of unanchored microelectrodes. This work proposes a mechanically and electrically robust neural probe architecture that could significantly improve microelectrode density and actuation distance of current state-of-the-art self-deploying microelectrode arrays while minimizing potential glial passivation effects.

To everyone in the future living happily with a brain implant

Contents

List of Figures

List of Tables

Acknowledgments

There have been so many colleagues, friends, and family that have played an integral part in helping me complete the capstone to my academic journey, and I hope that I can properly express my gratitude to each and every person.

Of course, an enormous thank you to my advisors, Michel Maharbiz, who guided me for the entirety of my PhD, and Kristofer Pister, who graciously became my co-advisor at the tail end of my graduate program. Michel has always encouraged me to pursue what I found interesting and meaningful, but at the same time ensured that I solved each problem in a methodical way. He gave me ample room to develop my own scientific and research intuition, and I will always treasure his approach to advising. In addition to his technical skills, Michel has a gift for motivating and inspiring others and has always made sure that I received the support I needed. Kris became my official co-advisor relatively later in my program, but certainly I have felt his influence since the beginning, taking two of his classes as well as having him on my preliminary and qualifying exam and dissertation committee. I only wish I could have joined his group earlier. I consider Kris to be no holds barred when it comes to technical feedback, and it has made me a more thoughtful and careful researcher.

Thank you Michael DeWeese and Mekhail Anwar for serving on my qualification committee, and Mike again for serving on my dissertation committee as well. You both brought such poignant thoughts to my research I had not ever considered, and your feedback is a reminder that I still have so much to learn from the biological and clinical side of this work. Interestingly, I somehow managed to get a Michael, Mekhail, and Michel all on one committee.

To my fellow Maharbytes, I thoroughly enjoyed every minute I spent with every one of you: Mauricio Bustamante, Camilo Diaz-Botia, Jordan Edmunds, Kyoungtae Lee, Wei Li, Amy Liao, Monica Lin, Bochao Lu, Travis Massey, Wentian Mi, Arda Ozilgen, David Piech, Konlin Shen, Soner Sonmezoglu, Tom Zajdel, and Alyssa Zhou. You all are such intelligent, interesting, and humble individuals, and I am so glad I had the chance to work and grow alongside you. Thank you especially to Konlin, who I learned so much from and goofed off even more with, Mauricio, who I consider to have "grown up" research-wise with, Kyoungtae, who I could depend on to be my late night buddy, and Travis, who always was ready to help at a moment's notice. To my fellow Pisterbots, I wish I could have worked alongside you for longer, but nonetheless thank you for the valuable time I got to spend with you. To the MEMS group in particular, I loved hearing about your work and keeping up with your progress, Alexander, Daniel, and Dillon.

To the staff at Berkeley who made my journey significantly less stressful and at times shared my burdens, thank you so much. To Shirley, thank you for covering for me on so many occasions and looking out for me. To Joanna, thank you for making my crazy deadlines on masks. To Ryan, thank you for your technical expertise on so many tools. To Allison, thank you for your tips and tricks I would have never known otherwise. To Rich, thank you for making me feel comfortable and welcome in lab. To Dave, thank you for always being helpful in fulfilling oddball requests.

To my friends who I consider family, thank you for supporting me since the early days, making me laugh, giving me a place to crash in my moments of need, moving apartments with me, and making the hard times bearable. I'm not sure I would have turned out fine during the pandemic without you all. I truly appreciate everything you have done for me, and I know our bond will last a lifetime.

Most importantly, thank you to my parents, Yunyu Zhou and Liangyu Chen. No words are enough to describe my appreciation. Thank you, Mom, for your patience throughout all those hours of Singapore Math/piano lessons/peewee soccer/etc., cooking delicious homemade meals, and being so dependable for so many decades. Thank you, Dad, for your undying interest in my research, terrible yet hilarious sense of humor, and endless lectures from which I somehow managed to learn a thing or two. I'm sure I have caused you lots of grief and worry, but your love, support, and honesty over the past 28 years have shaped me into who I am today as a person and researcher. You have sacrificed so much to watch me grow, and I hope I made you proud of your son.

And to the reader, thank you for joining me through my work, and I hope it helps you along your journey.

Chapter 1

Introduction

1.1 Significance of the Nervous System

Who we are, what we think, and what we do are all completely encoded by our neural cells and their connections. Our every thought and action can be attributed to some subset of neurons firing in a specific pattern [1]; essentially, we are entirely defined by our nervous systems. In fact, if we had a perfect system to record all neuronal communications with infinite spatiotemporal resolution, we might be able to unravel the deepest mysteries of the human brain, ranging from critical clinical needs such as treating Alzheimer's disease [2], epilepsy [3], sleep disorders [4], to compelling research topics like understanding why we dream [5], how we form memories [6], and human creativity and imagination [7]. What makes us human and sets us apart from other animals is indeed the power and complexity of our brains, and understanding it is and will continue to be of utmost scientific importance.

1.2 Neuronal Physiology and Activity

The central nervous system consists of the brain and the spinal cord while the peripheral nervous system consists of the nerves that branch out from them. As complex as the nervous system is, it can be broken down to individual neurons and supporting glial cells with estimates around 90 billion of each in the human brain between a 1:1 and 1:3 ratio [8], [9].

Neurons are the functional group for transmitting and receiving electrical and chemical signals in order to respond to stimuli (sensory neurons), control muscle contractions and glandular output (motor neurons), and form neural circuit connections (interneurons) [10]. Neurons are typically composed of a soma, axon, and dendrites. The soma, or the body of the neuron, contains the nucleus and is usually smaller than 20 µm in diameter [11]. The dendrites are cellular extensions which receive the majority of input for neuronal communication. The axon is a long, thin projection that can extend ten to ten thousand times the diameter of the soma in length [10] and transmits electrical signals down its length.

Electrical signals of neurons are often distinguished by frequency. High frequency (>300 Hz) electrical signals are attributed to single unit or multi-unit activity. Typically, they are be observed as action potentials or spikes characterized by rapid polarization and depolarization of the cell membrane with frequency content centered around 1 kHz. The peak-to-peak amplitude across the membrane can reach over 100 mV during an action potential, but has an amplitude of less than 1 mV (usually 10s-100s μm) when measured strictly extracellularly due to the smaller change in ion concentration outside the cell compared to inside [12]. Though smaller in amplitude, extracellular recordings are more common than intracellular recordings due to the difficulty in precisely piercing the cell membrane without damaging the cell or altering its function. These single/multi-unit signals fall off quickly with distance from the neuron soma ($\frac{1}{r^n}$) where $1 < n < 2$, so these high frequency signals can be pinpointed to a single neuron in the best case scenarios [1], [12]. While high frequency content is useful for closed-loop feedback systems for neural interfaces, the tradeoff is the invasiveness of recording electrodes that must be placed either on top of the cortex or intracortically.

Low frequency (<300 Hz) extracellular signals are local field potentials (LFPs) that contain a volumetric averaging of groups of neurons. The relative locality of LFPs is still debated as estimates range from 200-400 μm to cm and mm distances [13]. This makes differentiating specific single unit activity of an individual neuron impossible, but still contain useful information regarding various neural processes including indexing events causal to action potentials and information transfer across neural circuits [14]. One major advantage of low frequency recordings is that electrodes are not necessarily implanted intracortically; in fact, electroencephalograms can be used to record LFPs from the scalp or other external areas of the head.

The major glial cells consist of microglia, astrocytes and oligodendrocytes [15]. Originally, these cells were considered to have little to no function outside of “gluing” neurons together, but now have been discovered to have a wide range of essential cellular functions. Microglia are the phagocytic cells that respond to brain or blood brain barrier (BBB) injury that also have been shown to be significant in synaptic pruning [16]. Astrocytes, the most abundant fraction of glia, carry out an extremely wide variety of physiological functions including K^+ buffering, control of extracellular pH, uptake of neurotransmitters like glutamate, control of cerebral blood flow, and water transport [17]. Oligodendrocytes are the myelinating cells that enable motor function and other critical functions. When severe loss of myelination occurs, motor dysfunction, ataxia, weight loss, and seizures can develop [15].

The electrical potentials generated by neurons which contain clinically and physiologically useful information may be supressed by glial responses to invasive implanted devices, as we will discuss in section 1.5.

1.3 Central Nervous System Brain-Machine Interface

A brain-machine interface (BMI) is a communication system for the central nervous system to interact with the environment without the use of use of peripheral nerves and muscles [18].

There are many modalities for recording neural activity such as electrical, magnetic, optical, and chemical sensors; however, we will focus on electrical recording and stimulation. BMIs can relay thoughts and intentions to external devices for use as speech assistance and neural prosthetics in order to restore function to patients disabled by neuromuscular disorders like stroke, cerebral palsy, and spinal cord damage [19].

A full BMI learns neural patterns and translates them into clinically relevant information in five stages: signal acquisition, preprocessing, feature extraction, classification, and control interfacing [20]. During signal acquisition, dedicated hardware collects raw neural data to send to later stages of the BMI. The preprocessing stage performs rough signal processing like noise reduction or artifact removal. The feature extraction stage identifies certain pieces of significant information. During classification, the features in the data are mapped to physiologically relevant intentions known as pattern recognition. Finally, these signals are translated into real world commands to control an external device. In the past few decades, BMIs have become more complex, demonstrating neurological controls of computer cursors, robotic arms, prostheses, and other devices [21], [22] (Fig. 1.1).

We will focus on the signal acquisition stage of a BMI and the hardware sensors used to acquire and measure neural signals. At the most basic level, a neural probe measuring electrical signals consists of a conducting electrode to sense changes in potential in the immediate vicinity. These signals are then typically “shorted” to an amplifier through the electrode to increase their amplitude for further processing. As discussed earlier, recording parameters like signal frequency and spatial resolution can inform necessary electrode geometries and placement.

For example, if only LFPs are needed, electrodes can be placed outside of the brain and skull on the skin (electroencephalography–EEG). These tissue layers separating the neurons, which act as dipoles or higher-order n-poles, from the electrodes act as a spatially averaging low-pass filter [24] and sample the local area near each electrode. These electrodes are external to the body and non-invasive, but also are fairly large, up to centimeters in

Table 1.1: Types of Central Nervous System Cells

Type	**Sub-Type**	**Function**
Neuron	Sensory Neuron	Respond to stimuli
	Motor Neuron	Control muscle contractions and glandular output
	Interneuron	Form neural circuits
Microglia	Microglia	Phagocytosis of foreign material
Macroglia	Astrocyte	Homeostasis and blood-brain barrier formation
	Oligodendrocyte	Myelin sheath formation

Figure 1.1: Human clinical patient operating a cursor on a screen using cortical control through an implanted multielectrode array. *Reproduced from [23] with permission.*

diameter (Fig. 1.2). Though they have high temporal resolution, EEGs suffer from low spatial resolution and are insufficient for complicated tasks that require many degrees of freedom [25].

Electrocorticography (ECoG) is used to monitor LFP signals as well from the cortex by placing electrodes directly on the brain (Fig. 1.3). These devices provide higher spatiotemportal resolution with a higher degree of accuracy than EEGs simply due to their proximity with the tissue. These two dimensional grids of electrodes are much smaller than their EEG counterparts since they are implanted into the skull and consequently have larger signal amplitudes from fewer neurons. Though a craniotomy is needed, inserting an ECoG array is minimally invasive while still offering high enough resolution for medical BMI applications like decoding muscle activation from neural activity [25], [27]. ECoG electrodes are typically arrayed much closer together than EEGs electrodes due to limited size constraints and also are much smaller as well (typically mms in diameter and pitch for ECoG and 10s to 100s μm for μECoG) [28], [29]. Though ECoG arrays can typically only record LFPS, μECoG arrays with their smaller electrode sizes are capable of recording spikes [30], [31].

Intracortical neural probes are the most invasive implanted device with the potential for the highest spatial resolution compared to EEG and ECoG. Because these electrodes

Figure 1.2: Lab based electroencephalogram used for measuring neural activity from the scalp with metal electrodes. *Reproduced from [26] with permission.*

are implanted within the cortex itself, they must be as small as possible while maintaining recording efficacy. If the electrodes are large, they will not only displace their same volume of tissue, but also lose recording specificity. Therefore, intracortical electrodes must be placed within 150 μm of a neuron to detect appreciable potential fluctuations and within 50 μm to separate individual neural signals [1]. Typically, these electrodes are 10s of μm in diameter. The various device architectures are described in more detail in section 1.7.

To summarize, the closer the electrodes are to the neurons they record from, the higher the spatiotemporal resolution. Intracortical neural probes typically demonstrate the highest resolution, followed by ECoG, and finally EEG. Higher resolution also closely correlates with ability to record higher frequency content, but at the cost of surgical invasiveness. To further increase resolution, electrode size and pitch can be scaled down as well which leads to other engineering tradeoffs that will be discussed later.

1.4 Abiotic Failure Modes

At this point, it is critical to note that recording from large arrays of hundred or thousand channel devices is not only an engineering challenge, but also introduces biological obstacles that can drastically impact recording efficacy. The ideal intracortical neural probe would have an infinite implant lifetime without causing damage to the surrounding tissue or degrad-

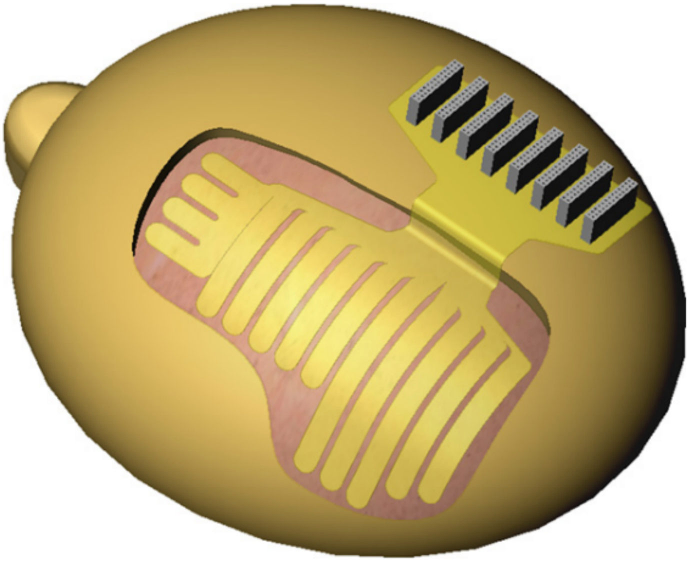

Figure 1.3: Schematic diagram of electrocorticogram device with array placed on the cortex after the skull has been removed. *Reproduced from [32] with permission.*

ing itself since the frequency of surgical procedures to implant/remove/maintain the implant should be minimized. Explantation or further surgeries to correct a faulty probe carry non-trivial risks to the patient. Unfortunately, the implant itself can affect tissue behavior and health and vice versa, and efforts to reduce adverse biological responses to implants have become a central research topic in the field of BMIs and neuroscience.

To achieve clinical translation with therapeutically-relevant lifetimes, implantable neural probes must address a variety of abiotic and biotic failure mode. Abiotic failures are caused by device damage usually due to the harsh biological environment and include corrosion, lead/connector damage, and bulk packaging failure [33]. Catastrophic corrosion usually first occurs at exposed metal areas when a formation of a galvanic pair causes a small potential difference between the two. This chemical reaction takes place more rapidly for a distinct pair with different metals, but can also occur between identical metals due to local variability in field potential across the device substrate [34]. This phenomenon not only reduces the conductivity and recording efficacy of the metal electrode, but can also produces toxic metal compounds dissolved in the surrounding cerebrospinal fluid (CSF).

Lead damage is observed most often in wired or tethered percutaneous devices. In order to extract raw or preprocessed neural data, the most straightforward method is to connect each channel directly or through a multiplexer to external computing devices via conducting wires. These wires protrude from layers of tissues and can create routes for infection, requiring constant position adjustment or explantation in the most severe cases [35]. Wires themselves have a finite mechanical lifetime as repeated stressing or bending can cause fracture as well.

Delamination of the encapsulation layers of implanted devices must also be considered due to deterioration of the adhesion layer on the substrate. This happens either through water diffusion through the encapsulation layer or via cracking/pinholing and undermines the adhesion mechanism, peeling the outermost layer(s) off [36].

1.5 Biotic Failure Modes

Biotic failure modes result from tissue reactions to an implanted neural probe that cause reduced recording efficacy or shortened recording lifetimes. Acute damage occurs during implantation via vascular damage due to volumetric tissue displacement, causing a foreign body response to isolate the implant and protect vulnerable nearby tissue. This response is complex, but most importantly consists of activated microglia releasing proinflammatory cytokines which causes neural death and degeneration at the implantation site [37].

For neural probes, the chronic tissue response is actually more detrimental to recording function compared to the acute response. Probes can show good quality recordings for a few days to weeks before degradation occurs [9], [38]. This degradation occurs over time (2-6 week formation time and steady state 3-6 months post-implantation) as reactive astrocytes form a diffusion barrier around the implant, referred to as a the glial sheath or glial scar [39], [40], [41], [9] (Fig. 1.4). The thickness of the scar is variable depending on the size, geometry, and material of the implant, but is generally between 25-200 μm [42], [43]. Furthermore, constant relative micromotion on the order of 10s of μm caused by respiration, blood pressure fluctuations, and general movement between the implant and the surrounding tissue can cause chronic inflammatory responses when the implant is anchored to the skull or not free-floating in the brain [44], [45], [46].

This glial scar is associated with reduced recording quality, and various underlying mechanisms have been proposed. After acute damage caused by implantation, neurogenesis in immediate proximity to the implantation site is blocked by the reactive astrocytes preventing axon regeneration causing secondary tissue damage [47], [48]. In addition, when presented with a large surface area foreign object, neurogenesis is discouraged as cells are unable to attach themselves to these smooth structures [49], [50]. Furthermore, protein adsorption onto electrode sites and corrosion of metals causes increases in electrode impedance while can reduce the signal-to-noise of the recording device [9]. This increased impedance induces higher voltages or currents for current-controlled and voltage-controlled stimulation architectures, respectively, which can also damage nearby tissue and create a positive feedback cycle.

1.6 Implant Design Affects Gliosis

Many physical properties of implanted devices can exacerbate the magnitude of gliosis such as probe substrate material, size, geometry, and coating. Stiff substrates like silicon or

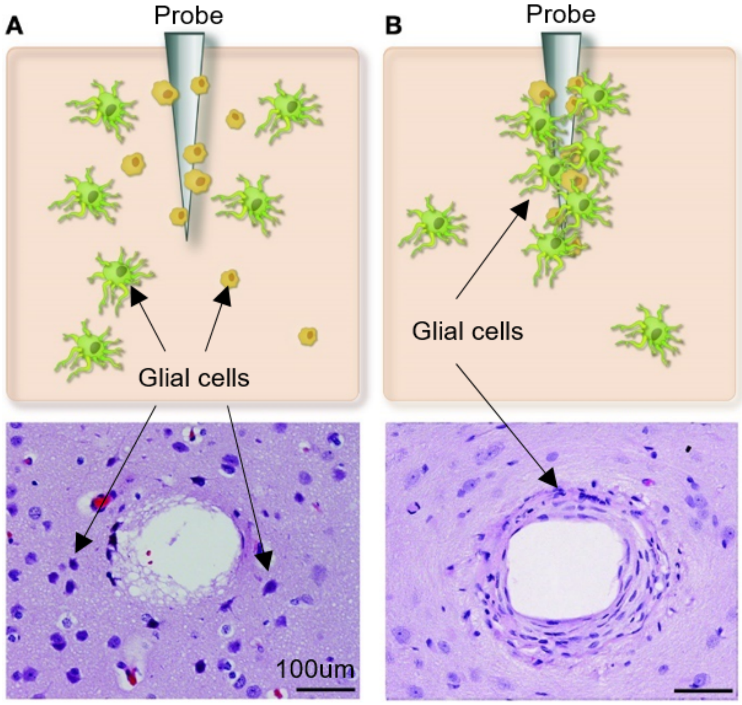

Figure 1.4: a) Initial glial response immediately after implantation of probe with glial cells gathering near site. b) Chronic glial response showing dense scar formation around probe as glial cells congregate near foreign object. *Adapted from [42] with permission.*

polyurethane are orders of magnitude less compliant than brain tissue when comparing Young's modulus (10^2, 10^1, 10^-5 GPa, respectively) [51] (Fig. 1.5). Both microglial cells and astrocytes which play a large role in the foreign body response show mechanosensitivity like differing phenotypes and morphologies, increasing inflammatory response, microglia growth and proliferation, and antigen presentation when grown on polyacrylamide substrates with higher stiffness [52]. Mechanically adaptive materials that are inserted while stiff and then become compliant after implantation show significantly less scarring and inflammation [53], [54], [55].

Total bending stiffness is not just determined by substrate material, but also geometry as well. In fact, because bending stiffness is proportional to Et^3 where t is the thickness of the cross-section of the implant, compliance can be increased more rapidly with decreasing size rather than material. In addition, if the implant size is significantly reduced, smaller volumes of tissue will be displaced, less vasculature will be damaged, and a reduced inflammatory response will occur. It seems that probes with subcellular dimensions elicit little to no gliosis for this reason, and it is additionally postulated that microglia cannot attach to foreign bodies when this size scale [56], [57]. This ties in closely with probe geometry as

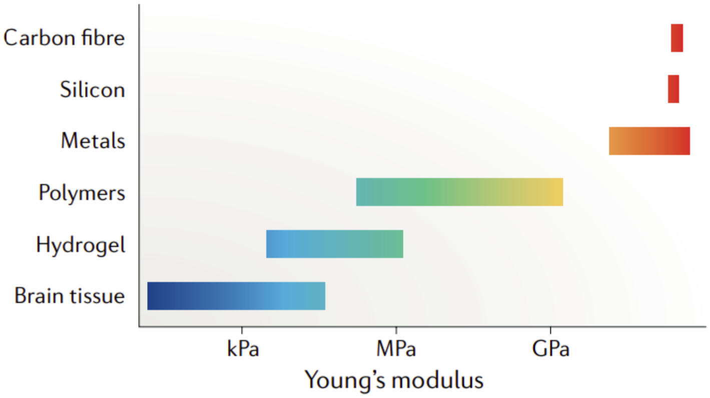

Figure 1.5: Range of Young's moduli of various materials used in neural implants and microelectrodes compared to neural tissue. *Reproduced from [11] with permission.*

well. Increased neuronal density and reduced gliosis occurs near lattice structures in silicon penetrating probes compared to a solid body silicon probe [50]. Combining smaller, softer substrates with well-informed design can have a significant effect on reducing the foreign body response.

In order to aid implantation of soft substrate probes to achieve less inflammatory response, certain types of dissolvable coatings are used. These coatings which include polyethylene glycol (PEG), poly(lactide-co-glycolide) (PGLA), polycarbonates, and biodegradable silk polymers, are rigid and stiff during surgical insertion into tissue to prevent buckling, but quickly dissolve and are reabsorbed minutes or hours afterwards [58], [59], [60], [61]. This allows the implanted substrate to have a high compliance to match the surrounding tissue as closely as possible in the long-term by temporarily increasing total stiffness only during the short-term. Other coatings are used to explicitly reduce foreign body response through controlled delivery of anti-inflammatory therapeutics like hydrogel silk, bioactive anti-inflammatory surface molecules, and biodegradable polymer nanoparticles [62], [63], [64], [65], [66], [67], [68], [69].

Yet another parameter that can be tuned to reduce gliosis is probe insertion speed. The exact mechanism for this phenomenon is still not completely understood, but arguments supporting slow insertion speed include minimal vibration/mechanical shock and tissue accomodating compression and stretching [70]. Slow insertion speeds lead to less dimpling during penetration and small penetration forces at all stages of insertion [71]. Typically, minimum insertion speeds float around 10 µm/s, typical speeds are around 100s of µm/s to a few mm/s, and the fastest are pneumatic inserters at 10s of µm/s. The lower bound of insertion speeds are limited by the need to complete insertion within the surgical window so generally even slower speeds have not been investigated.

1.7 Intracortical Neural Probes

Modern intracortical neural probes follow several main architectures: microwire arrays, silicon-based arrays, flexible substrate arrays, and ultrasmall microelectrodes.

A microwire embodies the simplest and one of the oldest types of intracortical probes. A conductive wire usually made from tungsten around 20-100 μm in diameter is insulated and the tip is cut to reveal an small cross-section of exposed area for recording [72], [73]. Several microwires can be bundled together to form a polytrode, and the most common configuration is a tetrode due to its ability to triangulate neural signals to identify single neuron activity [74]. However, a microwire can only record local activity at its tip, and increasing the number of recording sites requires the same number of wires. These bundles are generally stiff and large, causing gliosis after implantation.

Complementary metal oxide semiconductor (CMOS) microfabrication techniques like lithography, deposition, etching, and oxidation were adapted for microelectromechanical systems (MEMS) fabrication to develop silicon substrate neural probes. The utilization of these techniques enabled unprecedented microelectrode density, consistency in fabrication across an array and batches of arrays, unique substrate shapes, and integration with backened electronics. The two most prominent architectures are the Michigan probe developed at the University of Michigan [75], [76] and the Utah array developed at the University of Utah [77].

The Michigan array at its simplest is a silicon substrate for mechanical support with insulated, patterned, conductive traces wire bonded to any off-chip electronics [78] (Fig. 1.6). The recording sites can be between a few μm to 10s of μm in diameter with traces about the same width, and the pitch between recording sites is around 10s of μm. The silicon shank is typically less than 100 μm thick and a few hundred μm wide. These arrays have the advantage of being dense and monolithically fabricated without the need for tedious and difficult assembly that microwire arrays require. More recent designs continue to be iterated upon with new features like optogenetic, microfluidic, and drug eluting capabilities [79], [80], [81].

The Utah array is another silicon substrate probe composed of a two dimensional grid of long conductive needles pointing out of plane of the substrate (Fig. 1.7). These mm long needles are usually less than 100 μm in diameter with several hundred μm pitch. The tips of the exposed needles are metallized, and the signal is routed through the conductive doped silicon needles. Again, the advantage of this design is its monolithic fabrication and ease for backend integration. The drawbacks of the Utah array are its large electrode diameters and pitches compared to the Michigan array. However, the Utah array was the first neural probe to be approved for human use under FDA Investigational Device Exemption and Institutional Review Board approvals [82], [83], [84].

However, due to their high Young's modulus and large implant footprint, silicon probes tend to elicit major gliosis [86]. High substrate compliancy and subcellular size are desirable for reducing gliosis and extending recording lifetime, but silicon probes are rigid and supercellular. Hence, another genre of probe design used to mitigate adverse biological reactions

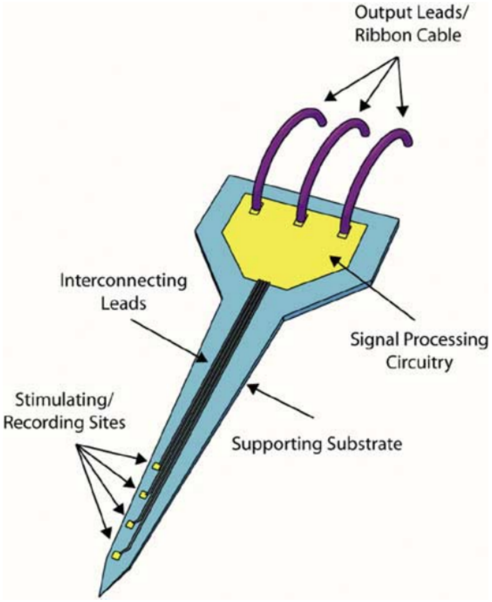

Figure 1.6: Diagram of silicon based Michigan probe architecture. *Reproduced from [78] with permission.*

has been the flexible substrate probe. The goal of these types of probes is to use materials that approach the Young's modulus of tissue as closely as possible to mimic their mechanical properties. Popular substrate materials that have been investigated include parylene, SU-8, and polyimide that are several hundred μm wide, 10-30 μm thick, and several mm long. Though these probe materials are much more compliant than silicon, they still remain about 100,000 times stiffer than brain tissue. Other concerns include delamination from and water diffusion through the substrate, polymer swelling, and insertion aid requirements [86]. As a whole, flexible substrate probes have encouraged the field of neural probes to move toward more biocompatible materials and design.

A related research thrust to flexible implants are ultrasmall implants with the same goal of reducing gliosis and adverse biological reactions. One popular architecture is the carbon fiber microelectrode array (CFMEA) in which electrically conductive (2 kΩ/mm), mechanically robust, and chemically inert carbon fibers less than 10 μm in diameter are used as recording microelectrodes similar to the larger microwire [87] (Fig. 1.8). Though polyacrylonitrile-based carbon fibers actually have a large Young's modulus of 200-280 GPa, the total bending stiffnesses are less than those of microwires due to their exceedingly small diameter. Carbon fiber arrays have been shown to elicit little to no gliosis due to their small subcellular diameters [88]. Other ultrasmall architectures include mesh electronics [89], [90], hong2018mesh and neuron-like microelectrodes [90] that combine ultrasmall microelectrodes with neuronal integration.

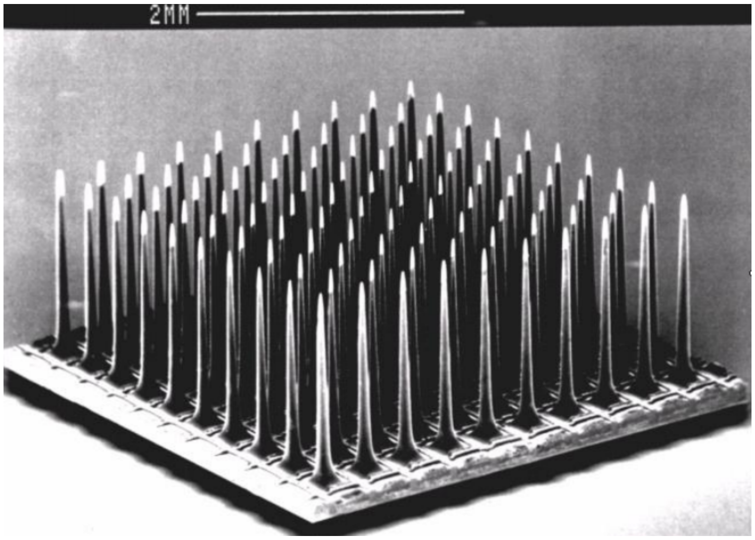

Figure 1.7: Scanning electron micrograph of Utah architecture recording array. *Reproduced from [85] with permission.*

When the progress and development of next-generation intracortical neural probes are viewed chronologically, it becomes exceedingly obvious that the major neural probe engineering milestones have shifted toward biological integration and biocompatibility.

1.8 Microelectrode Actuation Mechanisms

While most neural probes are inserted into brain tissue during the surgical implantation with the microelectrodes set permanently in place, a subset of them utilized mechanisms to deploy the recording features away from the substrate toward the targeted neural tissue. Self-deploying electrodes can benefit from being much smaller or more flexible than the substrate/shuttle from which they are initially integrated and are designed to reduce the glial response at the specific location of the microelectrode. In addition, self-deploying microelectrodes based on MEMS actuation can take place post-implantation allowing for controllable and much slower tissue penetration speeds.

One example is a silicon spring actuation mechanism where microelectrodes are patterned onto the tips of microsprings [91] (Fig. 1.9). The springs are preloaded by encasing them in a dried gel, and after insertion into tissue, the gel dissolves and allows the springs to push outward away from the shuttle (orthogonal to the initial implantation direction). This mechanism allows for monolithic fabrication and passive actuation, but suffers from low microelectrode density, limited actuation distance, and unnecessary displacement of tissue by the leading side of the spring.

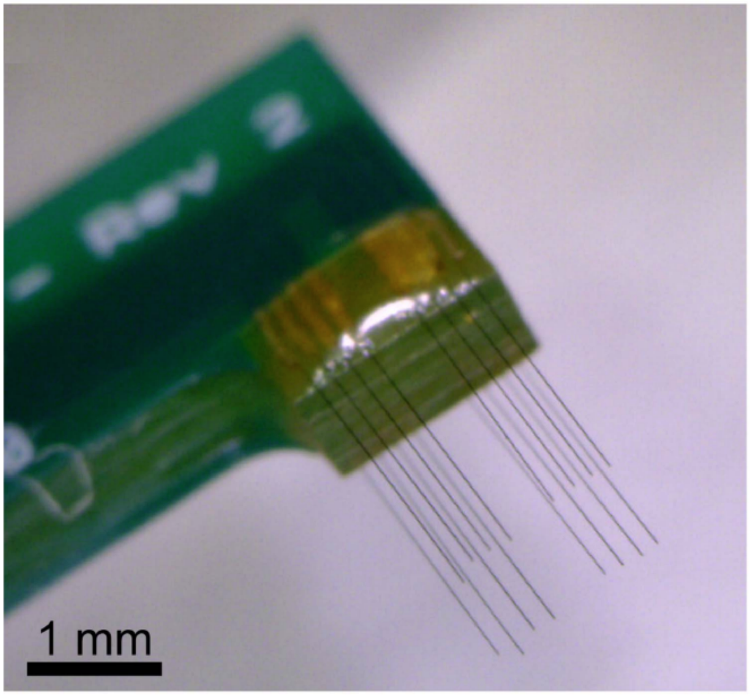

Figure 1.8: 16 channel carbon fiber microelectrode array with fiber microelectrode adhered to a printed circuit board with silver epoxy. *Reproduced from [88] with permission.*

Another slow and passive actuation mechanism is a shape memory polymer where chemically crosslinked materials deform when transitioning over a temperature range [92] (Fig. 1.10). The device is heated and pre-deformed prior to implantation and slowly returns back to the initial non-stressed shape over the course of hours to days depending on the material and geometry, allowing self-deployment parallel to the initial insertion direction. This method also suffers from limited microelectrode density and actuation force fallout after a few hundred microns.

An active actuation method that has been demonstrated is the gap closing inchworm motor that can insert carbon fiber microelectrodes into brain tissue phantom [93] (Fig. 1.11). This method can generate relatively large actuation forces with easily controllable and variable speeds. However, MEMS inchworm motors run on high voltages that can be significantly larger than the water window and require large chip areas for the gap closing actuators.

Another active actuation method is an electrolysis-based inflatable parylene balloon where a liquid is electrolyzed to create an expanding gas that provides actuation force to insert a silicon probe [94]. This method requires much less electric current and power, but is limited to a small actuation distance of a few microns while expanding significantly more in lateral directions not contributing to insertion.

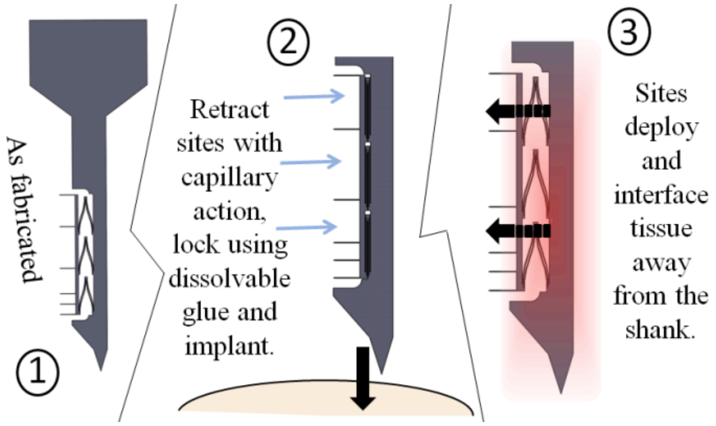

Figure 1.9: Silicon shank with spring feature initially retracted and held in place by a dissolvable gel that releases after implantation. *Reproduced from [91] with permission.*

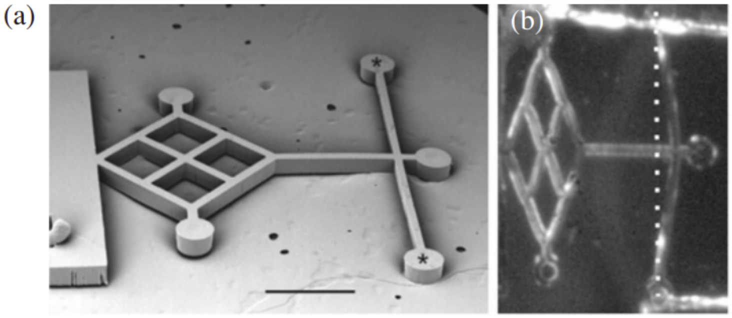

Figure 1.10: a) Scanning electron micrograph of shape memory polymer neural probe. b) Light micrograph of restored probe at 37°C. *Reproduced from [92] with permission.*

1.9 Hydrogel MEMS Actuation

Finally, a common material class used for in variety of biomedical devices which thus far has not been investigated as an actuation source for self-deploying neural probes is the hydrogel. Hydrogels are three-dimensional hydrophilic polymers that can absorb large amounts of water and maintain their polymer structure and integrity [95]. They can experience volumetric increases approximately 100-1000 fold [96], determined chiefly by their hydrophilicity. Hydrogels have been mainstays in many biological applications like contact lenses [97], drug delivery [98], tissue scaffolds [99], and even as a soft coating for neural probes [100].

Due to their swelling nature, hydrogels have been used as actuators for a number of non-neural applications. While smart hydrogels can control their actuation based on external changes in temperature, pH, light, chemicals, and current, they all uptake water to expand

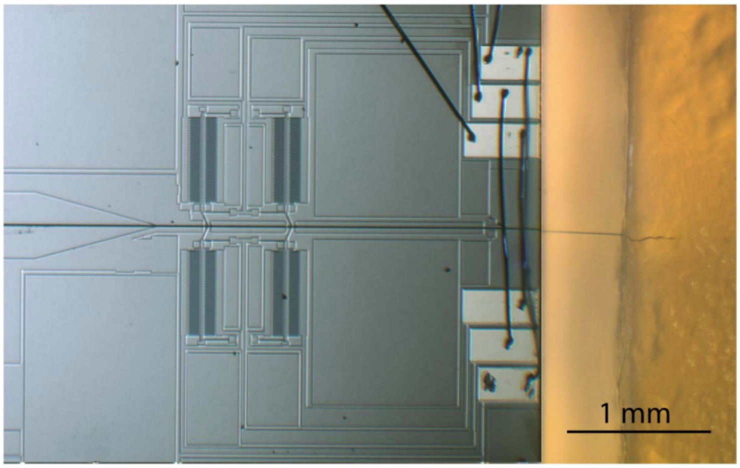

Figure 1.11: Electrostatic MEMS inchworm actuator inserting a carbon fiber into brain phantom. *Reproduced from [93] with permission.*

and produce force [101]. Though still in the proof-of-concept stage, hydrogel actuators have been used as grippers [102], [103], walkers [104], swimmers [105], artificial muscles [106], Artificial muscular microfibers: hydrogel with high speed tunable electroactivity], and valves [107], [108]. These actuation methods can generate nearly 100 kPa of force depending on the chemical and hydrogel dimensions [109] which can exceed the necessary penetration force of fractions of a mN for deployable microelectrodes. Given that these scales of force are possible, naturally hydrogels seem like an attractive and feasible actuation mechanism for neural probes [110]. They can utilize the abundant liquid surrounding the human brain (CSF) for slow post-implantation actuation and have been demonstrated to be biocompatible.

1.10 Thesis Organization

The primary goal of this work is to demonstrate a novel actuation mechanism for deployable microelectrodes that has the potential for ultrahigh density neural recordings and mm-scale displacements. Along the way, we will discover these desirable actuation parameters require an innovative recording architecture including a physical break in the metal interconnect.

Chapter 2 lays out the project goals and gives an overview of the device design that can achieve these goals. It will also briefly discuss the design considerations of major components of the device.

Chapter 3 discusses the microfabrication and fabrication process flow for the silicon shuttle of the probe, piston head, and carbon fiber insulation. In addition, it will show the assembly process to complete an implantation-ready carbon fiber microelectrode array.

Chapter 4 discusses the exploratory paths taken to find a wafer-scale microfabrication compatible process to integrate hydrogels into the device.

Chapter 5 presents methods to model the electrical impedance of the device as well as the minimum lower bound actuation force. This includes the complete electrical circuit equivalent model for the device's novel signal path and important leakage paths. It will also present the concepts of intrachannel and interchannel impedances that affect recording quality and adjacent channel crosstalk. In addition, a model to estimate the lower bound actuation force of the hydrogel during expansion will be presented.

Chapter 6 presents impedance and crosstalk data for the novel device architecture as well as mechanical actuation data for tissue phantom penetration.

Chapter 7 will summarize the novelties and achievements of this project, limitations, and future directions for investigation.

Chapter 2

Device Overview

2.1 Goals of This Work

The overarching goal of this work is to implement an intracortical neural probe capable of probing through the glial scar formed by chronic inflammation and tissue damage to increase the longevity of its electrical recording microelectrodes. This top-level goal can be broken down into several sub-goals:

1. Submicron microelectrode sizes: electrodes themselves will elicit little to no gliosis
2. Self-deploying microelectrodes: regardless of implant shuttle geometry and material properties, electrodes can be positioned away from local inflammation zone to avoid insulating effects of gliosis
3. Passive actuation mechanism for microelectrode deployment: reduce complexity of device and eliminate electrical power consumption to avoid heating/electrical harm
4. Large actuation displacement of multiple microelectrodes: supports penetration depths through entire cortex or distant areas from the initial implantation site
5. Slow deployment speeds: reduce vasculature and tissue damage compared to high speed insertions
6. High microelectrode density: maximize spatial resolution for recording

When considering the various architectures of neural probes listed in Chapter 1, no individual neural probe is designed to accomplish all of these goals simultaneously. Silicon probes chiefly suffer from large implant size and stiffness which fail to solve sub-goals 2 and 4. Carbon fiber microelectrode arrays typically have low microelectrode density without self-deploying electrodes which fail to solve sub-goals 4 and 6. MEMS actuated probes tend to suffer from large electrode size and low actuation distance which fail to solve sub-goals 1, 4, and 6.

To achieve these goals, the device architectures of silicon shuttle neural probes, carbon fiber microelectrode arrays, and MEMS actuated probes are integrated. This work proposes that the sub-goals be met by the following design choices:

1. Carbon fiber microelectrodes with diameters <10um
2. MEMS actuation mechanisms
3. Passive hydrogel actuation source
4. Hydrogel material with high swelling capabilities
5. Controllable deployment and low force output
6. Deployment of fibers from micropatterned channels with micron-scale pitch

2.2 Critical Architectural Concepts

Though these ideas will be further elaborated on in future chapters, it is worth noting from a high-level perspective how specific design choices can address these sub-goals. By using micropatterned channels in a silicon shuttle to store submicron sized carbon fiber microelectrodes, a high microelectrode density can be achieved. In fact, the potential spacing between adjacent channels can be patterned down to the lithographic limit if desired, an advantage over traditional carbon fiber arrays. To actuate the fibers out of the shuttle into surrounding tissue for recording, a swelling hydrogel inside the silicon shuttle that absorbs extracellular cerebrospinal fluid (CSF) can provide the driving force need to push the fibers out of the shuttle into the surrounding tissue. This deployment speed is dependent to the hydrogel volumetric swelling rate; the slower the hydrogel expands, the slower the fibers will be pushed out of the device. Furthermore, this swelling actuation force is completely passive and requires no external electrical power. To achieve large actuation distances, the volumetric increase of the hydrogel inside the shuttle must be considerable as well.

The ultimate goal is to actuate the fibers far enough to position the recording tip of the fiber outside of the region of glial scarring which inevitably occurs due to the implantation of the silicon shuttle. This device concept is shown in Fig. 2.1.

Because the necessary actuation distance can be up to hundreds of microns due to the glial scar thickness, the design of an interconnect from the tissue-facing carbon fiber to the backend electronics is not so straightforward. Typically, carbon fibers are not monolithically fabricated onto the substrate like silicon springs or actuating polymers, but rather mounted manually after substrate fabrication/preparation. Some type of conductive epoxy is used to adhere the fibers to the substrate in this case. However, mechanically anchoring the fibers prevents them from being deployed from the substrate. Hence, it seems that a conductive interconnect and self-deploying fiber microelectrodes are incompatible design features.

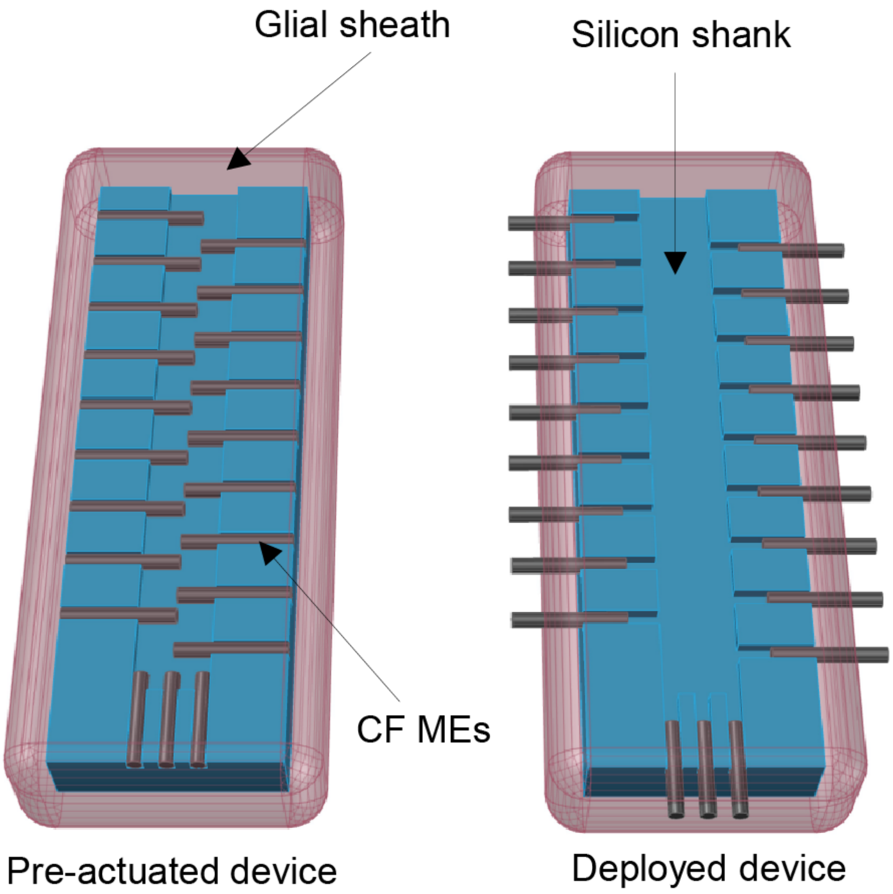

Figure 2.1: Cartoon of carbon fiber microelectrode array with pre-actuated device on left and deployed device state on right where carbon fiber microelectrodes (CF ME) pushed beyond region of glial scarring.

However, if the conductive interconnect between a fiber and metal electrode patterned on the shuttle substrate is liquid rather than solid, a fiber could be displaced large distances and still be electrically coupled to a nearby electrode. The extracellular CSF surrounding every cell that is used to expand the hydrogel is also an electrolyte capable of conducting electrical signals. If an electrolyte bridge can be maintained as a coupling medium, the fiber can be freely actuated by the hydrogel. This simultaneously permits high actuation distance of microelectrodes and electrical recording.

2.3 Device Architecture and Operation

As mentioned previously, this neural probe is composed of a microfabricated silicon shuttle that houses an array of carbon fiber microelectrodes that are actuated into surrounding neural tissue after implantation of the shuttle. The device architecture is shown in Fig. 2.2 with major components depicted.

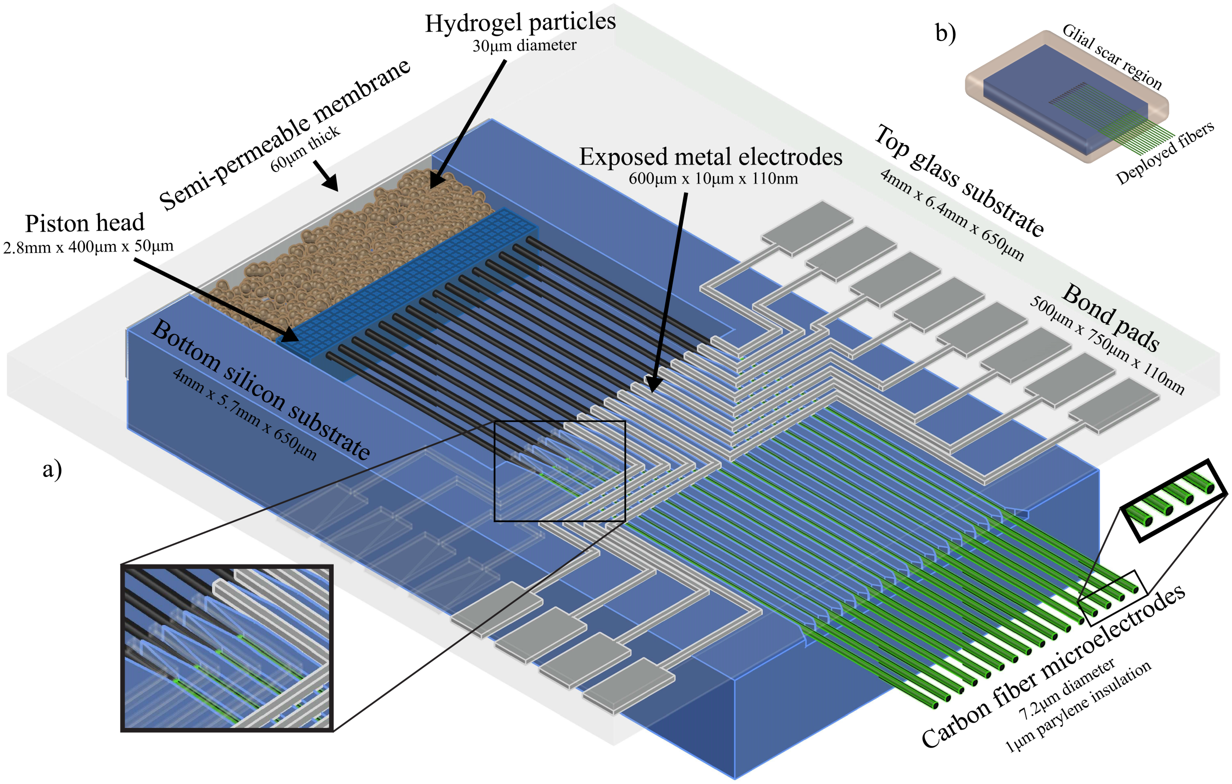

Figure 2.2: a) Cartoon of carbon fiber microelectrode array with fibers partially deployed. The top four left-hand side metal electrodes are transparent for visualization purposes. Bottom left inset: metal electrodes positioned over exposed section of fiber in each channel. Bottom right inset: parylene coated fiber cross-sections exposed. b) Simplified cartoon of device with fibers deployed beyond glial scar.

The two major parts of the device include the mechanical deployment backend and the electrical recording front end. The mechanical backend provides the actuation force needed to deploy the carbon fiber microelectrodes into the surrounding tissue. Desirable characteristics of the mechanical backend include:

- Large actuation distance – horizontal penetration beyond glial scar or vertical penetration through entire cortical thickness

- High actuation force – overcome initial penetration force and tissue shear forces
- Slow/controllable deployment speed – minimize tissue damage
- High efficiency – reduce initial volume of hydrogel needed

The mechanical actuation mechanism consists of a semi-permeable membrane, hydrogel, piston head, and an array of carbon fibers. When immersed in CSF, the device allows the electrolyte to permeate through the membrane to hydrate and expand the hydrogel. The membrane also prevents the hydrogel from escaping out of the device and keep the direction of hydrogel expansion constrained toward the mobile silicon piston head. In turn, the piston head transfers the expansion force and displacement to the fibers which are actuated out from the silicon shuttle and into the surrounding tissue. As the hydrogel expansion continues over the course of hours, the piston head is gradually pushed forward inside the chamber within the shuttle, and segments of the fibers are protruding out of the silicon shuttle. Once the expansion process has finished, the fibers are in their final positions and ready for long-term recording.

The electrical front end allows the device to record from neural tissue by coupling the electrical potential fluctuations to external electronics connected to the device. Desirable characteristics of the electrical front end include:

- Low intrachannel impedance – maximize signal amplitude by minimizing voltage drops over series impedances
- High interchannel impedance/low crosstalk – minimize signals coupling from one channel to adjacent channels
- High parasitic impedance – maximize signal amplitude by reducing current leakage

The electrical signal path consists of a carbon fiber with an insulating coating, a metal electrode patterned on the shuttle substrate, and CSF electrolyte bridge between them to couple the signal. After actuation is complete, an electrical signal is detected by the exposed tissue-facing end of the fiber, travels along fiber to the exposed distal end, coupled through a thin layer of CSF between the fiber and metal electrode, and finally reaches the substrate electrode inside the shuttle (Fig. 2.3). CSF enters the channel that the fiber resides in due to capillary force and bridges the exposed segment of the distal end of the fiber to the metal electrode patterned onto the device substrate. The maximum thickness of CSF layer is limited by the dimensions of the channel and the total diameter of the insulated carbon fiber.

These major structural components are summarized in Table 2.1.

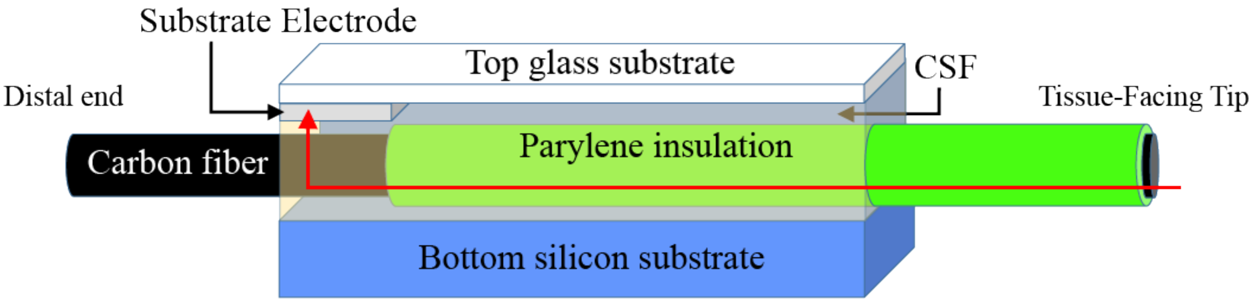

Figure 2.3: Cartoon of aCSF electrolyte bridge inside a single channel with the electrical signal path labelled in red. The tissue-facing exposed end senses a potential change, transmits it down the length of the insulated fiber to the exposed distal end. The aCSF residing in the channel couples the signal from the fiber to the metal electrode for recording. There are EEIs at the surface of the metal electrode, the distal end of the fiber (left end), and exposed tip of the fiber (right end). The gap between the carbon fiber and substrate electrode is $<1\mu$m.

2.4 Component Specific Considerations

In order to maximize the mechanical and electrical performance of the device, each component are carefully designed and implemented. This subsection will briefly discuss the important considerations for every major component.

The semi-permeable membrane acts as both an osmotic membrane to pass the electrolyte solution, CSF, into the device as well as a mechanical stop to prevent the hydrogel and other internal components from leaving the chamber. The biocompatible membrane should be hydrophilic in order to promote wetting to its surface and micro- or nano-porous to act as a selective sieve. At the very least, because the hydrogel is immediately inside the membrane, it's pore size much be at least be smaller than diameter of the hydrogel. With these considerations, a 0.2 µm pore size aluminum oxide membrane was used.

The hydrogel is the source of actuation force to deploy the carbon fiber microelectrodes from the silicon shuttle. When choosing a hydrogel for microelectrode actuation, volumetric size increase, osmotic force output, biocompatibility, particle size, and possible microfabrication compatibility are all essential to consider. Ideally, the hydrogel should have a large swelling ratio from its dry to expanded states to reduce the initial volume needed for device size considerations. In addition, the osmotic force that a hydrogel can generate can be variable, as various materials will be able to support different external loads. If a hydrogel can expand rapidly without a load, but fails to expand appreciably with a load, it is not compatible with this device design. In order to minimize device size, hydrogel particle size should also be as small as possible (micron-scale). For this work, with these considerations, 30 µm diameter sodium polyacrylate hydrogel particles were used.

The chamber inside the silicon shuttle is patterned into the silicon substrate and contains the hydrogel, piston head, and excess length of carbon fibers. The minimum depth of the chamber should be large enough to accommodate at least one layer of fully expanded hydrogel particles, but when accounting for particle volume variability, the chamber depth should be slightly deeper. The length of the chamber is set by the volume of hydrogel inserted, width of the piston head, and maximum actuation distance of the fibers. Likely, the limiting factor will be the actuation distance of the fibers since the chamber needs to initially contain this excess length inside the shuttle during implantation. For this work, a nominal chamber depth of 55 μm, length of 4 mm, and width of 3 mm were used.

The channels inside the silicon shuttle are patterned into the silicon substrate, house the carbon fibers, and constrain the deployment direction of the fibers. The channel must be patterned and etched in such a way to minimize the internal spacing between the fiber and its walls. This ensures two essential phenomena occur. First, when the gap between the fibers and channel walls are sufficiently small, capillary force will be very high which forces CSF from the surrounding tissue into the channels. This CSF is used as the coupling electrolyte. Second, because this CSF is conductive, its impedance along the length of the channel should be maximized to prevent current leakage through this thin sheath of electrolyte parallel to the fiber/channel. Hence, if the fibers have a diameter of n μm, the channel width and depth should be $n+\epsilon$ μm where ϵ approaches 0. In addition, the length of the channel should be as long as possible as this increases this leakage impedance. However, there is a design tradeoff

Table 2.1: Functional Components of Hydrogel CFMEA

Mechanical Components	**Function**
Semi-permeable membrane	Osmotic membrane to pass aCSF
Hydrogel	Absorbs aCSF to generate actuation force
Piston head	Harness hydrogel expansion force
Chamber	Dimensions set hydrogel expansion distance
Channels	Draw aCSF to fiber-electrode interface
Carbon fibers	Actuated into surrounding tissue phantom
Glass substrate	Transparent lid

Electrical Components	**Function**
Carbon fibers	Insulated tissue-facing microelectrodes
aCSF	Electrolyte shorting fiber to substrate electrode
Metal electrode	Trace routed to backend electronics

between channel length/impedance and device size that must be considered. For this work, a nominal channel depth and width of 10 µm, length of 2.5 mm, and pitch of 110 µm was used.

The carbon fibers are used as the tissue-facing microelectrodes to conduct electrical signals for recording. They are involved in both the mechanical actuation as well as electrical recording. The dimensions of the fiber are determined by the desired actuation/penetration depth into tissue and avoidance of buckling. If the fibers are too long and thin, they will buckle when penetration is attempted. In addition, the fibers are conductive along their entire length so they must be selectively insulated to maintain recording specificity. The fibers are coated with parylene-C as a chemically stable dielectric and then exposed at the front tip (just a cross-section exposed) and distal end (mm-scale length exposed). This allows the tip of the fiber to be conductive at the tissue and along the segment near the metal electrodes in the shuttle. To decrease the electrochemical impedance of the fibers and electrolyte, the fibers were electroplated with a conductive polymer, poly(3,4-ethylenedioxythiophene) polystyrene sulfonate (PEDOT:PSS) to increase the effective surface area. For this work, 7.2 µm carbon fibers with varying lengths and a 1 µm thick parylene-C layer were used.

The bonded top glass and bottom silicon substrates are used as the shuttle to implant the carbon fiber microelectrodes and other internal components. The fused silica glass substrate was chosen for its optical transparency as the lid of the device in order to characterize the internal processes and compatibility with microfabrication tool contamination protocols. The silicon substrate was chosen for its compatibility with standard microfabrication processes and future CMOS integration. For this work, a 150mm diameter, 650 µm thick silicon wafer and 150 mm diameter, 500 µm fused silica wafer were used.

The electrolyte solution (CSF) is used to couple the fibers and metal electrodes for recording. Instead of physiological CSF, an artificial cerebrospinal fluid (aCSF) composed of 120 mM sodium chloride and 26 mM sodium bicarbonate solution. This aCSF formula was used due to its similarity to the ionic concentrations in physiological CSF in order to closely replicate its conductivity and electrical properties.

The metal electrodes and traces patterned on the bottom face of the glass substrate is used to pass the neural signal to any backend electronics for recording/signal processing. Because the metal electrode will come into contact with extracellular fluid, it will be subjected to potentially corrosive chemicals. Thus, the outermost layer of any metal stack must be a metal particularly resistant to corrosion to limit cytotoxicity and neurodegeneration. In addition, as will be discussed in more detail in Chapter 4, this metal electrode should have a large surface area compared to the cross-sectional exposed area of the fiber tip. In this work, a metal stack of 10 nm titanium and 100nm of platinum was used as the metal electrodes and traces.

Table 2.2: Component Sources

Major Component	**Company**	**Description**
Semi-permeable membrane	Sterlitech Corp.	Aluminum Oxide Membrane Filters, 0.2 Micron, 47mm
Hydrogel	Newstone International Corp.	Newsorb ST-500MPS, 30 μm diameter
Silica beads	Sigma-Aldrich, Inc.	10 μm diameter, monodisperse silica
Carbon fibers	Asbury Carbons Inc.	AGM94CF1000, 7.2 μm diameter
Silicon wafer	UniversityWafer, Inc.	P-type, 1-100 Ω-cm, 650 μm thick, 150mm diameter
Glass wafer	UniversityWafer, Inc.	Fused silica, 500 μm thick, 150 mm diameter
Silicon-on-insulator wafer	UniversityWafer, Inc.	N-type, 6.5 Ω-cm, 50 μm thick device layer, 2 μm thick oxide layer, 573 μm thick handle layer, 150 mm diameter
UV cure epoxy	Epoxy Technology Inc.	OG116-31, medical grade epoxy
Silver epoxy	M. G. Chemicals	8331D, two part thermal cure epoxy
Silicone adhesive	J-B Weld Co.	NCB 31310, all purpose silicone RTV adhesive
PEDOT:PSS	Sigma-Aldrich, Inc.	Poly(sodium 4-styrenesulfonate) (CAS No. 25704-18-1) and 3,4-ethylenedioxythiophene (CAS No. 126213-50-1)

Chapter 3

Microfabrication and Assembly

3.1 Microfabrication of Shuttle

Microfabrication of the shuttle included the silicon substrate, glass substrate, and wafer bonding. Microfabricating the silicon substrate was a two-mask process. The first mask defined the channel etch pattern, and the second mask defined the chamber etch. Microfabricating the glass wafer was also a two-mask process. The first mask defined the metal layer for the patterned electrodes and routing traces, and the second mask defined the etch through the passivation layer on top of the electrodes. A set of microfabrication masks for a representative device is shown in Fig. 3.1. The full microfabrication processes described below were performed at the Marvell Nanofabrication Laboratory, and the process parameters are described in more detail in Appendix A.

The glass wafer fabrication is shown in Fig. 3.2(i)-(iv). The fused silica wafer was cleaned in a piranha bath for 10 minutes to remove organic residues and particulates. Then, a 1 µm lift-off resist layer (LOR 5A, Kayaku Advanced Materials, Westborough, MA, USA) was spun on (SVG 8626 Coater, ASML, Veldhoven, Netherlands), and soft baked to remove excess solvents in the resist. The lift-off resist was used to form a layered step structure with subsequent photoresist layers to prevent sidewall coverage in subsequent metal evaporation steps. A 2 µm i-line photoresist layer (MiR 701, MicroChemicals GmbH, Ulm, Germany) was spun on and soft baked (PCT-200 CRS, PicoTrack, Santa Clara, USA). The i-line photoresist was exposed in a contact aligner (SUSS MA-6, SUSS MicroTec Group, Garching, Germany). It then received a post-exposure bake and was puddle developed (MICROPOSIT MF-26A, Kayaku Advanced Materials, Westborough, MA, USA). Any photoresist residue is removed in an O_2 descum process (PE II-A, Technic, Cranston, Rhode Island, USA) to improve metal adhesion to the substrate. A final hard bake was done to prepare the photoresist for further processing by fully cross-linking the photoresist to improve etching selectivity.

Afterwards, 10 nm/100 nm titanium (Ti)/platinum (Pt) layers were evaporated consecutively using an electron beam to form 10 µm wide electrode and traces on the substrate (Solution Process Development System, CHA Industries, Fremont, CA, USA) shown in Fig.

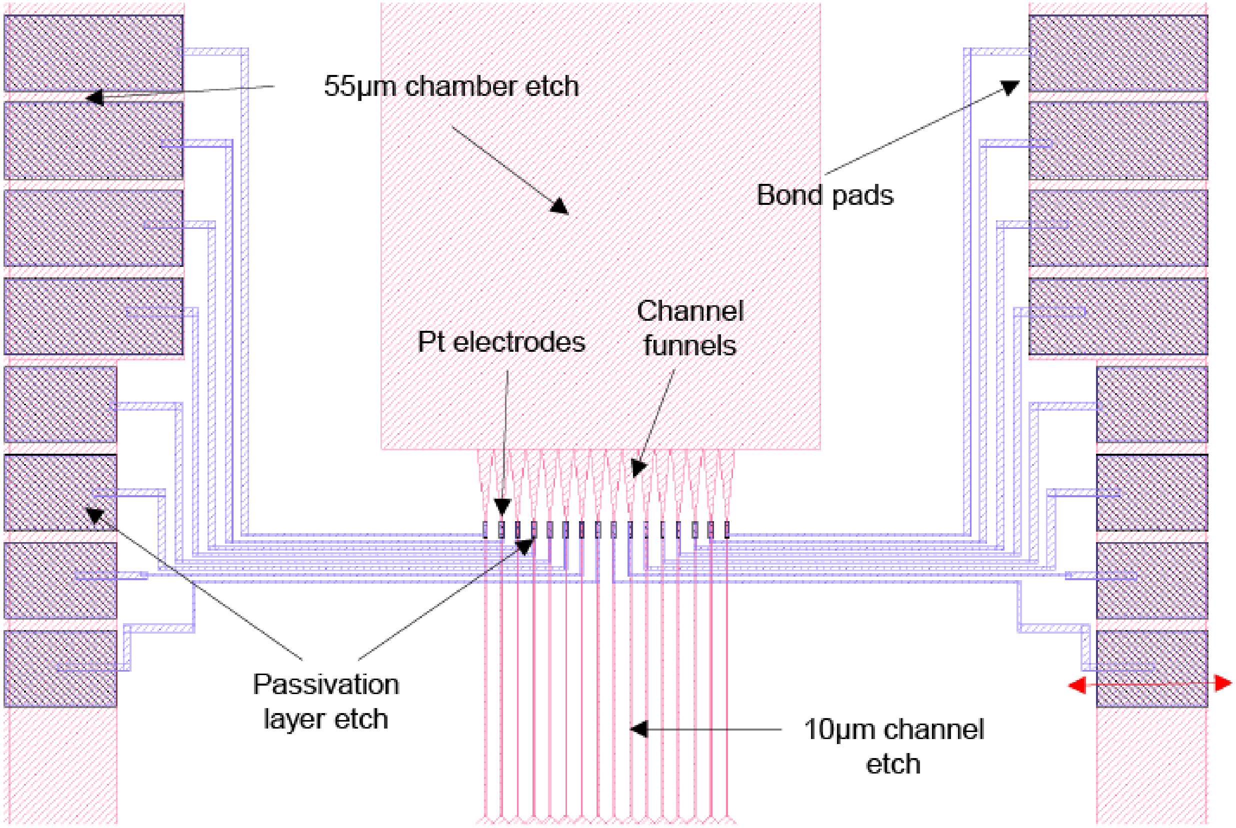

Figure 3.1: Layout of representative device. Chamber, channels, and channel funnels etched into silicon substrate, shown in red. Metallized traces, electrodes, and bond pads deposited on glass substrate, shown in blue. Silicon dioxide passivation layer etch holes on glass substrate, shown in black.

3.2(i). The Ti was used as an adhesion layer, and Pt was used as the chemically inert electrodes/traces. A lift-off process was used to remove the resist layers and excess metal (M6100, ASAP Co., Ltd., Saitama, Japan).

A 1 µm layer of plasma enhanced chemical vapor deposition (PECVD) silicon dioxide (Plasmalab 80plus, Oxford Instruments Plasma Technology, Bristol, United Kingdom) was deposited to form a passivation layer for the metallized traces shown in Fig. 3.2(ii). To planarize the wafer, chemical-mechanical polishing (POLI-500 DC Chemical-Mechanical Polisher, Beijing TSD Semiconductor Co., Beijing, China) was used to leave a subsequent thin film layer 200 nm thick shown in Fig. 3.2(iii). At this point, the substrate had 60-70 nm diameter silica nanoparticles embedded in the top film layer as a result of the polishing measured with an atomic force microscope (NX-20 AFM, Park Systems, Suwon, South Korea) shown in Fig. 3.3. To reduce surface roughness, a 5 second HF dip was performed to quickly etch silica particles while protecting the substrate and silicon dioxide film from excess etching (Fig. 3.2(iii)). Without this step, local topology would prevent local wafer bonding near the particles. The PECVD SiO_2 was patterned using i-line photoresist and etched (PK-12 RIE, Plasma-Therm, St. Petersburg, FL, USA) using an anisotropic reactive ion etch (RIE) to expose the metal electrodes (600 µm × 10 µm) for recording shown in Fig. 3.2(iv).

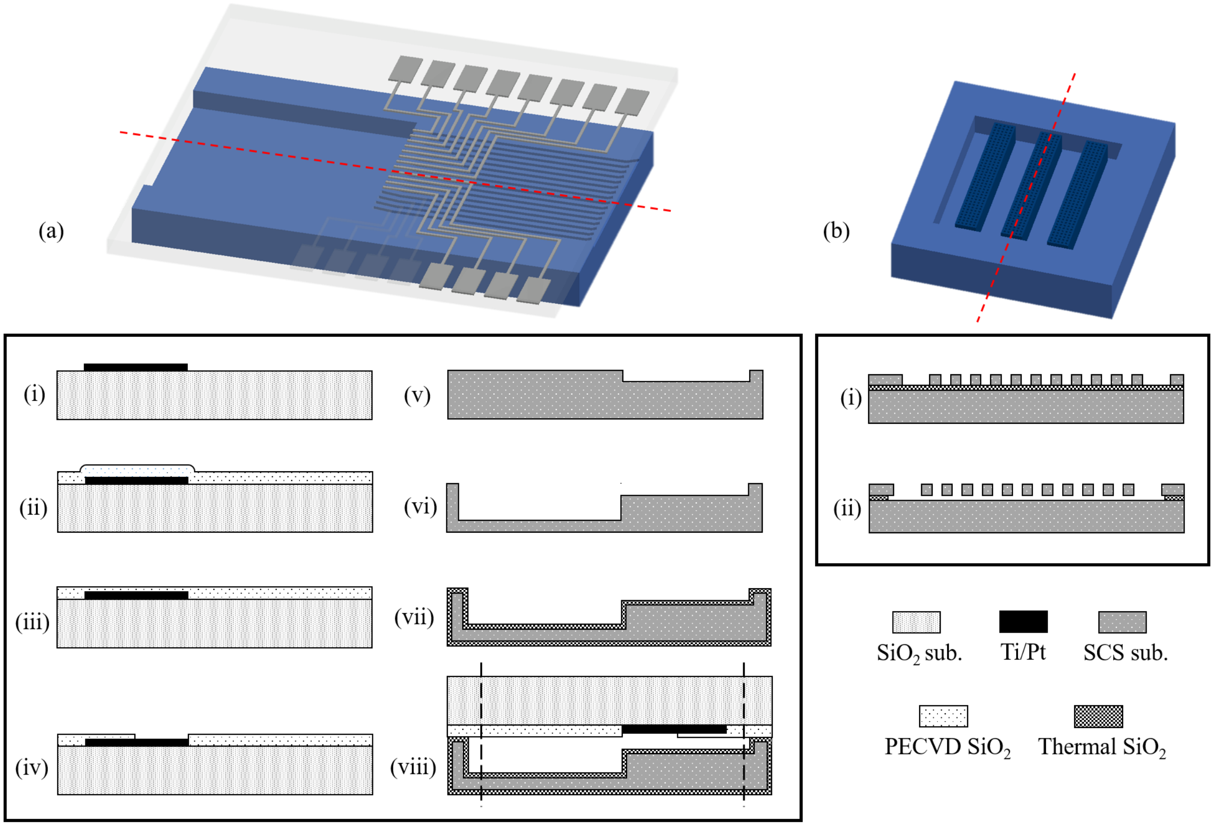

Figure 3.2: (a) Cross-section of hydrogel CFMEA process flow using two substrate wafer bonding along red dashed line. Glass substrate processing shown in (i) - (iv), silicon substrate processing shown in (v) - (vii), wafer bonding shown in (viii). (b) Cross-section of piston head process flow along red dashed line. Black dashed indicators represent dicing lines to open the channel and chamber for post-fabrication insertion of carbon fibers, piston head, and hydrogel.

The patterning of the silicon substrate is depicted in Fig. 3.2(v)-(viii). After the wafer cleaning step described previously, a layer of 2 µm PECVD silicon dioxide was deposited as a hard mask (Plasmalab 80plus, Oxford Instruments Plasma Technology, Bristol, United Kingdom). An 8 µm of positive photoresist (AZ P4620, MicroChemicals, Ulm, Germany)

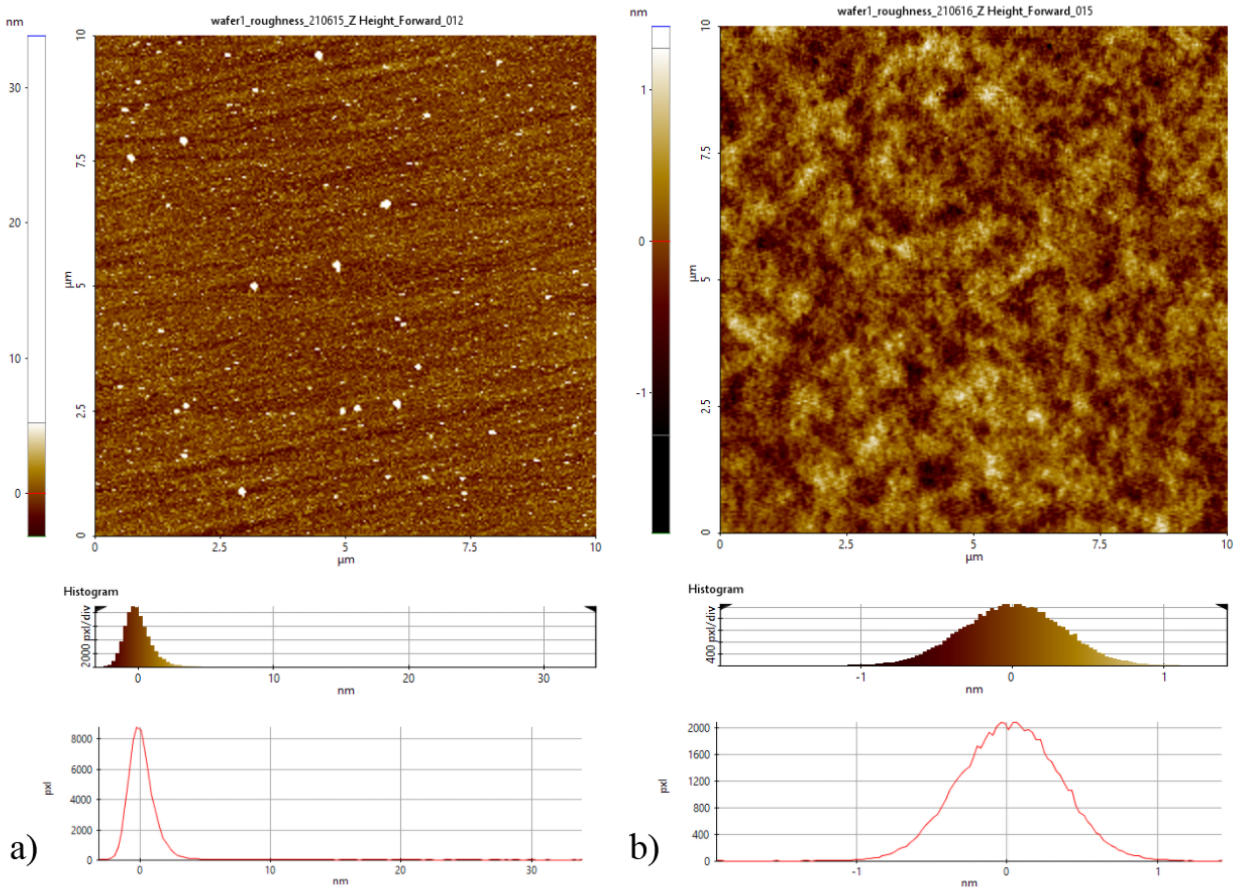

Figure 3.3: (a) Surface roughness after simple piranha clean showing silica particles on wafer surface. (b) Surface roughness after 5 second HF dip showing no silica particles on wafer surface.

was spun on and soft baked. It was exposed using a contact aligner. The photoresist was puddle developed and hard baked.

Following the lithography process, the underlying PECVD oxide was anistropically etched using a CHF_3 plasma (Surface Technology Systems Advanced Planar Source Oxide Etch System, SPTS Technologies, Newport, United Kingdom). Using this SiO_2 mask, the silicon substrate was etched using deep reactive ion etching (DRIE) in an inductively coupled plasma (Surface Technology Systems Advanced Silicon Etch, SPTS Technologies, Newport, United Kingdom) to form the final channel depth of 10 µm, width of 10 µm, and length of 2.5 mm with 110 µm pitch between channels shown in Fig. 3.2(v). The photoresist was stripped (MICROPOSIT Remover 1165, Kayaku Advanced Materials, Westborough, MA, USA), and the wafer cleaned of organic material and oxide using the previous piranha wafer cleaning process and a 2 minute hydrofluoric acid (HF) dip. This lithography, etching (55 cycles), and cleaning was repeated to etch the 55 μm deep, 4 mm long, 3 mm wide chamber as well shown in Fig. 3.2(vi). Finally, a 2 μm wet thermal silicon dioxide layer was grown for electrical insulation (Tytan Standard Series, Tystar Corporation, Garden Grove, CA, USA) as shown in Fig. 3.2(vii).

In preparation for wafer bonding, both the silicon and glass wafers were cleaned in the piranha bath before being spun dry. The direct bonding (AWB 08, Applied Microengineering Ltd., Didcot, Oxfordshire, United Kingdom) step is shown in Fig. 3.2(viii). An anneal step was completed to strengthen the bond. Finally, the bonded devices were singulated (DAD3240, Disco Corporation, Tokyo, Japan) into individual chips. Two additional cuts were needed to access the channels and chamber of the device for post-fabrication assembly. Finally, two partial vertical cuts through just the silicon substrate were done to expose the bond pads for wire bonding.

3.2 Microfabrication of Piston Head

Fabrication of the silicon piston heads from a silicon-on-insulator (SOI) wafer with a 50 μm device and 2 μm buried oxide layer is shown in Fig. 3.2b. The device layer thickness was chosen such that the final piston head thickness is smaller than the chamber depth but large enough to prevent the fiber from slipping over or under the piston head during actuation. The device layer was patterned and etched using the lithography and DRIE process (55 cycles) used for the silicon substrate to form a 2.8 mm long, 400 μm wide, and 50 μm thick piston head with 10 μm × 100 μm etch holes shown in Fig. 3.2(i). Before etching the buried oxide layer, the wafer was baked at 250°C for 2 minutes to remove adsorbed polymers from the surface of the wafer box. The underlying oxide layer was removed using an isotropic vapor HF etch (Primaxx uEtch, SPTS Technologies, Newport, United Kingdom) shown in Fig. 3.2(ii). The etch cycles lengths should be at least 5 minutes to stabilize etch rates during each cycle. The final piston heads were broken off the handle wafer manually for final device assembly.

3.3 Carbon Fiber Insulation, Exposure, and Electroplating

The 7.2 μm diameter carbon fibers (Asbury Carbons, Asbury, NJ, USA) were insulated with a 1 μm thick layer of conformal CVD parylene-C (SCS Labcoter 2, Specialty Coating Systems, Indianapolis, IN, USA). Rows of carbon fiber are placed side-by-side on two parallel strips of Kapton tape. One end of the fibers are adhered to one strip of tape and the other end on the other strip with a majority of their lengths not adhered or covered by the tape. When removed from the tape, a large segment of the fibers are coated with the dielectric and ready for exposure. Parylene-C is known for its chemical inertness as a dielectric and is pinhole-free when thicker than 100 nm [111], [112].

In order to finely manipulate a single 7.2 μm diameter carbon fibers, a 2.4 μm radius probe tip (PTT-24-25, Cascade Microtech, Beaverton, OR, USA) was coated with a thin layer of cured silicone adhesive (Clear All Purpose RTV Silicone, J-B Weld, Sulphur Springs, TX, USA) and mounted on a micromanipulator. The fibers adhered well enough to the silicone coated probe tip to be lifted, but detached easily when a small external force was applied. Without the silicone, simply using a bare probe tip could not generate adhesion to pick up even a single fiber.

To expose the cross-section of each parylene insulated fiber tip, the fiber was inserted into a dummy device chip channel with a short segment protruding outside the device. The protruding segment was broken off using a probe tip, leaving the cross-section exposed without stripping any parylene insulation. This method is preferred when considering cutting fibers with a blade or scissors always damages the insulating coating on the fiber. Then, the parylene insulation of a 2 mm portion of the opposite end of the fiber was pyrolyzed with a small flame to expose the distal segment as well. This allowed the distal segment of the fiber to be exposed right below the metal electrode in each chamber. Care must be taken to prevent excessive heat from reaching the fibers. Otherwise, the flame can sharpen the fiber and alter its dimensions and brittleness.

The fibers and metal electrodes in the shuttle were then electroplated with PEDOT:PSS in order to reduce the impedance of the signal path. After parylene insulation and exposure, each fiber was adhered (Fig. 3.4) to a printed circuit board (PCB) pad using conductive silver epoxy (8331D, M. G. Chemicals, Ontario, Canada). The exposed fiber tips were immersed in a 0.02 M poly(sodium 4-styrenesulfonate) and 0.01 M 3,4-ethylenedioxythiophene solution (Sigma-Aldrich, Inc., St. Louis, MO, USA) and electroplated at a 1 μA DC current using the NanoZ (Plexon Inc., Dallas, TX, USA) until the impedance reached 800 kΩ or less. Then, the entire length of the fibers were immersed in the plating solution and plated again to coat the exposed distal end of the fibers until the impedance reached 10 kΩ or less. After plating, the fibers are bent until fracture where they were adhered to remove them from the PCB. The distal ends and tissue-facing tips of uncoated and PEDOT:PSS coated fibers are shown in Fig. 3.5 and Fig. 3.6.

3.4 Device Assembly

The major steps of the post-fabrication assembly included insertion of the hydrogel, membrane, and fibers into the silicon shuttle.

After insulating and exposing the carbon fibers, the entire device was assembled. Using the precision of the micromanipulator, each electroplated fiber was sequentially inserted into a different channel, and the probe tip was removed in an orthogonal direction to the channel to keep the fiber in its channel while detaching from the silicone. After the fibers were inserted sequentially into the 16 channels, the silicon piston head was picked up using the same silicone coated probe tip and guided into the chamber opening created from the dicing line (Fig. 3.7). Because the opening is just 55 μm, a 50 μm thick piece of polyethylene

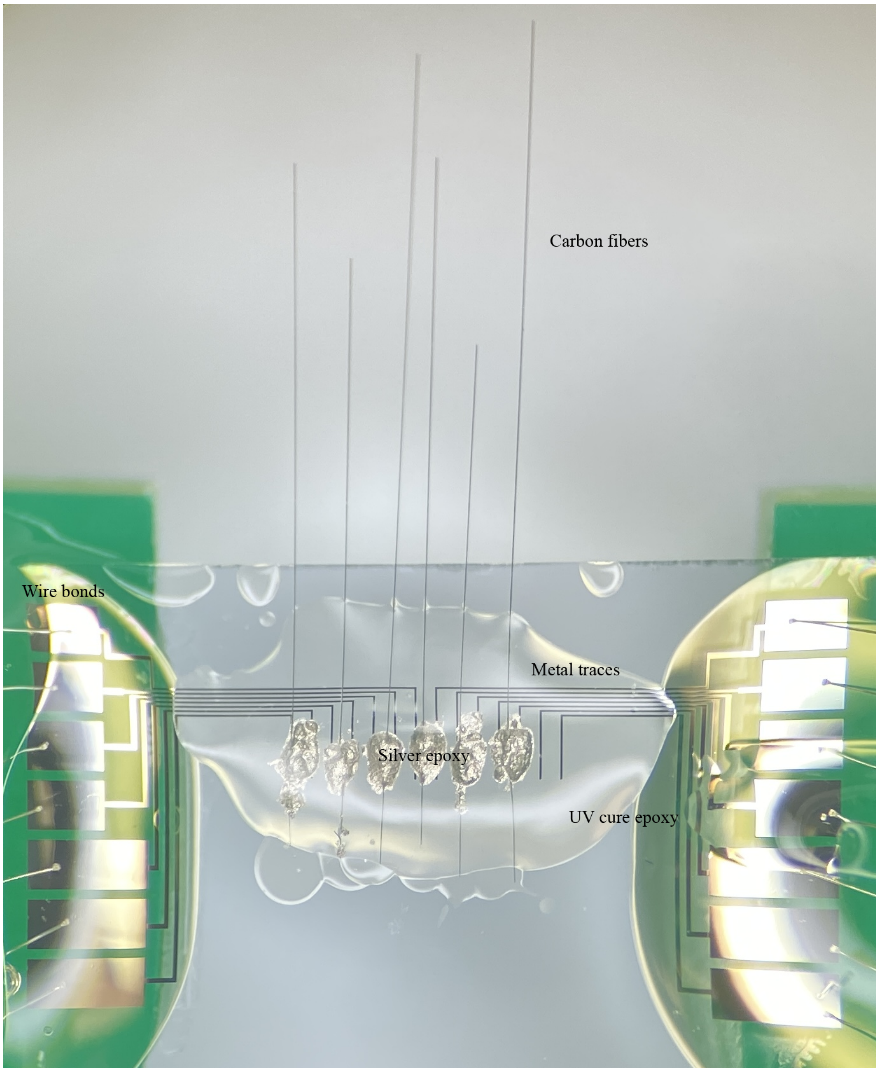

Figure 3.4: Fibers are shorted to PCB pads via microfabricated breakout board and silver epoxy. UV cure epoxy is used to electrically insulate the traces and silver epoxy.

terephthalate (PET) film was used to gently push the piston head deeper into the chamber until it was in contact with all fibers.

Once the piston head is in position, the hydrogel was inserted into the chamber. Because the chamber etch is 55 µm deep, the diameter of each hydrogel bead must be, at largest, slightly smaller than the chamber depth. For this reason, commercially available off-the-shelf 30 µm sodium polyacrylate hydrogel beads (Newsorb ST-500MPS, Newstone International, Tokyo, Japan) were used. The beads were placed at the chamber opening and then pushed into the chamber using a bare probe tip in a process similar to doctor blading. This is

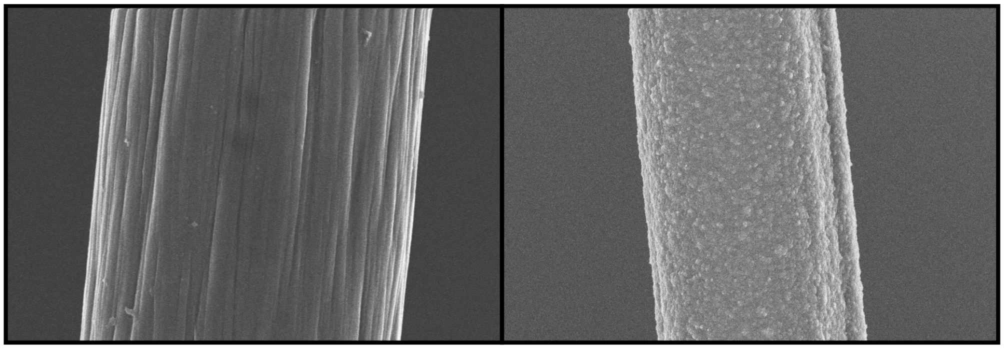

Figure 3.5: Scanning electron microscope (SEM) image of exposed cross-section of 7.2 μm carbon fiber with 1 μm parylene-c insulation layer. Left: bare fiber without PEDOT:PSS coating imaged at 5 kV and 11.2 mm working distance. Right: PEDOT:PSS coated fiber imaged at 5 kV and 8.3 mm working distance.

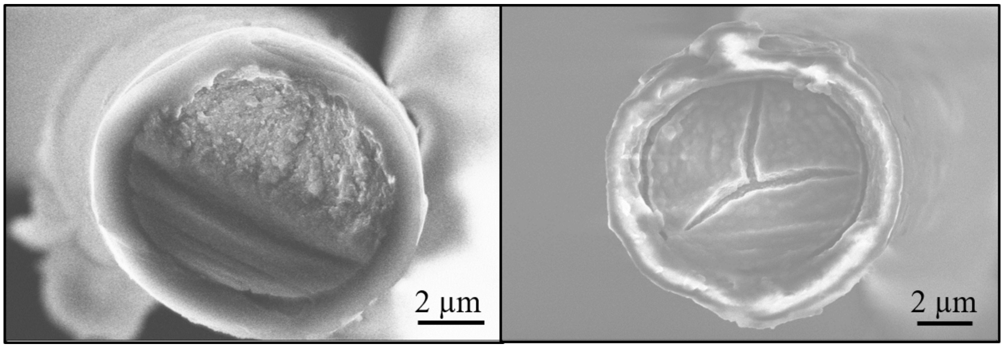

Figure 3.6: Scanning electron microscope (SEM) image of exposed cross-section of 7.2 μm carbon fiber with 1 μm parylene-c insulation layer. Left: bare cross-section without PEDOT:PSS coating imaged at 4 kV and 5.6 mm working distance. Right: PEDOT:PSS coated cross-section imaged at 3 kV and 4.7mm working distance.

repeated several times to push each successive load of hydrogel deeper into the chamber as the probe tip was too wide to be inserted millimeters into the chamber. This ensured an even, dense distribution of beads along the entire width of the chamber. The chamber was sealed using a 0.2 μm pore size aluminum oxide membrane (Sterlitech Corp., Auburn, WA, USA) and medical grade UV-curable epoxy (OG116-31, Epoxy Technology Inc., Billerica, MA, USA). A picture of a final assembled device is shown in Fig. 3.8.

For mechanical characterization, these devices were ready for testing. To prepare the assembled devices for electrical testing, the devices were epoxied and wire bonded (7440D, West-Bond, Inc., Anaheim, CA, USA) to a custom PCB breakout board to access the metal

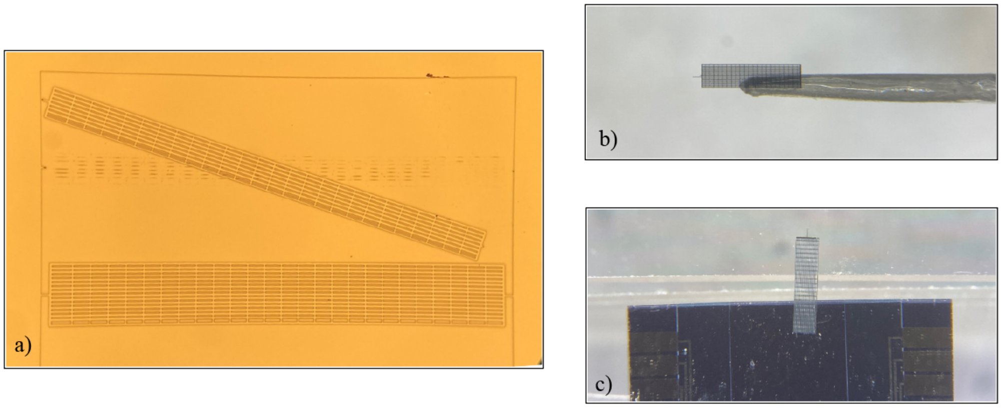

Figure 3.7: (a) Microfabricated silicon piston heads with one piston head broken off by hand. (b) Piston head mounted on silicone coated probe tip. (c) Piston head partially inserted into device chamber from back side.

electrodes patterned on the shuttle.

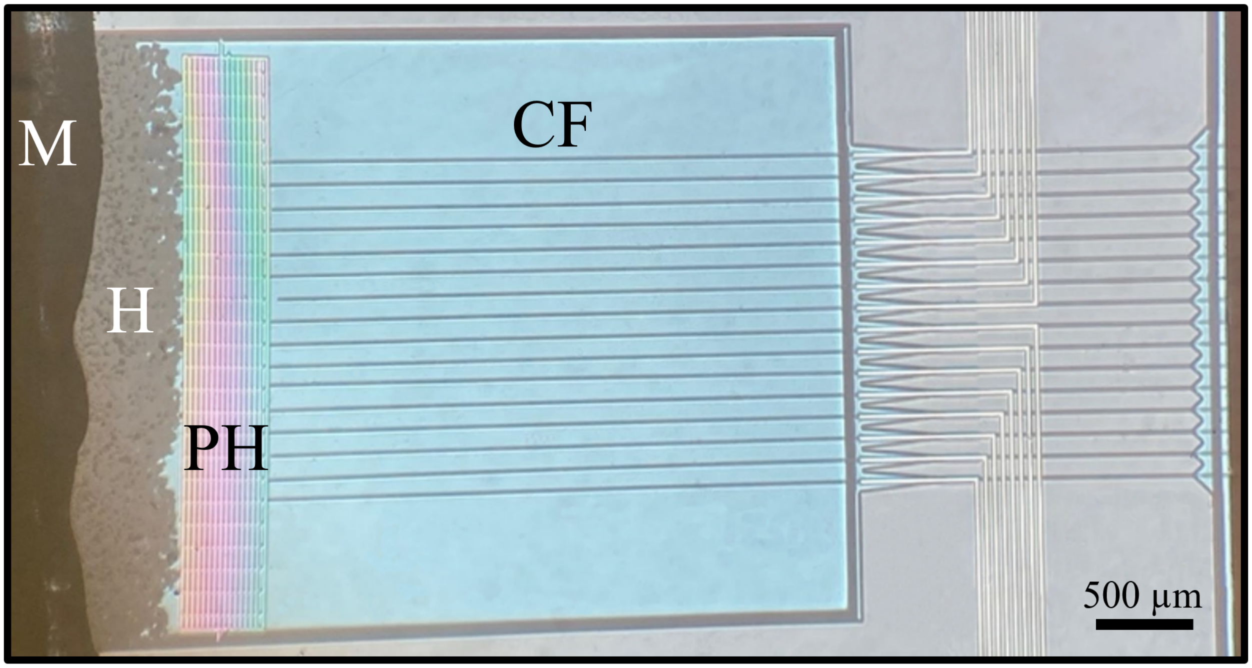

Figure 3.8: Post-fabrication assembled 16 channel device with insulated and exposed carbon fibers (CF), silicon piston head (PH), sodium polyacrylate hydrogel (H), and epoxied aluminum oxide membrane (M). Deployment direction is to the right.

Chapter 4

Exploratory Paths for Hydrogel Integration

4.1 Challenges of Hydrogel Deposition

As discussed in the last chapter, dry hydrogel particles were manually loaded into the shuttle chamber. However, significant effort was put into exploration of possible processes to deposit/integrate hydrogels using standard microfabrication process. This chapter elaborates on these investigations for loading hydrogels as well as fabricating hydrogel particles with the targeted particle size.

When depositing a layer of film for wafer-scale patterning, it should be generally compatible with standard microfabrication techniques. When it comes to hydrogel deposition, there are several challenging issues that prevent integration with existing processes like tool contamination limitations and chemical process development challenges.

The most difficult obstacle to overcome is tool cross-contamination due to high volatility of many polymers in vacuum. For example, the vapor pressure of sodium polyacrylate hydrogel is approximately 10 Torr, below which the hydrogel will vaporize and can redeposit inside the vacuum chamber. Comparing this vapor pressure to typically acceptable vapor pressures of 10^{-7} Torr for evaporators indicates that depositing a hydrogel onto a wafer will prevent it from being further processed in most high vacuum tools. Furthermore, hydrogels absorb water, making wet processing with any solutions using water as a solvent much more difficult. These limitations make a process flow extremely challenging to integrate with a hydrogel.

Regardless of contamination issues, synthesis and deposition of hydrogels themselves at wafer-scale is no trivial task. Only very specific hydrogels have a well-characterized CVD process like poly(2-hydroxyethyl methacrylate) (PHEMA) [113], [114]. Development of CVD processes for complex hydrogel polymer structures is lacking, likely due to previous mentioned limitations.

A wafer-scale deposition process using spin coated hydrated hydrogels was investigated.

Spin coating viscous fluids like photoresists or sol-gel precursors is common, but requires a uniform fluid. If a hydrogel is sufficiently hydrated and then blended until a uniform consistency, it may meet this requirement. Combined with a lift-off process (Fig. 4.1), selective deposition of hydrogels may be able to be accomplished.

4.2 Spin Coating Hydrogels

The microfabrication and spin coating process overview is as follows. A 2 µm thick photoresist was spun onto a silicon wafer, followed by a 55 µm DRIE chamber etch. The hydrated, blended hydrogel was spun onto the wafer. Afterwards, the wafer was baked at 60°C for 15 minutes to dehydrate the hydrogel, and the wafer was soaked in acetone for 10 minutes to remove the photoresist. Only the hydrogel in the chambers was left on the device.

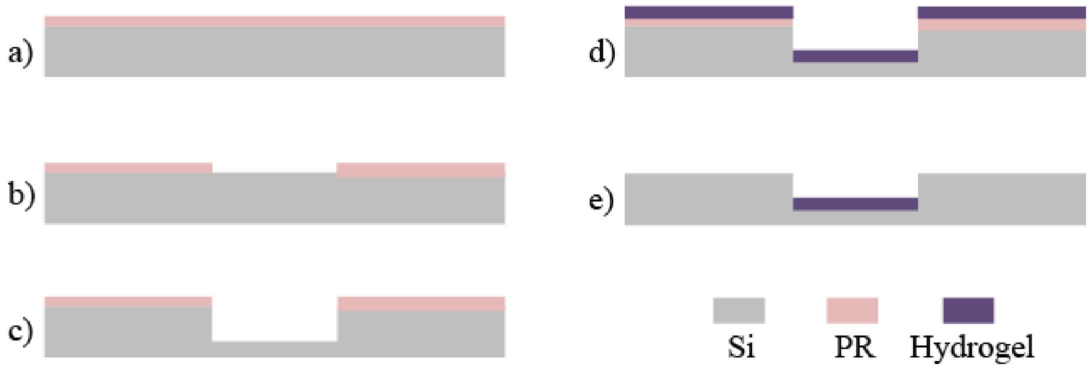

Figure 4.1: Process flow for lift-off of spin coated hydrogel. a) Spin coat photoresist (PR). b) Pattern PR. c) Deep reactive ion etch silicon substrate 55 µm. d) Spin coat hydrogel blend and bake at 60°C. e) Acetone soak to remove PR and lift-off dried hydrogel.

To fully hydrate the polyacrylate hydrogel particles, 20 g of hydrogel was thoroughly mixed into 1 L of deionized water (DI) to prevent clumping and left overnight. Afterwards, excess water was removed using a filter to strain out the saturated hydrogel particles. The particles were then blended using an immersion blender on the highest speed setting to make the final gel as uniform as possible. Even at the highest speed, it was observed that the final gel still contained small unblended particles roughly 50 µm in diameter regardless of blend time. This effectively created a hydrogel suspension, rather than a uniform colloid. If the hydrogel is not hydrated fully, the particles remain firm and cannot be blended at all.

Using an optimized spin speed and spin coating time, hydrogel volume deposited into device chambers will be maximized while avoiding sidewall coverage. The more hydrogel volume deposited, the larger the actuation distance it can provide. However, if the hydrated hydrogel overflows the chamber during spin coating, the sidewalls coverage will cause stringers and fencing of the hydrogel intended to be removed during photoresist removal. Hence, only the optimal window of spin speed and time will achieve the correct thickness of hydrogel and volume deposited into the device chambers.

Fig. 4.2 shows qualitative results of overly thick and thin coatings for a varying spin speeds of 150 rpm and 1000 rpm, respectively. Fig. 4.3 shows the results of an excessively thick coating and the resulting sidewall coverage after dehydration. Fig. 4.3 also shows an excessively thin coating which prevents full wafer uniformity. To achieve an even coating when reducing spin speed (Table 4.1), a very thick layer of hydrogel was required which makes lift-off impossible. At these low speeds, acceptably thin coatings became non-uniform when spun for longer times. Likely, slow spin speeds remove hydrogel particles at nearly the same rate as the water they were suspended in, which makes it difficult to selectively leave hydrogel on the wafer surface while removing excess water. This issue could be attributed to the inability of the blending process to produce a very uniform colloid. For higher spin speeds run at longer time lengths, no hydrogel is left on the wafer surface. When the spin time is reduced however, the separation between the excess water and hydrogel particles becomes noticeable. Water quickly spins off, but the hydrogel particles take longer to spin off wafer. Thus, spinning at higher speeds for short time was found to be best for maximize hydrogel deposition while avoiding sidewall coverage.

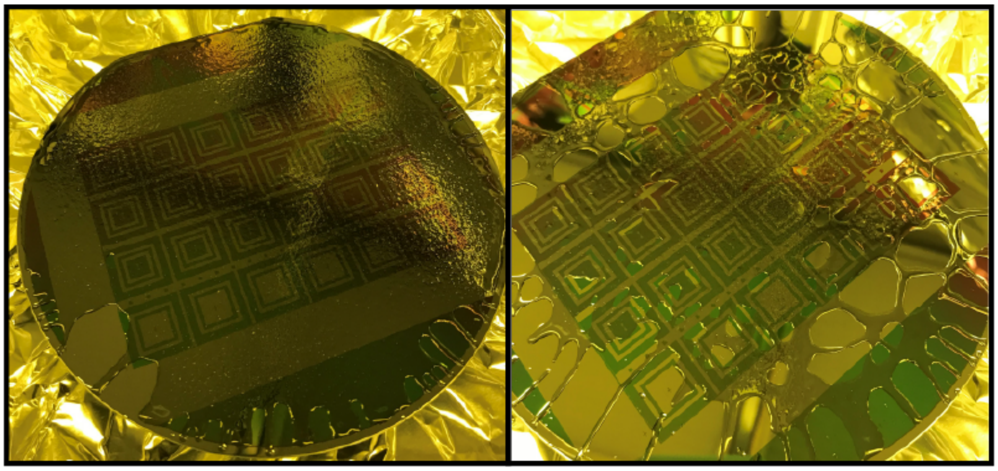

Figure 4.2: Spin coating hydrogel blend across two wafers. Left: thick coating of hydrogel blend causing eventual sidewall coverage. Right: thin coating of hydrogel blend with non-uniformity.

However, the observed final thickness of deposited hydrogel into the chamber varied wafer by wafer, and it was found that adding more hydrogel suspension onto the wafer during the second phase of the coating cycle led to more uniform and thicker layers (Fig. 4.4). There was a noticeable radial dependence of final hydrogel thickness as the center devices contained adequate dried hydrogel, but devices closer to the edge received significantly less.

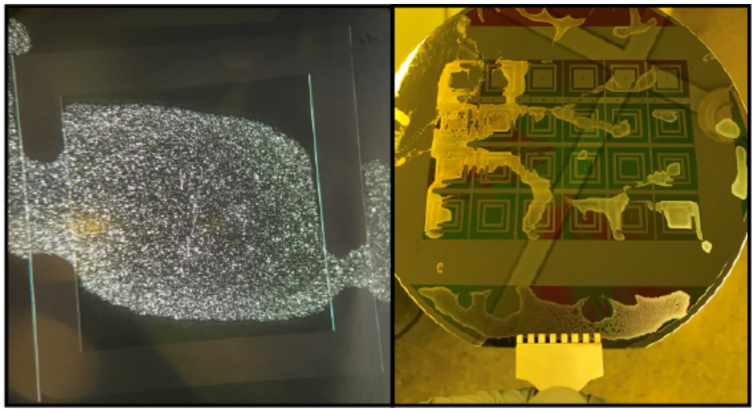

Figure 4.3: Post-dehydration bake reveals if coat is too thick or too thin. Left: thick coating with sidewall coverage and fencing. Right: thin coating showing severe non-uniformity.

This indicates that the hydrogel suspension created by blending was still too viscous and non-uniform as the spinning process only removed excess water but left a majority of the hydrogel particles at the center of the wafer.

To estimate expansion capabilities, devices with adequate dried hydrogel in the chambers were rehydrated. Fig. 4.5 shows several devices showing significant volume expansion. The

Table 4.1: Spin Coating Parameters

Even coating		**Thick coating**		**Thin coating**	
Parameter	**Value**	**Parameter**	**Value**	**Parameter**	**Value**
Ramp 1	50 rpm/s	Ramp 1	15 rpm/s	Ramp 1	100 rpm/s
Time 1	10 s	Time 1	10 s	Time 1	10 s
Speed 1	500 rpm	Speed 1	150 rpm	Speed 1	1000rpm
Ramp 2	0 rpm/s	Ramp 1	0 rpm/s	Ramp 1	0 rpm/s
Time 2	100 s	Time 1	100 s	Time 1	30 s
Speed 2	500 rpm	Speed 1	150 rpm	Speed 1	1000 rpm
Ramp 3	50 rpm/s	Ramp 1	15 rpm/s	Ramp 1	100 rpm/s
Time 3	10 s	Time 1	10 s	Time 1	10 s
Speed 3	0 rpm	Speed 1	0 rpm	Speed 1	0 rpm

Figure 4.4: Spin coating multiple coats of hydrogel blend increases volume of dried hydrogel deposited in chambers. Left: single coating of hydrogel blend after dehydration. Right: triple coating of hydrogel blend after dehydration.

qualitative results shows that while it seems it is possible to spin multiple coats of hydrogel suspension to deposit an acceptable volume of dried hydrogel into device chambers, the difficulty in creating a truly even and uniform blend prevents reasonable yield and repeatability across both a single wafer and a batch of wafers. However, these results show a possible avenue of wafer-scale deposition of hydrogels worth further investigation.

4.3 Synthesis of Hydrogel Particles

Due to the difficulty in achieving a reliable hydrogel spin coating process, several methods of synthesizing 10s of μm diameter hydrogel particles for insertion into the device chambers during assembly were investigated instead. The first step toward this goal was to identify a viable hydrogel. A viable hydrogel should have a feasible recipe, show potential for high actuation force and distance, and be synthesizable at the correct size scale. Three alginate-based recipes were investigated due to their simple chemistry and extensive documentation in the literature.

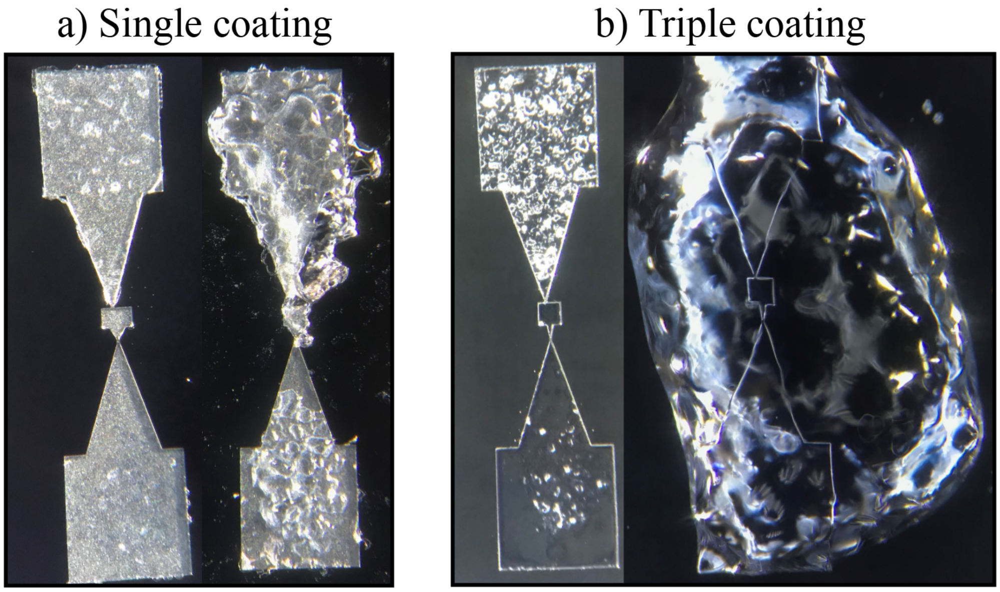

Figure 4.5: Spin coating multiple coats of hydrogel blend significantly increases rehydrated hydrogel volume. a) Single coating of hydrogel blend after rehydration. b) Triple coating of hydrogel blend after rehydration.

1. Chitosan and alginate [115]
2. $CaSO_4$ and alginate [116]
3. $CaCl_2$ and alginate [116]

To synthesize all three hydrogels, a common alginate stock solution was made by dissolving 2 g sodium alginate in 100 mL DI at room temperature. The chitosan stock solution was made by first suspending 2 g chitosan powder in DI for 30 minutes at 120°C, and then the excess water was drained and 100 mL of 0.5 M acetic acid was added. The chitosan and alginate stock solutions were mixed in a 1:1 ratio. A dicyclohexyl carbodiimide (DCC) was added to some batches of the mixed solution by melting the DCC at 40°C and dripping it into solution (Fig. 4.6). Then the hydrogel was strained and dried overnight in ambient conditions.

This recipe showed a few shortcomings, mostly do to the crosslinker. Because DCC is waxy and solid at room temperature, it must be heated to liquefy. However, trying to extrude it through a pipette or syringe causes the DCC to cool down due to the high surface area contacting the pipette/syringe walls. This re-solidifies the DCC and makes it difficult to synthesize small particles. Only large flakes can be made using this recipe. Similarly to other hydrogel polymers, grinding larger particles into smaller particles is very difficult and will be discussed later.

Figure 4.6: Chitosan and alginate crosslinked hydrogel using dicyclohexyl carbodiimide created irregularly shaped and waxy product.

The $CaSO_4$ stock solution was made by dissolving 2 g $CaSO_4$ dihydrate into 50 mL DI at room temperature. To crosslink the hydrogel, the alginate stock was dripped into the Ca solution. After 1 hour, the hydrogel particles were filtered out and dried overnight in ambient conditions. However, it was observed that after crosslinking, the particle size and shape were highly variable and generally not spherical. This was likely due to the difficulty in creating a uniformly dissolved $CaSO_4$ solution due to its naturally poor solubility in water.

The final $CaCl_2$ stock solution was made by dissolving 2 g $CaCl_2$ in 100 mL DI at room temperature. The alginate stock was dripped into the Ca solution. After 1 hour, the hydrogel particles were filtered out and dried overnight in ambient conditions (Fig. 4.7). The $CaCl_2$ and alginate hydrogel particles were highly spherical and showed large volume changes when rehydrated (2.9× increase in radius and 24.4× increase in volume). It is notable that these hydrogel do not rehydrate in isopropyl alcohol (IPA) or DI, but they rehydrate in ionic solutions like NaCl, KCl, $MgCl_2$, etc. The higher the ionic concentration, the faster the rehydration.

Once initially synthesized, then dehydrated and rehydrated, it was observed that the rehydrated hydrogel particles showed slightly reduced radius and mass (Table 4.2). The particles were dehydrated at 70°C for 35 minutes and rehydrated with 0.9% saline for 20 minutes. The average hydrated radius was approximately 3 mm, the average dehydrated

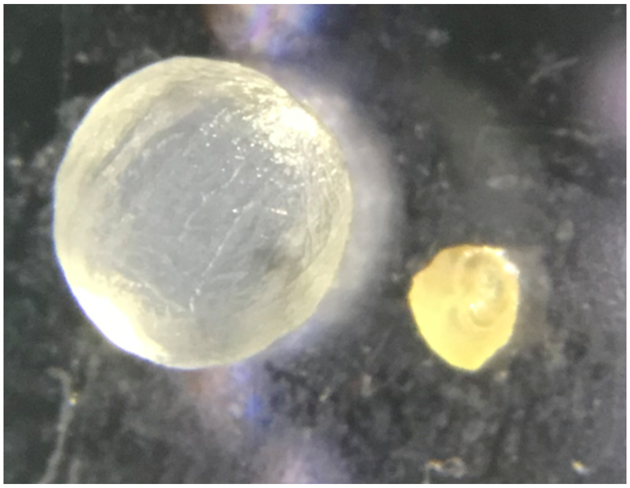

Figure 4.7: $CaCl_2$ and alginate crosslinked hydrogel creates a spherical product. After dehydration, radius decreases by 2.9× and volume by 24.4×. Left: Hydrated particle. Right: Dehydrated particle.

radius was approximately 1 mm, and the average rehydrated radius was between 2-2.5 mm. The dehydrated particles were stored in IPA overnight, and rehydration was not affected by whether the hydrogel had been soaked in IPA. Final rehydration mass was on average within 90% of the initial synthesis mass.

Because the $CaCl_2$ particles showed rehydration capabilities, scaling the size of the particles was then investigated. Three methods to extrude the alginate solution into the $CaCl_2$ solution to synthesize micron-scale particle sizes were explored:

1. Capillary pulling
2. Humidifier
3. Atomizing nozzle

Using a micropipette puller (P-30, Sutter Instruments, Novato, CA, USA), glass capillaries (1B100-3, World Precision Instruments, Sarasota, FL, USA) were pulled into thin micropipettes by applying heat and an axial force. The glass softens and when pulled, narrows into a nanometer-scale wide tip. The tip size, taper length, and taper angle are controlled by the temperature and force applied to the capillary (Fig. 4.11a). A micropipette grinder (MicroGrinder EG-401, Narishige International USA, Inc., Amityville, NY, USA) was used to remove the tip of the pulled capillary to open a 10-20 μm hole to extrude solutions (Fig. 4.11bc). However, when the calcium solution was extruded from the capillary tip (Fig. 4.11d), the pressure would build up rather than steadily dispensing solution. This led to uneven hydrogel particle size and string formation (Fig. 4.11e).

A commercial humidifier was used initially to generate a fine aerosol from the $CaCl_2$ solution into the alginate solution. However, the less dense $CaCl_2$ would float at the top of the alginate solution, and the speed of crosslinking occurred at a slower rate than subsequent layers of $CaCl_2$ depositing on previous layers. This caused a skin to form rather than individual particles (Fig. 4.8). Reversing the two solutions (alginate aerosols into $CaCl_2$ solution), caused sputtering of the humidifier due to the higher viscosity of the alginate solution. This reduced the rate of particle generation significantly and increased particle diameter to over 100 µm.

Finally, a pressurized atomizing nozzle (1/4-J-SS, Spraying Systems Co., Glendale Heights, IL, USA) was used to aerosolize the alginate solution into the $CaCl_2$ solution (Fig. 4.9). The nozzle produced aerosols with an average diameter of 8.2 µm with 90% of particles having diameters less than 15 µm. When run with <60 psi, the nozzle produced hydrogel sheets/tendrils in the $CaCl_2$ solution. To produce individual particles, the nozzle needed to be run with 60 psi. However, this would also cause the particles to adhere to each other so the nozzle was duty cycled (5 seconds on, 15 seconds off) to allow the initial layer of particles to crosslink and sink to the bottom of the $CaCl_2$ solution. This produced particles with diameters <100 µm with spherical shapes (Fig. 4.10).

To isolate and dry the hydrogel particles, the suspended hydrogel was transferred to a centrifugal filter tube (Pierce Protein Concentrator PES, 30K MWCO, 5-20 mL, Thermo Fisher Scientific, Waltham, MA, USA) and spun at 3300 rpm for 10 minutes. The particles were dried overnight in ambient conditions, and then suspended in IPA. The particle suspension was then loaded into the pulled micropipettes via syringe. Similar to previous micropipette extrusion issues, the suspension was unable to be dispensed. In addition, the

Table 4.2: Dehydration, IPA Suspension, and Rehydration of Hydrogel

Batch 1	**Particles**	**Total Mass (g)**	**Mean Mass (g)**	**% Mass Increase**
Prehydration	100	0.9581	9.581×10^{-3}	100%
Dehydration	100	0.03	3×10^{-4}	3.1%
Rehydration	97	0.849	8.757×10^{-3}	91.4%
Post-IPA Rehydration	96	0.8526	8.881×10^{-3}	92.70%

Batch 2	**Particles**	**Total Mass (g)**	**Mean Mass (g)**	**% Mass Increase**
Prehydration	49	0.5018	1.024×10^{-2}	100%
Dehydration	49	0.0069	1.408×10^{-4}	1.4%
Rehydration	42	0.4534	1.080×10^{-2}	105.4%
Post-IPA Rehydration	23	0.227	0.986×10^{-2}	96.3%

Figure 4.8: Hydrogel "skin" formed on surface of alginate stock when using humidifier to aerosolize $CaCl_2$ solution into alginate. Necessary to aerosolize alginate solution into $CaCl_2$ stock due to density difference allowing alginate particles to sink.

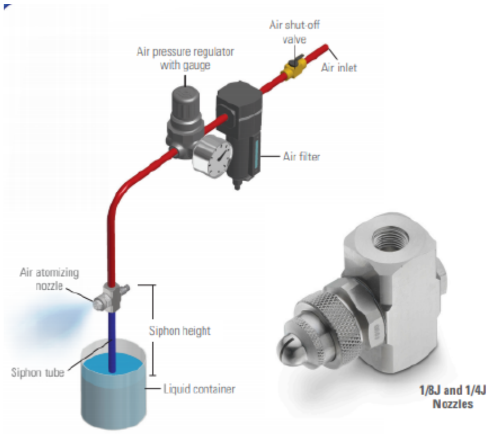

Figure 4.9: Pressurized nozzle used to aerosolize alginate solution into $CaCl_2$ solution and setup. *Adapted from [117]*

micropipettes were subject to frequent clogs from larger dust particles or even clumps of hydrogel particles. These difficulties, combined with the low yield of adequately sized particles and complex processing steps, made scaling the hydrogel particle synthesis impractical.

4.4 Toward Scalable Hydrogel Integration

Though this body of work moved away from deposition of hydrogels via spin coating or particle dispensing, it provides possible paths for investigation to enable scalable wafer-level integration of hydrogels. With a refined blending process, a highly uniform hydrogel colloid

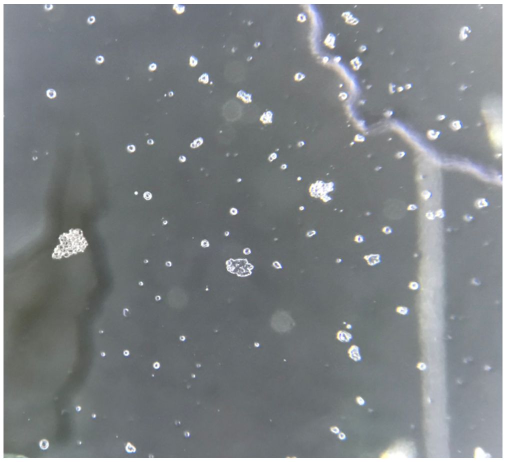

Figure 4.10: Alginate/$CaCl_2$ hydrogel particles <100 μm in diameter produced by pressurize nozzle

can be spin coated over an entire wafer and lifted off to deposit dry hydrogel. A microdispenser with a pump and properly fitted nozzles may be able to load the hydrogel/IPA suspension simultaneously into many devices at once after microfabrication and dicing. As will be discussed in later chapters, these wafer-scale routes could possibly have an advantage over manually loading hydrogel particles when it comes to overall scalability in next-generation hydrogel actuated designs.

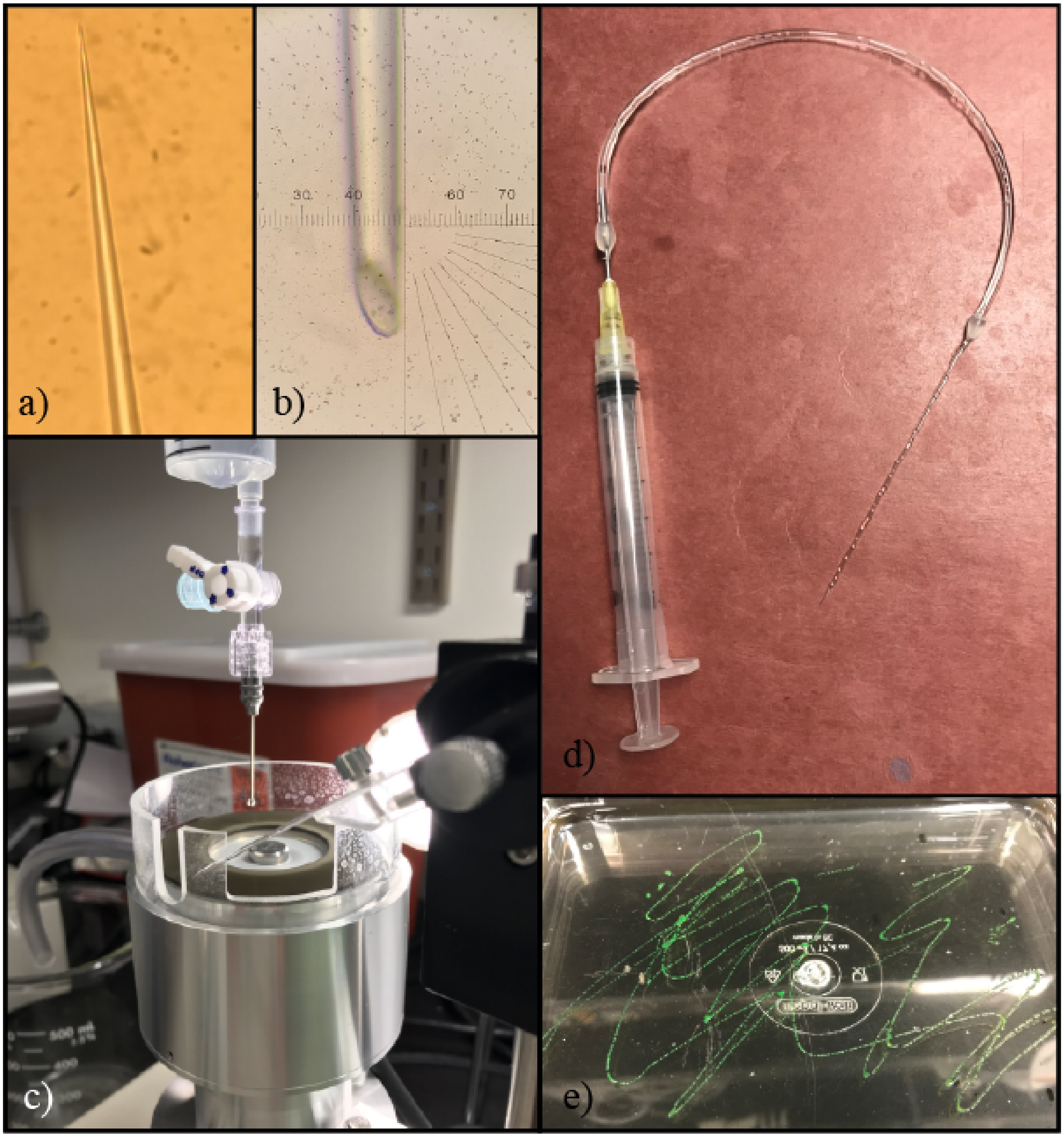

Figure 4.11: Development of micropipette syringe extrusion of hydrogel. a) Glass capillary formed into micropipette with nm-scale tip size using pipette puller. b) Microscope image of pipette opening roughly 17 μm inner diameter. c) Micropipette grinder used to open micropipette. d) Micropipette, plastic tubing, and syringe epoxied together to form extrusion device. e) Fluorescent dye mixed with hydrogel precursors extruded from micropipette. High pressure forms strings of gel rather than particles.

Chapter 5

Electrical and Mechanical Modeling Methods

5.1 Impedance Requirements for Recording

The importance of minimizing the signal path impedance is apparent in a generic equivalent circuit model of the recording environment (Fig. 5.1). Because neural signals have exceedingly low amplitudes, the signals must be amplified for further processing. Ideal amplifiers have infinite input impedance, meaning that as long as the impedance of the circuit leading up to the input of the amplifier is finite, the entire signal voltage is dropped across the amplifier input. However, if the input impedance of the amplifier is not significantly higher than the input circuit impedance, only a fraction of the signal voltage will be dropped across the amplifier input. This leads to an attenuated final amplified signal which is highly undesirable. Modern amplifiers for neural recordings can have input impedances of 100s of MΩ to GΩs [118], [119]. Generally, the amplifier input impedance should be designed to be an order of magnitude larger than the impedance of the rest of the circuit to mitigate this loading effect.

Though series impedances are important to consider, shunt impedances are possibly even more essential to design for. Shunt impedances occur in parallel to the amplifier input, and if they are relatively low, they reduce the overall input impedance of the amplifier circuit [120]. These shunt impedances can be current leaks along long wires, parasitic capacitances through the substrate/adjacent conductors, or other difficult to estimate paths. In order to keep the input impedance of the amplifier high, these shunt impedances should be as large as possible. A reasonable ballpark to aim for is a shunt impedance of 10× the total series input impedance seen by the signal source.

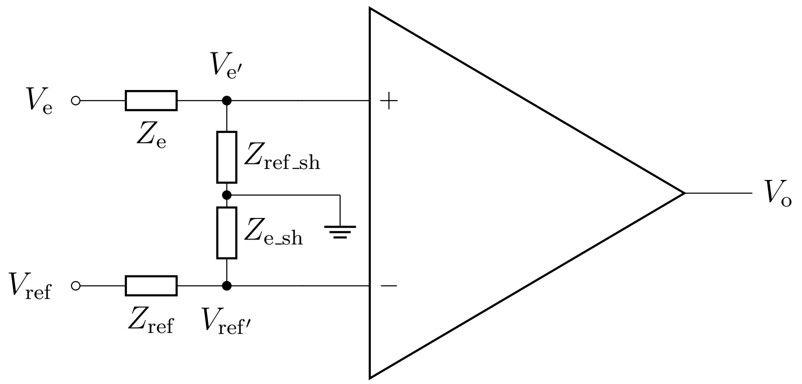

Figure 5.1: Simplified circuit diagram for visualizing voltage drops and current leakage paths. V_{ref} and V_{e} are the input potentials, Z_{ref} and Z_{e} are the effective electrode impedances for the input potentials, $Z_{\mathrm{ref\_sh}}$ and $Z_{\mathrm{e\_sh}}$ are the effective amplifier input impedances, and $V_{\mathrm{ref}'}$ and $V_{\mathrm{e}'}$ are the voltages measured by the amplifier. Note that the shunt impedances simultaneously increase current through the input circuit and reduce the amplitude of the measured signal due to the voltage divider effect and can have an impact on the frequency spectrum of the output if the reactances are non-negligible.

5.2 Intrachannel and Interchannel Impedance

To show acceptable recording capability, a neural probe should have low impedance of a single channel to maximize output signal amplitude while also having high impedance between channels to minimize multichannel crosstalk. For this CFMEA in particular, this can be verified through low "intrachannel" impedance from the tissue-facing tip of each fiber to its corresponding metal electrode in its channel and high "interchannel" impedance between adjacent metal electrodes between neighboring channels.

The electrical signal path of a single channel consists of a parylene-coated insulated carbon fiber, a metal electrode, and aCSF electrolyte bridge between them to couple the signal. After actuation is completed, an electrical signal is detected by the exposed tissue-facing tip of the fiber, travels along fiber to the exposed distal end, coupled through a thin layer of aCSF between the fiber and metal electrode, and finally reaches the metal electrode inside the shuttle (Fig. 2.3). aCSF enters the channel that the fiber resides in due to capillary force and bridges the exposed segment of the distal end of the fiber to the metal electrode patterned onto the shuttle substrate. The total impedance of this architecture should be minimized to improve the overall signal amplitude and signal-to-noise ratio (SNR).

To minimize intrachannel impedance and maximize interchannel impedance in this device, a specific funnel geometry was implemented at the end of each channel inside the shuttle between the chamber and channels (see Fig. 5.2). When these funnels are filled completely with electrolyte, the electrolyte reaches laterally from one channel funnel to adjacent funnels which couples all channel together and leads to high crosstalk. If the funnels are dry without any electrolyte, there is no electrolyte connecting each adjacent channel. The tapered angle of the funnels was to increase the width of the channels to reduce the capillary force in the funnels and observe the air-aCSF meniscus behavior during testing.

After immersion in electrolyte solution, the device undergoes two transitions from the "dry" state to the "flooded" state to the "expansion" state which can be observed in the channels' funnel structures (Fig. 5.2). Effective electrical recording can only occur during the expansion state. Before immersion into aCSF, the device is in the dry state with high intrachannel and interchannel impedance while there is no electrolyte bridge in the channels. Immediately after immersion, the device transitions to the flooded state with low intrachannel and interchannel impedance as the electrolyte fills all channels and their funnel structures to couple all channels together. It is critical to note that at this time, an air pocket is trapped inside the chamber as both the hydrogel at the back side and channels at the front side of the device are filled with aCSF. As the hydrogel absorbs aCSF and expands, its increased volume displaces a small fraction of this trapped air and forces it out through the open ends of the channels of the device. The device enters the expansion state once the fiber is actuated to the point that the exposed distal section of the fibers line up with the metal electrodes. At this point, the device presents low intrachannel as the electrolyte between each fiber and its corresponding electrode is maintained due to the capillary effect as aCSF still lines the length of the channels due to the hydrophilicity of the channel walls. Simultaneously, the device presents high interchannel impedance as the aCSF bridge between the funnel structures at the end of the channels is replaced by the air bubble due to the hydrogel expansion. With this architecture, low intrachannel impedance can be maintained while maximizing interchannel impedance.

5.3 Electrode-Electrolyte Interface Impedance

In order to properly analyze the electrical circuit equivalent of the intrachannel impedance, it is important to note that the impedance of a conductor immersed in is not simply a resistor. Rather, the impedance at the electrode-electrolyte interface (EEI) is dominated by the ion behavior. Conceptually, if there exists a potential difference between the metal surface and the surrounding electrolyte solution due to a neural firing or an applied current/voltage during stimulation, the ions within the solution are drawn closer to the conductor due to electrostatic forces. Depending on the magnitude of charge injected or voltage applied, these ions either line up along the electrode surface forming a structure resembling a capacitor or combine with the electrode material causing chemical reactions at the electrode surface. These phenomenon are know as non-Faradaic and Faradaic processes, respectively.

In typical electrodes used for recording and stimulation, the electrodes experience high current densities and cause Faradaic processes driven by reduction-oxidation reactions. In that situation, EEI impedances can be modelled using a simplified Randle's cell model (Fig. 5.3) usually involving a charge transfer resistance, R_{ct} in series with a Warburg impedance,

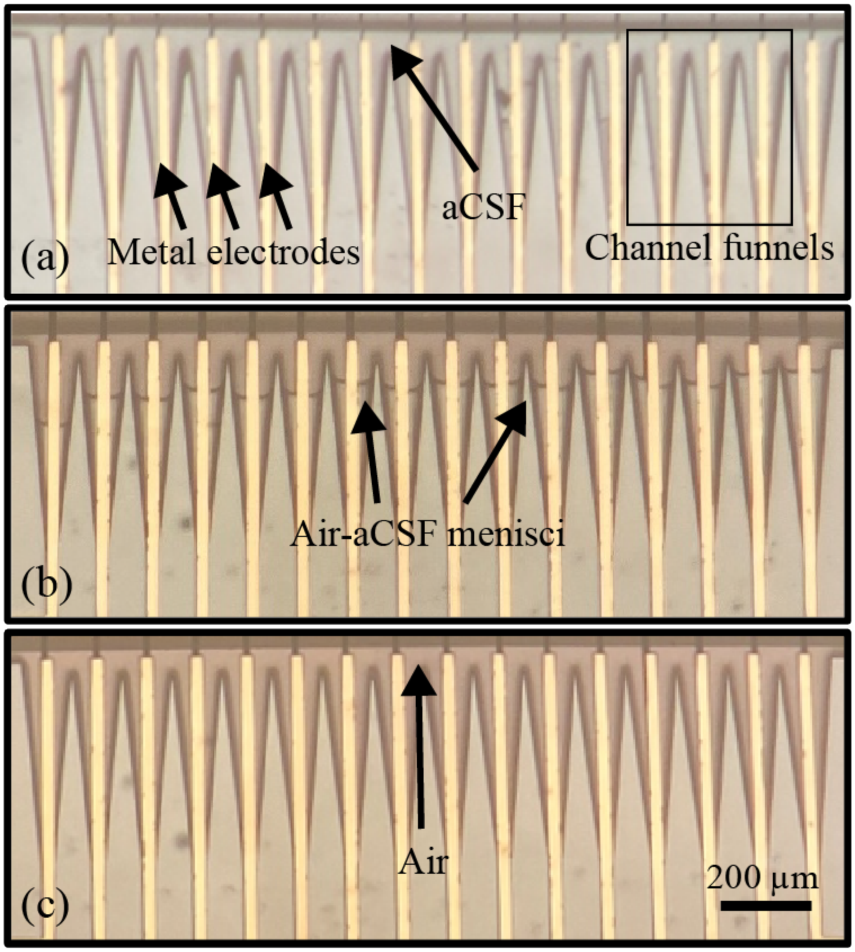

Figure 5.2: Electrolyte states in channel funnels during hydrogel expansion. Chamber is north of channel funnels. (a) Initial flooded state during which all channels are coupled together. (b) Intermediate moment before the expansion state during which receding air-aCSF meniscus in each funnel structure is visible and adjacent channels are not coupled together. (c) Final expansion state during which expansion is complete, air has displaced aCSF in the funnel structures, intrachannel impedance is low, interchannel impedance is high, and crosstalk is low.

Z_W, all in parallel with a double layer capacitance, C_{dl} [121]. The charge transfer resistance models the transfer of electrons between the metal and electrolyte, and thus charge is being transferred. The speed of these reactions is dependent on the temperature, concentration of reaction products, and applied voltage, and if operated in this regime for long periods of time, the electrode material itself can corrode. The Warburg impedance models the effects of reactants diffusing into the bulk electrolyte. This impedance has a frequency

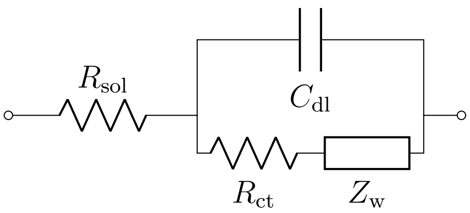

Figure 5.3: Randle's cell equivalent circuit to model the electrode-electrolyte interface impedance for Faradaic processes where R_{sol} is the solution resistance, C_{dl} is double layer capacitor, R_{ct} is charge transfer resistance, and Z_{w} is the Warburg impedance.

dependence due to the finite time constant for the diffusion rate. At high frequencies, this diffusion process is supressed, and the Warburg impedance is small. At low frequencies, the reactants have more time to diffuse, and the opposite is true. However, because this device is used for recording, the electrochemical processes at the EEI are non-Faradaic due to a very low driving voltage of actuation neurons (∼1mV). This implies that no charge crosses the interfaces and the behavior is analogous to charging and discharging a capacitor. It is worth noting that in practical electrochemical impedance spectroscopy, this double layer capacitor does not behave like an ideal capacitor, but rather as a constant phase element which will be discussed later.

When used only for recording and not stimulation, the charge transfer resistance and Warburg impedance within the Randle's cell model can be ignored. This can be shown trivially:

$$R_{ct} = \frac{RT}{nFi_0} \tag{5.1}$$

where R is the gas constant, T is the temperature, F is the Faraday constant, n is the number of electrons transferred, and i_0 is the exchange current density. Here both n and i_0 are negligible in non-Faradaic processes and drive $R_{ct} \to \infty$.

$$Z_W = \sigma\omega^{-1/2} - j\sigma\omega^{-1/2} \tag{5.2}$$

where ω is the frequency and σ is the Warburg coefficient which is defined as

$$\sigma = \frac{RT}{n^2F^2A\sqrt{2}}\left(\frac{1}{\sqrt{D_O}c_O^\infty} + \frac{1}{\sqrt{D_R}c_R^\infty}\right) \tag{5.3}$$

where A is the electrode area, D_O and D_R are the diffusion coefficients and c_O^∞ and c_R^∞ are the bulk concentrations for the species O and R respectively in any reversible electrochemical redox reaction $O + ne^- \rightleftharpoons R$. Due to negligible non-Faradaic processes at the EEI, c_O^∞ and $c_R^\infty \to 0$ and therefore σ and $\mathrm{Z}_W \to \infty$. Due to the lack of redox reactions at the EEI, we ignore the charge transfer resistance and Warburg impedance [122].

Consequently, at the EEI, we model the impedance using a double layer capacitance only. This double layer capacitance is a result of adsorbed ions on the surface of the electrode which repels charges of the same polarity. Because there is a space between these two charged layers, it effectively acts as a capacitor. There are many circuit models of this double layer capacitance in the literature, and we will be using the Guoy-Chapman-Stern model [122], [123], [124], [125]. The double layer capacitance can be expressed as a series of capacitors, the Helmholz capacitance and the diffuse capacitance:

$$\frac{1}{C_{\mathrm{dl}}} = \frac{1}{C_{\mathrm{H}}} + \frac{1}{C_{\mathrm{diff}}} \tag{5.4}$$

C_H and C_{diff} are given as:

$$C_H = A\frac{\epsilon_0\epsilon_r}{d} \tag{5.5}$$

$$C_{\mathrm{diff}} = A\sqrt{\frac{2n_o\epsilon_0\epsilon_r z^2 e^2}{kT}}\cosh\left(\frac{zeV}{2kT}\right) \tag{5.6}$$

where A is the effective surface area of the electrode, d is the thickness of the Helmholtz layer, n_o is the bulk concentration of ions, V is the potential drop between the electrode and bulk electrolyte, z is the valency of the ion, e is the elementary charge, k is the Boltzmann constant, T is the temperature, and ϵ_0 and ϵ_r are the permittivity of free space and the relative permittivity of body saline.

The thickness of the Helmholtz layer can be estimated with the Debye length, the measure of a charge carrier's net electrostatic effect in the solution:

$$d = \sqrt{\frac{\epsilon_0\epsilon_r kT}{2Nn_0 z^2 e^2}} \tag{5.7}$$

where N is the Avogadro constant.

The final EEI impedance of a recording electrode used in this device can be approximated as a double layer capacitor and numerically estimated using the Guoy-Chapman-Stern model.

5.4 Signal Path Intrachannel Impedance

Given that an approximate model has been established for an EEI impedance, the intrachannel impedance of the signal pathway composed of a carbon fiber microelectrode, an aCSF electrolyte bridge, and a metal electrode can be established. The signal pathway is composed of three EEI impedances, the solution impedance of the aCSF electrolyte bridge, the fiber impedance, and the parasitic leakage impedance of the surrounding aCSF along the channel. The three EEIs are at the surfaces of the metal electrode, distal end of the fiber, and cross-section of the fiber tip. The cross-section of a single channel with all impedances is shown in Fig. 5.4. Order of magnitude estimations for each impedance can inform which impedances can be ignored and which are relevant to the final intrachannel impedance model.

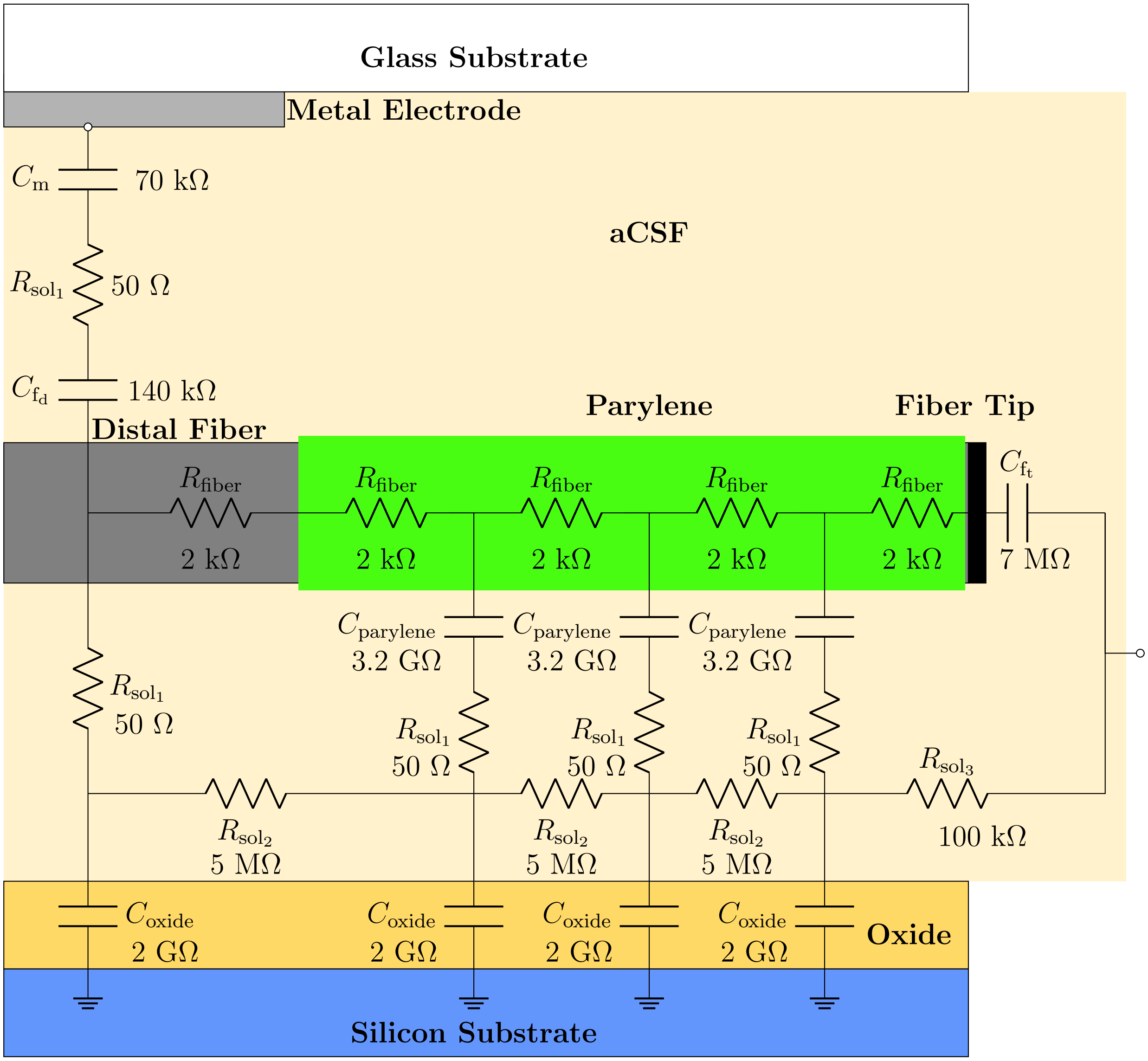

Figure 5.4: Diagram of full equivalent circuit for electrical recording in a single channel.

The fibers themselves typically have a measured characteristic impedance of 2 kΩ/mm. The line capacitance of the fiber to the electrolyte can be estimated using the parallel plate capacitance model:

$$C_{\text{parylene}} = \epsilon_{\text{parylene}}\epsilon_o \frac{w}{t_{\text{parylene}}} \tag{5.8}$$

where $\epsilon_{\text{parylene}}$ is the relative permittivity of parylene-C, w is the effective width of the capacitor given here as half of $2\pi r_{\text{fiber}}$.

This yields a line capacitance of roughly 32 nF/mm. At 1 kHz, this corresponds to an impedance of 3.2 GΩ for 1 mm of fiber. Similarly, the impedance of the capacitance coupling the electrolyte in the channel to the wafer substrate is approximately 2 GΩ. For electrolyte solution with concentration near physiological saline, the impedance of aCSF is purely resistive. The resistance of the aCSF solution can be expressed as:

$$R = \rho \frac{l}{A} \tag{5.9}$$

where ρ_{aCSF} is the resistivity of aCSF at body temperature (1 Ω/m), l is the length of the segment of aCSF being considered, and A is the cross-section area of the segment. For the aCSF between the substrate and parylene insulated fiber separated by about 0.5 μm, this corresponds to a total resistance of about 50 Ω. For the lengthwise aCSF segments along the fiber, this corresponds to a total resistance of about 200 MΩ.

At 1 kHz, the impedance of the double capacitance of the metal electrode is approximately 70 kΩ and the exposed distal end of the fiber is approximately 140 kΩ. The capacitive impedance of the exposed fiber tip is approximately 5 MΩ.

Lumping together the line capacitances in parallel and series aCSF resistances (along the direction of the fiber), these components can be grouped as a single parasitic parallel resistor and shunt capacitor. This yields an equivalent circuit model shown in Fig. 5.5.

At the center frequency of single unit neural activity of 1 kHz, the R_{p} and C_{p} impedances are much larger (10s MΩ and >1 GΩ, respectively) than those of the EEI double layer capacitances (100s kΩ) due to the small difference between the fiber and channel diameters and low surface area of the fiber contributing to the capacitance, respectively. R_{sol} is small (100s Ω) due to micron-scale distance between the fiber and metal electrode. Note that if C_{p} and R_{p} are ignored, the remaining series capacitances should be dominated by the smallest capacitor, C_{f_t}, due to its smaller EEI surface area compared to those of C_{f_d} and C_{m}. To minimize the total signal path impedance of this configuration, the most critical impedance to reduce is thus C_{f_t} by electroplating the tissue-facing fiber ends with PEDOT:PSS. To avoid multichannel crosstalk or reduced signal amplitude recorded by the metal electrode, the parasitic impedances should be as large as possible by reducing A_{ch} and increasing the parylene insulation thickness.

5.5 Hydrogel Expansion Force Variation

The force exerted by the hydrogel was non-linear in both time and distance due to the thermodynamics of its network swelling. Dry hydrogel is considered to be in its unsolvated glassy phase and transitions to a rubbery phase as water penetrates the polymer network due to its high water affinity and permeability [126]. This enthalpic process can be related the free energy of mixing, ΔG_{mix}, from the polymer and solvent interaction. However, as more water penetrates the network, the entropic elastic retractive force increases as the polymer network is being stretched. This process is described by the elastic free energy, ΔG_{elas}. The hydrogel/water system can be described as follows using the Flory-Rehner Theory [127]:

$$\Delta G_{\text{sys}} = \Delta G_{\text{mix}} + \Delta G_{\text{elas}} \tag{5.10}$$

At first, $\Delta G_{\text{mix}} << 0$ and $\Delta G_{\text{elas}} > 0$ as water absorption is heavily favored. As the swelling continues, ΔG_{mix} begins increasing, and ΔG_{elas} decreases. Eventually, the process reaches a point at which $|\Delta G_{\text{mix}}| = |\Delta G_{\text{elas}}|$ and $\Delta G_{\text{sys}} = 0$. This is the equilibrium point at which swelling stops.

This indicates that for a single hydrogel particle, the maximum force should occur at the very beginning of the expansion process as this is where the free energy of the system is at its maximum absolute magnitude. As the hydrogel continues to swell, it gradually decreases its force output until it reaches equilibrium. For a differential volume of hydrogel, $\mathrm{d}V = tl\,\mathrm{d}w$, where t is the thickness, l is the length, and $\mathrm{d}w$ is the differential width, the force exerted in the direction parallel to the width decreases with time. Simply integrating over the width shows that this relationship is also true for any volume of hydrogel.

The exact force vs. distance and force vs. time curves were not explored in this work, but should be investigated moving forward as this could inform the maximum penetration depth of the fibers as the shear force of tissue penetration increases with depth as the actuation force decreases.

5.6 Lower Bound Hydrogel Actuation Force Estimate

Accurate measurements of sub-mN forces is non-trivial and generally require a dedicated MEMS device to properly characterize. For example, non-point source forces can be measured using flexing diaphragms where the displacement of the diaphragm is measured optically or capacitively [128], [129]. Point source forces can be measured using silicon spring devices [130], [131]. Though these measurement methods can be quite accurate, they require designing and fabricating separate device.

The device design of this CFMEA lends itself to support a simple method for assessing the lower bound estimate for hydrogel actuation force. This method centers around the critical buckling load, also known as Euler's critical load (Fig. 5.6). This value is the compressive load at which a long column will be unable to tolerate the total force and buckle.

This load is given as:

$$P = K\pi^2 \frac{EI}{l^2} \tag{5.11}$$

where P is the critical buckling load, K is the column effective length factor, E is the Young's modulus, $I = \frac{\pi}{4}r^4$ is the area moment of inertia, and l is the unsupported length of the fiber. As P increases, the column can be colloquially considered "stronger" or able to support more weight without bending. Once the column bends, it is unable to bear any reasonable load without further deformation. For columns made from stiff materials with a large Young's modulus, they can bear larger loads than columns of the same dimensions with a smaller modulus. Similarly, all things equal, a shorter or wider (larger cross-sectional area) column will also support a larger load before buckling. The K constant describes the boundary conditions at the ends of the column. Depending on how the ends of the column are supported, this affects the maximum load as well. For instance, one boundary condition is "fixed" where the end of the column cannot move nor be tilted. Another boundary condition is "pinned" where the end of the column cannot move, but it can be tilted. There are other types of conditions as well, and they also will affect K (Fig. 5.7).

A carbon fiber can be considered a column, given its large length to cross-sectional area ratio. This means that if a force is applied axially to a fiber, the force can be approximated if the fiber buckles and the dimensions of the fiber are known. However, it is important to note that the critical buckling force calculated is not the exact force, but rather the minimum value of the force. If the force applied to the fiber is much larger than the critical buckling load, it will still buckle the fiber. To successively approximate this force, shorter and shorter fibers can be used to increase the minimum force estimation.

To set up this situation, a fiber was inserted into an assemble device and then fixed to the substrate with an epoxy that flowed up the channel similar to the aCSF. Once cured, the length of the fiber in the channel was fixed, but the length of the fiber in the chamber was still free. This free fiber length can be considered the column. As the hydrogel expanded after exposure to aCSF, eventually made contact with the distal tip of the fiber and buckled it. With the known fiber dimensions, the critical buckling load and minimum force applied by the hydrogel can be calculated.

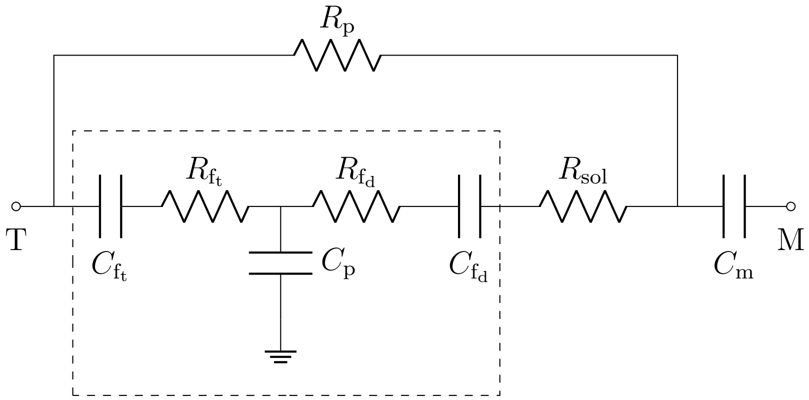

Figure 5.5: Equivalent circuit diagram for signal path from tissue (T) to metal electrode (M). $C_{\mathrm{f_t}}$: double layer capacitor at exposed tissue-facing end of the fiber, $R_{\mathrm{f_t}}$: resistance of the tissue-facing half of the fiber, C_{p}: parasitic shunt capacitance from the fiber to ground, $R_{\mathrm{f_d}}$: resistance of the distal half of the fiber, $C_{\mathrm{f_d}}$: double layer capacitor at the exposed distal end of the fiber, R_{sol}: thin aCSF bridge between the distal end of the fiber and the metal electrode, C_{m}: double layer capacitor at the metal electrode, and R_{p}: parasitic shunt resistance of the aCSF in the channel. The boxed section of the diagram contains all impedances associated with the fiber itself.

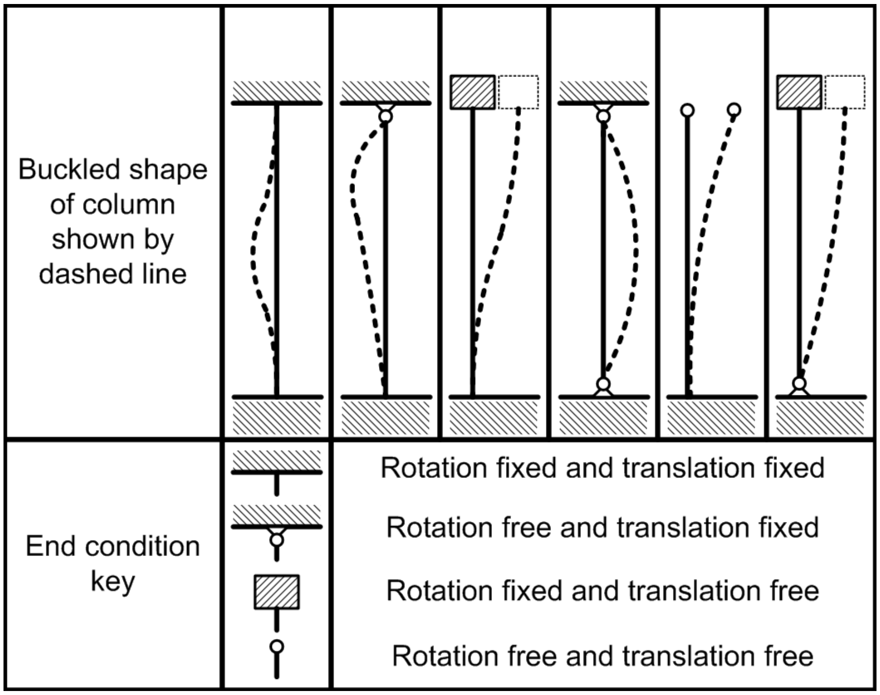

Figure 5.6: Critical buckling load modes dependent on end boundary conditions. *Adapted from Wikimedia Commons*

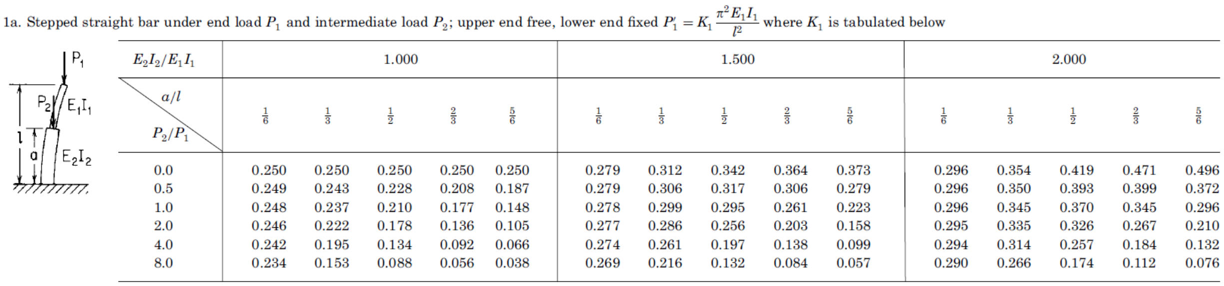

1a. Stepped straight bar under end load P_1 and intermediate load P_2; upper end free, lower end fixed $P_1' = K_1 \frac{\pi^2 E_1 I_1}{l^2}$ where K_1 is tabulated below

E_2I_2/E_1I_1	1.000					1.500					2.000				
a/l \ P_2/P_1	$\frac{1}{6}$	$\frac{1}{3}$	$\frac{1}{2}$	$\frac{2}{3}$	$\frac{5}{6}$	$\frac{1}{6}$	$\frac{1}{3}$	$\frac{1}{2}$	$\frac{2}{3}$	$\frac{5}{6}$	$\frac{1}{6}$	$\frac{1}{3}$	$\frac{1}{2}$	$\frac{2}{3}$	$\frac{5}{6}$
0.0	0.250	0.250	0.250	0.250	0.250	0.279	0.312	0.342	0.364	0.373	0.296	0.354	0.419	0.471	0.496
0.5	0.249	0.243	0.228	0.208	0.187	0.279	0.306	0.317	0.306	0.279	0.296	0.350	0.393	0.399	0.372
1.0	0.248	0.237	0.210	0.177	0.148	0.278	0.299	0.295	0.261	0.223	0.296	0.345	0.370	0.345	0.296
2.0	0.246	0.222	0.178	0.136	0.105	0.277	0.286	0.256	0.203	0.158	0.295	0.335	0.326	0.267	0.210
4.0	0.242	0.195	0.134	0.092	0.066	0.274	0.261	0.197	0.138	0.099	0.294	0.314	0.257	0.184	0.132
8.0	0.234	0.153	0.088	0.056	0.038	0.269	0.216	0.132	0.084	0.057	0.290	0.266	0.174	0.112	0.076

Figure 5.7: Straight column under axial load with K values listed for various conditions. *Figure reproduced from [132] with permission*

Chapter 6

Electrical and Mechanical Characterization

6.1 Impedance Characterization Setup

Intrachannel and interchannel impedance measurements were made before and after hydrogel expansion as the fibers were actuated (Fig. 5.2). Intrachannel impedance was measured twice. First, the intrachannel impedance of just the fiber-aCSF-metal electrode portion of the signal path was characterized by shorting the tissue-facing end of the fiber to an external wire. This ensured that the EEI impedance of the fiber tip was not included. This portion of the signal path deviated from the typical metallized interconnect of other neural probes, and this setup was designed to evaluated just this additional impedance alone. The second measurement was taken from the tissue-facing tip of each fiber to its corresponding metal electrode in its channel. Essentially, this measurement includes entire signal path impedance. The interchannel impedance was measured between adjacent metal electrodes in different channels.

An LCR meter (E4980A, Keysight Technologies, Santa Rosa, CA, USA) was used to measure both the intrachannel and interchannel impedance from 20 Hz up to 10 kHz at 100 mV source voltage. A neural signal replicated from raw neural data provided by [112] and sinusoidal waves were both output from a waveform generator (33210A, Keysight Technologies, Santa Rosa, CA, USA) for simulating intrachannel and interchannel signal sources and crosstalk measurements. Interchannel crosstalk was directly measured in two steps. First, crosstalk resulting from the portion of the signal path consisting of the fiber-electrolyte-metal electrode inside the device was measured by applying the input signal directly to the tip of a single fiber and measuring the resulting signal from other channels' metal electrodes. Second, total crosstalk was measured by immersing the entire device in aCSF, applying the input signal between two external Pt wire electrodes near the exposed ends of one fiber and again measuring the resulting signal from other channels' metal electrodes. With this procedure, crosstalk could be attributed to either the device's specific internal architecture or external crosstalk due to the tissue-facing microelectrodes' proximity to one another.

6.2 Intrachannel Impedance and Crosstalk

In Fig. 6.1, the intrachannel impedance of just the fiber-aCSF-metal electrode portion of the signal path is shown for a representative device. The data is averaged over 16 channels with the standard deviation shown. The final expansion state intrachannel impedance spectrum is two orders of magnitude lower at all measured frequencies than the impedance of the dry state that acts as an open circuit control. In addition, it is within 25% of the flooded state impedance spectrum at all frequencies. This demonstrates that after the actuation process, the electrolyte effectively bridged the distal end of the fiber to the channel's substrate electrode, maintaining a low impedance signal path similar to when the entire device is in the flooded state. Furthermore, the intrachannel impedance of the fiber-aCSF-metal electrode section is over an order of magnitude smaller than the double layer impedance of a typical 7.2 µm diameter cross-section of a fiber. This is particularly significant because total intrachannel impedance increases by less than 10% when using an electrolytic bridge as opposed to a conductive physical interconnect. $C_{\mathrm{f_t}}$ dominates other series components in Fig. 5.5 due to the much larger surface areas of the metal electrode and exposed distal end of the fiber compared to the exposed fiber tip. The theoretical spectrum derived from the equivalent circuit model shown in magenta agrees with these results, as the $C_{\mathrm{f_t}}$ impedance does indeed dominate the other components. Hence, the addition of the aCSF bridge introduces two EEI impedances that are significantly smaller than the tissue-facing fiber tip EEI impedances. At 1 kHz, the mean intrachannel impedances are as follows: expansion state – 219 kΩ, flooded state – 208 kΩ, dry state – 88 MΩ, and fiber cross-section – 7 MΩ. Values calculated for the equivalent circuit are as follows: $R_{\mathrm{p}} = 20$ MΩ, $R_{\mathrm{sol}} = 200$ Ω, $R_{\mathrm{f_d}} = 5$ kΩ, $R_{\mathrm{f_t}} = 5$ kΩ, $C_{\mathrm{m}} = 100$nF, $C_{\mathrm{f_d}} = 550$ nF, $C_{\mathrm{f_t}} = 5$ nF, $C_{\mathrm{p}} = 2$pF. When looking at the phase plot of the intrachannel impedance in (Fig. 6.1), it is clear once again that the series capacitance dominates the total impedance. However, note that double layer capacitor exhibits phase behavior similar to a constant phase element rather than an ideal capacitor which is in agreement with typical empirical electrochemical measurements [133]. A non-ideality factor fit of $n = 0.65$ was used to simulated the phase plot presented in Fig. 6.1.

These results demonstrate that this recording architecture that utilizes an electrolyte to couple two electrodes only marginally increases intrachannel impedance.

6.3 Interchannel Impedance

To achieve low crosstalk between adjacent channels, the device architecture must demonstrate a high interchannel impedance in the expansion state. This ensures that the electrolytic aCSF between channels inside the shuttle has been displaced (Fig. 5.5). In Fig. 6.2, the flooded state interchannel impedance that acts as a short circuited control is less than

10% of the impedance of the expansion state at all measured frequencies and is less than 2% at 1 kHz. In addition, the expansion state interchannel impedance is within a factor of 1/3 of the dry state impedance spectrum at all frequencies. This demonstrates that as the hydrogel expands and displaces the air trapped in the chamber, the air in turn displaces the aCSF coupling adjacent channels. The discrepancy between the expansion and dry state impedances is likely explained by the unavoidable parasitic resistance of the aCSF wetting the interior of the channels, R_p. At 1 kHz, the mean interchannel impedances of each state are as follows: expansion – 32 MΩ, flooded – 617 kΩ, dry – 61 MΩ. These values are shown for a representative device averaged over 16 channels with standard deviation shown.

Fig. 6.3 shows the direct measurements of multichannel crosstalk where all measurements are normalized to the input signal amplitude and averaged. As expected, crosstalk is at its peak during the flooded state since all channels' substrate and fibers are connected by aCSF. However, after hydrogel expansion, the aCSF between channels inside the device is displaced by air as suggested by the interchannel impedance data, and crosstalk drops to less than 1.5% at all frequencies which falls within the range of reported silicon probes and is lower than flexible polymer probes [134], [135]. This suggests an SNR of over 50 V/V when considering channel-to-channel leakage. There was no discernable relationship between crosstalk magnitude and separation distance between channels (Fig. 6.4).

6.4 Fiber Tip Impedance Electroplating

After electroplating the tissue-facing cross-section of the carbon fiber, the total intrachannel impedance decreased by roughly a factor of three between 100 and 1500 Hz (Fig. 6.5). By reducing the impedance of the tip of each fiber, the intrachannel impedance of each channel decreases significantly since Cft impedance dominates, and this reduces the leakage effect due to parasitic effects through the aCSF in the channel and maximizes SNR. After electroplating, a capacitive phase is observed due to the increase in effect surface area of the double layer capacitor which is in agreement with other empirical measurements [136].

PEDOT:PSS electroplated fibers were inserted into a device flooded with aCSF and actuated until the expansion phase was reached. Outside of the device, a pair of insulated platinum wires 25 μm in diameter was used to generate an AC signal replicated from raw neural data collected by [112]. One wire was cut with a pair of surgical scissors to expose just the cross-sectional area, and the other wire was exposed to a flame to remove a bulk segment of insulation to use as the ground electrode. Using an arbitrary waveform generator to produce the replicated neural signal, the ground wire was placed several mm away from the device, and the cut wire was placed 10 μm away from each fiber tip. The cut wire was moved from on fiber tip to the next, and the signal was measured and recorded from each fiber.

There is a non-linear correlation between the tip impedance of the fibers and recorded amplitude (Fig. 6.6). Coated fibers with an impedance around 470 kΩ had a maximum amplitude 50% larger than coated fibers with 780 kΩ impedance. In addition, uncoated fibers showed about 1/3 amplitude of the 470 kΩ PEDOT coated fibers. From Fig. 6.7, PEDOT electroplating does not seem to significantly affect the frequency response below about 4 kHz which also corresponds to equivalent circuit model's RC filter cutoff frequency.

6.5 Hydrogel Actuation Force Characterization Setup

Due to the small particle size of the 30 μm sodium polyacrylate beads, complete hydration of a densely packed mass of beads is non-trivial. Once the outermost layer of beads absorbed any water, the rate of diffusion further into the mass of beads drastically decreased because the polymer network interstitial space would be filled in by local swelling (Fig. 6.8a). To reduce the day-scale expansion time for benchtop testing, 10 μm silica beads (Sigma-Aldrich, Inc., St. Louis, MO, USA) were mixed into the hydrogel. The silica acted as a hydrophilic spacer to shuttle water deeper into the densely packed beads to prevent the slowing of diffusion (Fig. 6.8b). However, a higher ratio of silica would result in quicker expansion times at the cost of maximum expansion volume. A satisfactory ratio to optimize for an hour-scale expansion time was 3:1 silica to sodium polyacrylate by volume.

In order to penetrate the tissue phantom, the hydrogel expansion must provide a minimum actuation force dependent on the number of fibers in the array given that other parameters such as fiber diameter, tip shape, and insertion speed are constant.

A small block of 0.6 w/w% agarose gel tissue phantom (LP0013T, Thermo Fisher Scientific, Waltham, MA, USA) was placed at the front side of the fully assembled device to simulate neural tissue to test hydrogel expansion under typical operating conditions. With this setup, both tissue phantom penetration and penetration depth were observed.

To estimate a lower bound actuation force using the critical buckling load model, a new fiber array was mechanically anchored to the channels by flowing epoxy into the channels. Once the hydrogel had sufficiently expanded and buckled the array, the actuation force applied by the hydrogel can be calculated using the critical buckling load. For multiple fibers in parallel, the critical buckling load can be scaled multiplicatively. This setup informs the minimum force that can be provided by the hydrogel actuation mechanism.

6.6 Actuation Dependence on Hydrogel Volume

Fig. 6.9 characterizes the actuation distance dependence on the volume of dried hydrogel/silica initially inserted into the chamber for both loaded configurations where the hydrogel is pushing a piston head and fibers, and unloaded configurations where the hydrogel is freely expanding in the chamber of the shuttle.

The results suggest that because expansion correlates roughly linearly with hydrogel volume, the hydrogel beads are expanding uniformly on average. When considering the loaded configuration slope in Fig. 6.9, for every 100 μm of tissue penetration desired, less than half that amount of dried hydrogel is required. For unloaded configurations, the expansion per unit width of hydrogel is nearly 75% higher due to a lack of Van der Waals forces between the piston head/fibers and substrate opposing the osmotic swelling force. As a hydrogel bead absorbs water, it transitions from a glassy phase to a gel-like phase, gradually reducing its swelling force until it is equal to this external Van der Waals force. At mechanical equilibrium, the hydrogel is saturated and stops swelling.

6.7 Tissue Phantom Penetration

Fig. 6.10 shows a typical post-actuation CFMEA into the agar tissue phantom. The largest penetration depth achieved into the tissue phantom was approximately 2.5 mm; significantly beyond this depth the fiber arrays are likely to buckle inside the chamber according to the model presented in [137]. Using a 3:1 silica to gel ratio, the full expansion duration lasted between two to three hours. However, qualitative observation showed that actuation speed was not constant due to an initial ramp up period lasting anywhere from 10-60 min depending on the hydrogel volume width when the aCSF was penetrating the membrane and first reaching the dry hydrogel. Once wetted, the hydrogel expansion rate was always below 1 μm/s.

6.8 Lower Bound Force Estimation

Using a new device with 1 mm long fibers fixed to the substrate with epoxy, the minimum force applied by the swelling hydrogel can be calculated using the critical buckling load for a cylindrical fiber. With radius, r, and one end fixed and one end pinned [137]:

$$P = 0.62\text{mN} \tag{6.1}$$

where P is the critical buckling load, $K = 2.046$ is the column effective length factor, $E = 234$ GPa is the Young's modulus, $I = \frac{\pi}{4}r^4 = 132\ \mu\text{m}^4$ is the area moment of inertia, and $l = 1$ mm is the unsupported length of the fiber. It is important to note that this is the minimum force that the hydrogel generates to buckle the fiber, and the total force could be larger. For an array of 16 fibers in parallel, the total critical buckling load (and thus applied force by the hydrogel) is 9.92 mN.

For a slowly penetrating ($<25\ \mu$m/s) microwires similar in diameter to carbon fibers, the peak force during insertion is expected to be about 0.15 mN [138]. Thus, the load applied onto the entire 16 fiber array is approximately 66 times the maximum force required for a single fiber to penetrate tissue. This indicates that a device with these dimensions and volume of hydrogel should be able to actuate 66 fibers concurrently.

This hydrogel force is compared with the force generated by a typical electrostatic gap closing inchworm actuator in Appendix B for comparison with more detailed analysis.

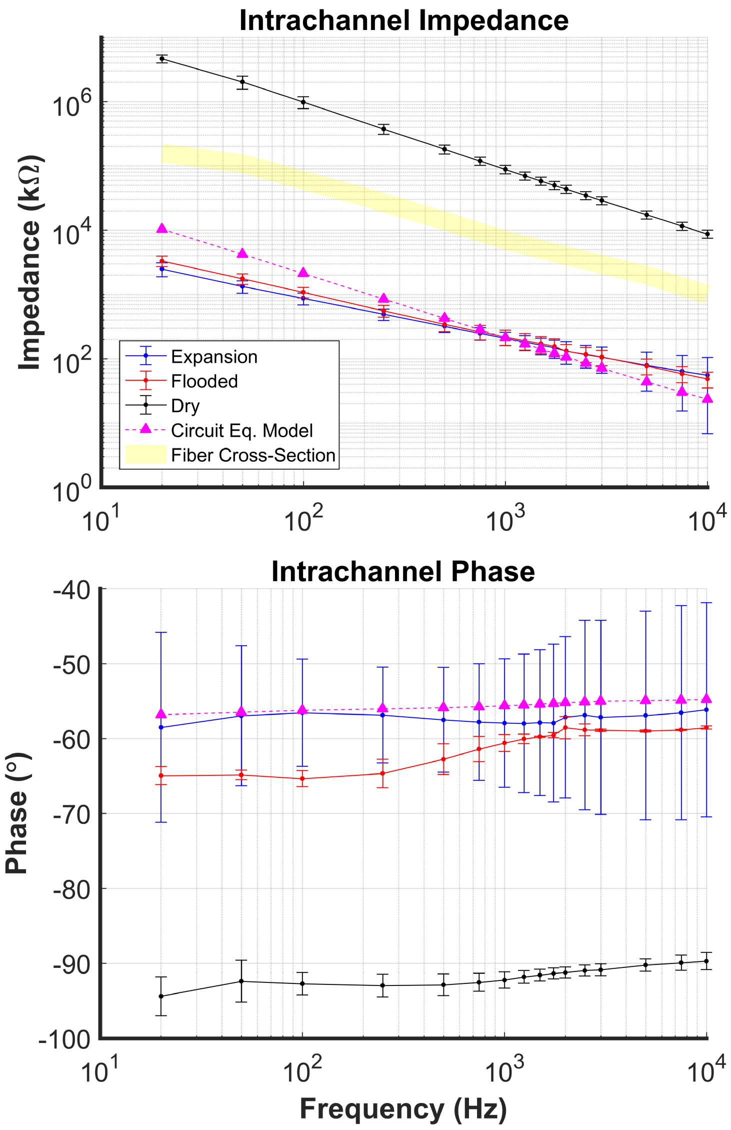

Figure 6.1: Electrical intrachannel impedance characterization for representative CMFMEA devices. Top: intrachannel impedance magnitude as a function of all device states plotted against theoretical equivalent circuit model and typical impedance range of a bare 7.2 μm diameter carbon fiber tip. Averaged over $n = 16$ channels. Bottom: intrachannel impedance phase as a function of all device states. Averaged over $n = 16$ channels.

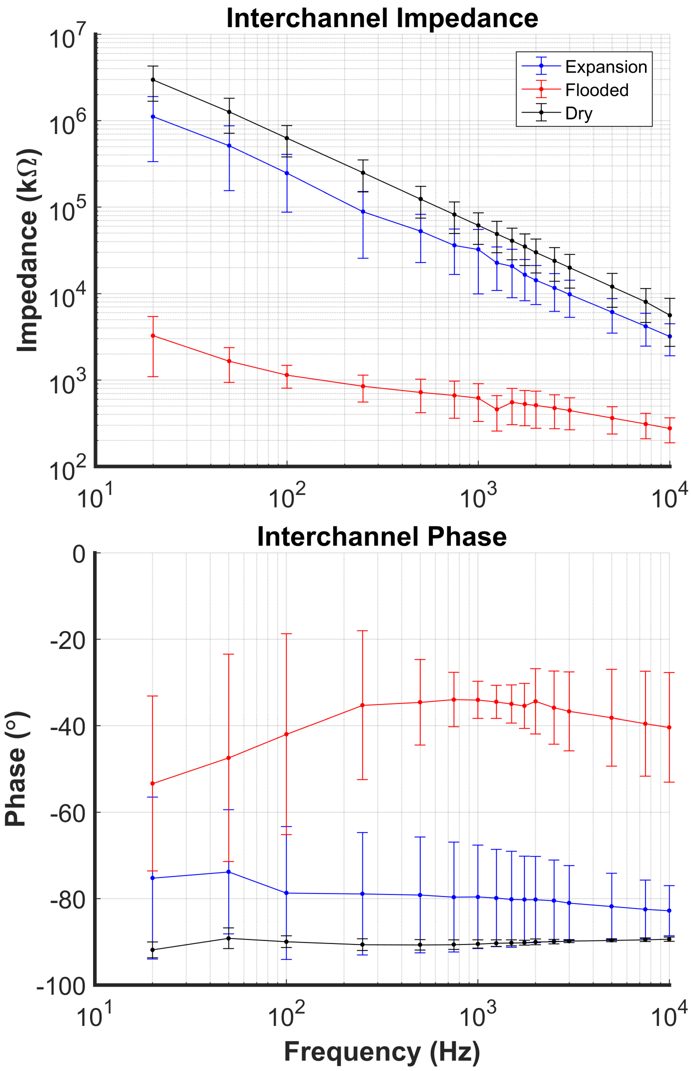

Figure 6.2: Electrical interchannel impedance characterization for representative CMFMEA devices. Top: interchannel impedance magnitude as a function of all device states. Averaged over $n = 16$ channels. Bottom: interchannel impedance phase as a function of all device states.

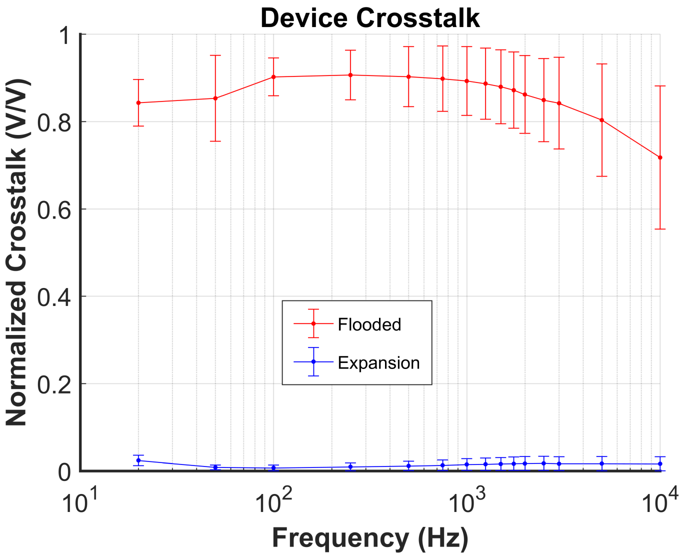

Figure 6.3: Crosstalk attributed to interchannel impedance between adjacent electrode-fiber pairs during flooded and expansion states. Averaged over $n = 4$ channels.

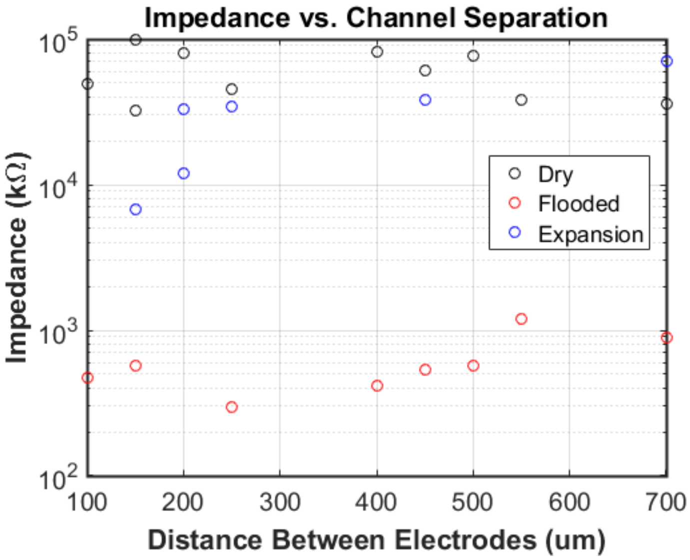

Figure 6.4: Interchannel impedance plotted as a function of separation distance between channels. Separation distance is a poor predictor of interchannel impedance.

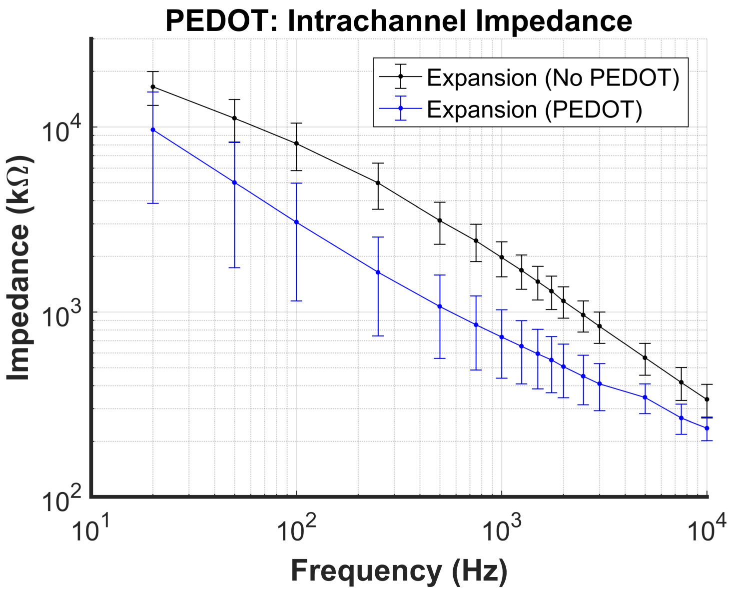

Figure 6.5: Intrachannel impedance magnitude of tissue-facing cut face before/after PEDOT electroplating. Averaged over $n = 6$ channels.

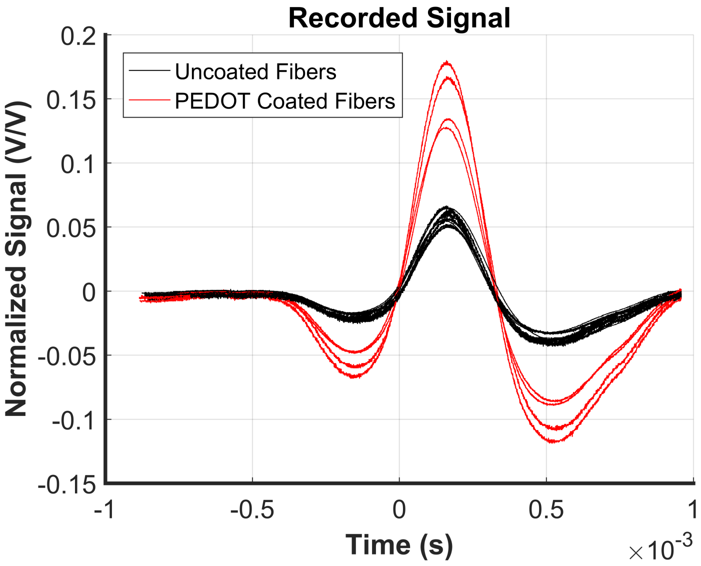

Figure 6.6: Recorded signals by uncoated fibers and PEDOT electroplated fibers.

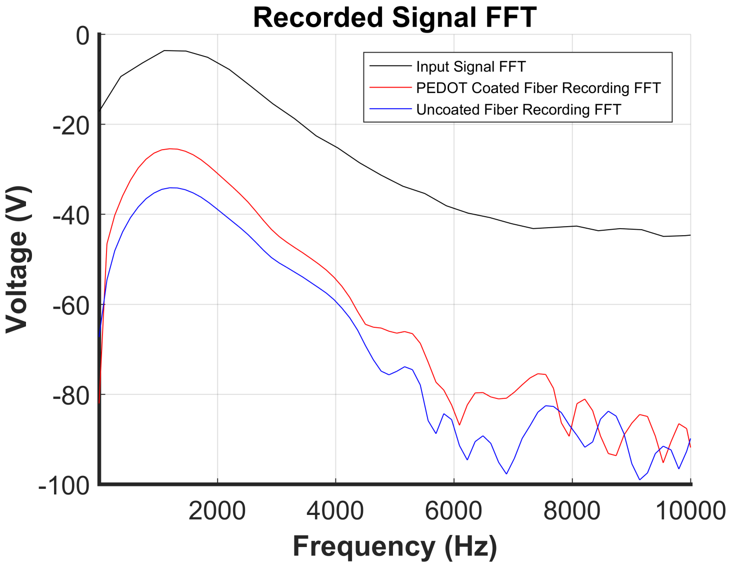

Figure 6.7: Fast Fourier transform (FFT) of representative signals recorded by PEDOT coated fiber and uncoated fiber plotted against the input signal FFT.

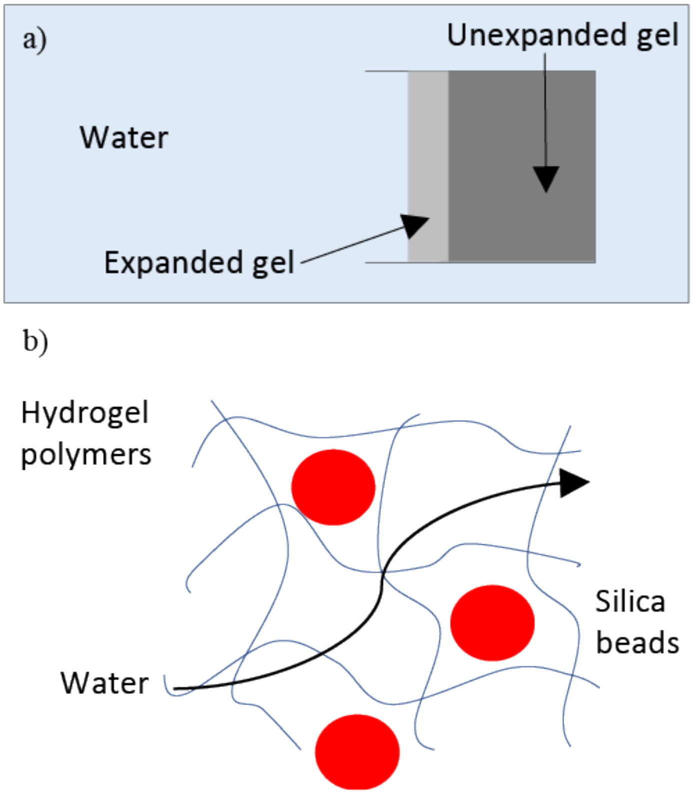

Figure 6.8: Mixing silica beads into hydrogel particles drastically decreases diffusion rate into hydrogel network and hydrogel expansion time. a) Expanded hydrogel acts as effective diffusion barrier for deeper dehydrated layers, preventing expansion within a reasonable time frame. b) Silica beads act as effective spacer to allow water to permeate hydrogel network.

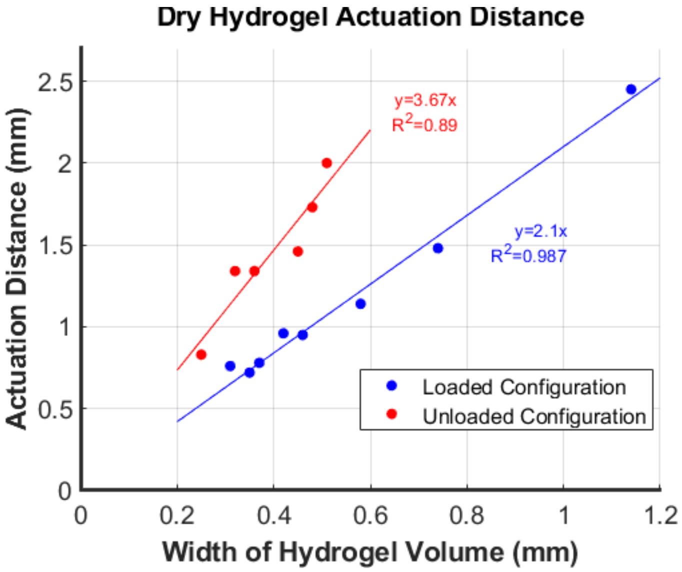

Figure 6.9: Hydrogel expansion as a function of initial dried hydrogel volume for both loaded and unloaded configurations. Width is in direction of actuation.

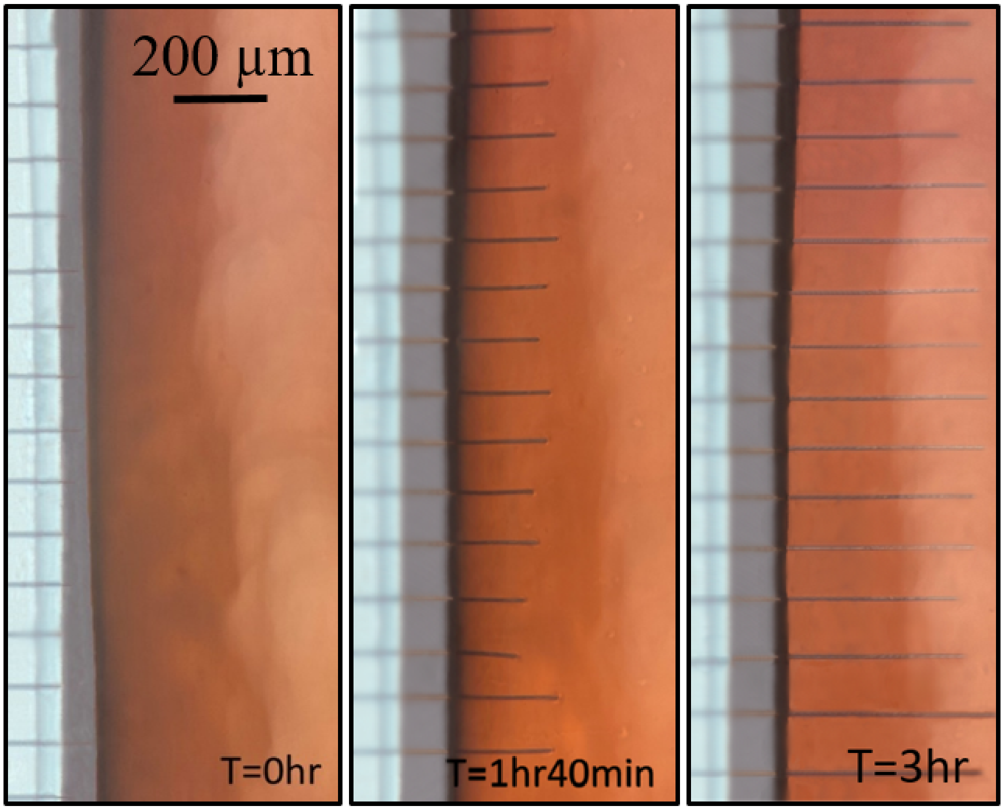

Figure 6.10: Fiber array penetration and deployment distance of approximately 550μm into 0.6% agarose gel stained with red dye for visibility. Actuation direction to the right over 3 hours. Penetration depth variations due to initial fiber length differences.

Chapter 7

Toward a Fully Scaled Neural Implant

7.1 Significant Milestones and Progress

The current iteration of this device requires optimization on several fronts to achieve true viability for chronic *in vivo* implantation and recording. In this work, we demonstrated a high-density carbon fiber array with a self-deploying, hydrogel actuation mechanism capable of inserting sixteen 7.2 μm diameter carbon fibers up to 2.5 mm deep into brain tissue phantom. We presented the microfabrication process for the device, discussed the assembly process to insert both the carbon fibers and hydrogel into the device, and highlighted the robust electrical and mechanical characteristics of the device.

This device architecture is able to passively and slowly self-deploy submicron diameter carbon fiber microelectrodes millimeters deep into tissue phantom while utilizing an electrolyte solution to bridge the gap between the fibers and the metal electrodes. The physiological cerebrospinal fluid effectively couples the fiber and metal electrode while increasing the total intrachannel impedance by less than 10%. The device is also capable of maintaining interchannel crosstalk at levels comparable to existing silicon and polymer neural probes. This method of recording and actuation, while promising, has several avenues for significant improvement to work toward a fully scaled neural implant.

7.2 Hydrogel Actuated Paradigm Advantages

This device makes use of a unique passive actuation mechanism and introduces new mechanical insertion paradigm to the field of implantable neural probes. Hydrogel actuation not only provides enough actuation force and penetration depth, but also does so completely passively at ultralow speeds. Because the hydrogel expansion does not begin until some time after submersion in cerebrospinal fluid, the microelectrode actuation and deployment can take place after closing the surgical wound and implantation of the devices. If microelectrode deployment must be completed during the surgery itself like for other CFMEA or silicon probes, it requires higher insertion speeds >1 μm/s up to several mm/s. This leads to more tissue and vascular damage which is associated with a reduction in SNR and an increase in of separable single-unit activity [139]. This device can achieve actuation speeds (100 nm/s) significantly lower than previous reported methods, and may provide another avenue for reduced gliosis and neuronal distress.

Another issue that exists across many types of neural probes is limited recording within a very small volume of tissue close to the implantation site, especially for those without self-deploying microelectrodes like the Michigan probe. For traditional CFMEAs and the Utah array, sampling neurons from a wide area requires a wide substrate. This actuation design could be modified using multiple smaller chambers and piston heads to take advantage of the isotropic expansion of the hydrogel to actuate arrays of fibers in multiple directions either 100s of microns or several millimeters away from the implant location (Fig. 7.1).

7.3 Hydrogel Actuated Paradigm Limitations

However, a limitation of hydrogel actuation is the minimum chamber width is equal to the desired maximum actuation distance in order to store the length of fiber. A scalable MEMS actuation source like hydrogels could be the key to enabling large deployment distances for microelectrode arrays.

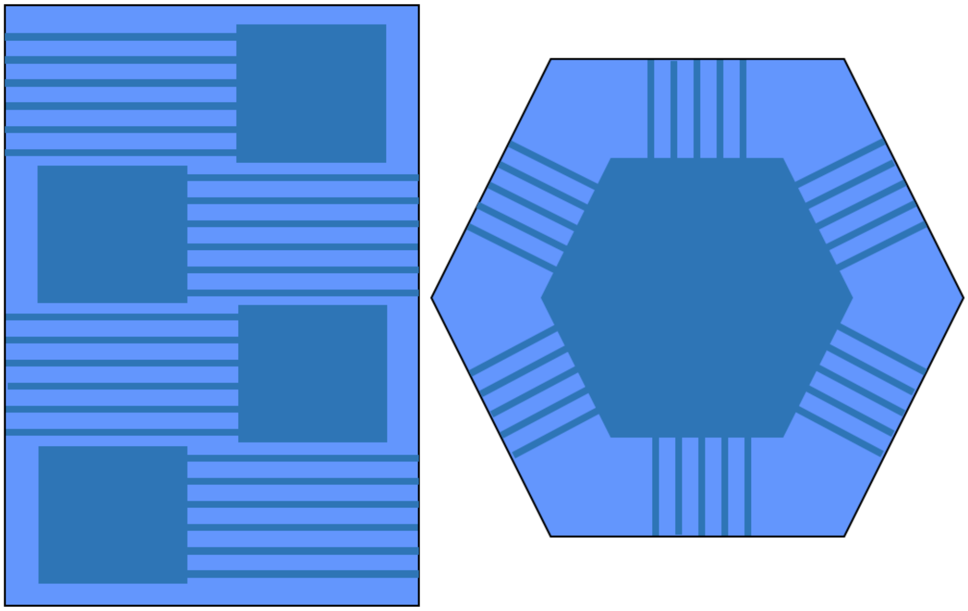

Figure 7.1: Simple two mask layouts to enable a) bidirectional actuation or b) isotropic actuation. Light blue – substrate, dark blue – etch masks.

As mentioned previous the use of hydrogel polymers in neural implants introduces many microfabrication and assembly limitations. Because these polymers tend to have high vapor pressures, they sublimate appreciably at low vacuum pressures typically required for a majority of microfabrication processes. This may contaminate shared tools and equipment as well as prevents additional fabrication steps after the hydrogel is added. There exists very few standard microfabrication compatible physical or chemical deposition processes for common hydrogels. Spin coating water-saturated gels into the chambers tends to deposit an insufficient mass of gel into the chamber to actuate fibers. The most feasible method to place hydrogels into the chamber was to simply create a back side opening large enough to fit hydrogel beads by pushing with a probe tip. This places an additional size constraint on the hydrogel particles. The beads must be at least two to three times smaller in diameter compared to the depth of the chamber to allow sufficient room to expand. Creating beads in the low 10s of μm size range via mechanical grinding techniques like jet milling and ball milling proved to be difficult due to the soft polymers elastically deforming rather than breaking into smaller particles. Hence, we were limited to hydrogel particles that were commercially available in that size range. Injection of UV cross-linking hydrogels or dried hydrogel beads in an organic solvent suspension into the chamber using a microdispenser may be a more scalable method for inserting hydrogels into microfabricated devices in future.

In this work, we used sodium polyacrylate for its commercial availability and suitable particle size, but any biocompatible hydrogel can be used. In fact, cellulose-based hydrogels have shown swelling capabilities over 100× what we demonstrated [99] and could be characterized in the future for increased actuation potential with smaller initial volumes of dried hydrogel. When choosing a hydrogel for microelectrode actuation, volumetric size increase, osmotic force output, biocompatibility, particle size, and possible microfabrication compatibility are all essential to consider.

7.4 Towards Scalability

Advancing scalability and device performance to move toward a platform that can support thousands of densely packed recording electrodes with high spatial resolution, full-volume sampling, and minimal long-term biological damage is the next step toward a truly efficacious and safe neural implant. These optimizations range from microfabrication to assembly considerations, many of which were touched on in previous chapters. The microfabrication process and layout advances will be discussed first, followed by chip size minimization.

Monolithic fabrication can improve scalability of wafer-level batch manufacturing by shifting to silicon-based microelectrodes. An SOI wafer with the fibers and piston head being replaced by a single mask process to etch the device layer to produce connected silicon needle microelectrodes would be a monolithic process, requiring additional metallization and passivation steps. This change in processing would remove the need to hand assemble the piston head and carbon fibers. Given that these two assembly steps are both serial in nature as the number of devices and channels increase, eliminating them and replacing them at the wafer scale would drastically improve the scalability of assembly. However, due to the aforementioned microfabrication incompatibility of hydrogel deposition, this step would likely remain as a post-fabrication assembly step.

Wafer-scale fabrication of microelectrodes would likely be difficult if large actuation depth is needed as silicon is more brittle than carbon fiber composites. Because carbon fiber is stiffer with regards to its Young's modulus, it has a greater critical buckling load to support larger actuation distances considering the silicon microelectrodes would still need to be subcellular in width and thickness to prevent gliosis. In addition, this would require a several step etch through the device layer, buried oxide layer, and handle wafer to hollow out the chamber since the device layer would be too thin to accept hydrogel particles of 30µm diameter. On the other hand, in-situ carbon fiber microfabrication through CVD growth is typically difficult [140], [141] so it is still unclear whether carbon fiber microelectrodes or silicon microelectrodes will have better performance with fewer scalability tradeoffs.

Another microfabrication change that should be investigated is whether the channel dimensions can be altered in such a way to allow the fibers to be considered truly free-floating with respect to the silicon shuttle. Unanchored carbon fibers can partially avoid lateral micromotions relative to the tissue that cause chronic inflammation they have penetrated even if the silicon shuttle itself is anchored to the skull or sitting above the brain (Fig. 7.2). Typical micromotions caused by respiration, vascular activity, and general body movements are between 1-25 µm. The fibers' relative motion can be reduced if the gap between the fiber and channel is larger, allowing for the fiber to move laterally within its channel. However, this obviously introduces a design tradeoff by decreasing R_{p} in Fig. 5.5 which increases channel leakage and crosstalk. However, as discussed briefly before, significantly lowered electrode impedance through electroplating can mitigate the effects of parasitic resistance. For every 2× decrease in impedance at the tip of the fiber microelectrodes, this would allow a $\sqrt{2}\times$ increase in channel width. Likely a full 25 µm width channel would not be possible, but there is room for optimization.

This device demonstrated a 16 channel CFMEA, but mechanical characterization results indicates that a larger array of at least 66 channels is possible. In fact, the upper bound on the number of channels is likely to be even larger as the force estimate was a conservative lower bound value. Generally, small pitches for large arrays is extremely difficult to achieve due to the hand assembly process for carbon fibers and limits microelectrode density, but this silicon channel architecture could support small pitches between channels down to the single micron or 100s of nm range. However, the time needed to serially load large numbers of fibers and cut them to precise lengths scales linearly with the number of channels and has been a limiting step in the assembly process for all CFMEAs. Automated robotics have been shown manipulating micron-scale flexible threads [142], [143], but a widely accessible solution has not yet become available.

From a size perspective, the device can be further optimized to minimize implantation footprint. The width of the device is limited by the number of channels and channel pitch. For a ultrahigh density device with 66 channels and 10 µm pitch, this would result in a 660 µm minimum width. The length of the device is limited by the length of the carbon

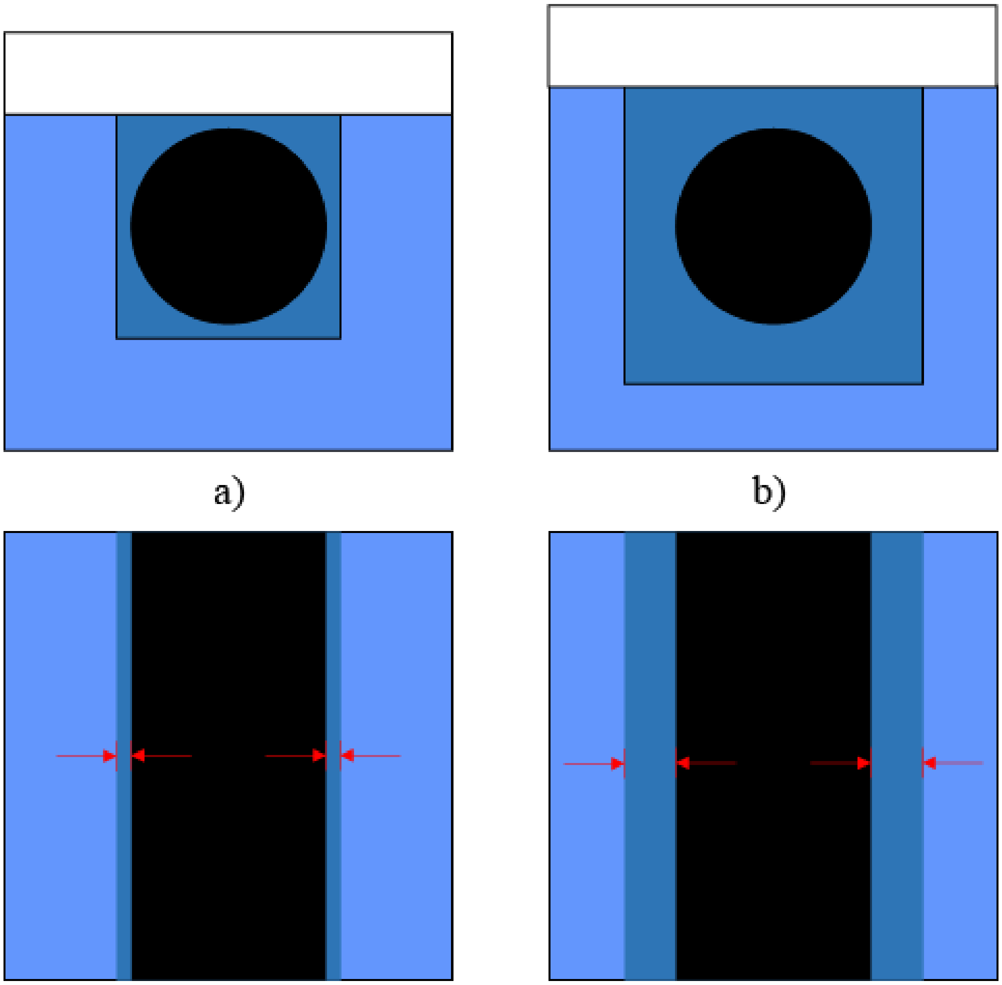

Figure 7.2: Wider channels creates more lateral space for fibers to move independently of shuttle. Light blue – bottom substrate, dark blue – etch masks, white – top substrate, and black – fiber. a) Fiber diameter and channel width nearly identical. Relative micromotion of shuttle likely to drag fiber and cause scarring. b) Fiber diameter significantly wider than channel width. Micromotion of shuttle can be independent to fiber to reduce scarring.

fibers, piston head, and hydrogel volume width. However, the entire length of the silicon shuttle may not need to be implanted entirely into the brain as it is only necessary to allow the channel openings to be placed at or in the surface of the tissue. The thickness of the device is limited by the insertion process as the device needs to be thick enough to penetrate tissue if an insertion aid is not used; alternatively, thinner devices could be stacked with each layer deploying fibers a different depth into tissue while simultaneously meeting rigidity requirements.

7.5 Final Remarks

We have presented a hydrogel actuated 16 channel carbon fiber microelectrode array and characterized its novel mechanical and electrical performance. We showed that an array of fibers can successfully penetrate agarose brain tissue phantom at a range of depths from hundreds of microns to several millimeters without buckling. Using the critical buckling load model, we determined that the number of channels can be scaled up even further. We presented an equivalent circuit model to characterize the intrachannel impedance of the electrolytic signal coupling from unanchored fibers to substrate electrodes as well as possible current leakage paths. Then, we showed that the fiber-aCSF-metal electrode segment of the signal path negligibly increases the intrachannel impedance and should not degrade the recording capabilities of the device in any significant way. Finally, we confirmed that the multichannel crosstalk of this recording architecture is comparable to existing silicon probes and carbon fiber microelectrode arrays.

Neural probes that avoid gliosis through either ultraflexible or ultrasmall microelectrodes are slowly becoming the gold standard for chronic implantation. This device provides a novel recording paradigm combining the strengths of microfabricated silicon and carbon fiber probes for brain-machine interfaces. Furthermore, this device demonstrates a microfabrication and assembly process compatible with passive, self-deploying hydrogel polymers. This work presents a path toward a scalable, chronically implantable microelectrode array with the potential for isotropic actuation, ultrahigh density, and completely unanchored electrodes for a wide variety of clinical applications and research thrusts.

Appendix A

Microfabrication Recipes

All microfabrication processing done at the Marvell Nanofabrication Laboratory at University of California, Berkeley. Optional steps in each process are shown in grey.

Table A.1: Wafer Clean

Process Step	**Tool**	**Description**
Photoresist removal	msink1/2	80°C 1165 remover bath for 10 min to strip photoresist.
Piranha clean	msink6/8	120°C sulfuric acid based piranha bath for 10 min to remove organics
Quick dump rinse (QDR)	msink6/8	Deionized water (DI) rinse and quick dump
Hydrofluoric acid clean (HF)	msink6/8	Dilute 25:1 HF bath for 1 min to remove native oxide
QDR	msink6/8	DI rinse and quick dump
Hydrochloric acid clean (HCl)	msink6/8	Dilute 1000:1 HCl bath for 1 min to remove metals
QDR	msink6/8	DI rinse and quick dump
Spin rinse dry (SRD)	msink6/8	DI rinse and dry cycle

Table A.2: Thin Photoresist (PR) Lithography

Process Step	**Tool**	**Description**
Coat lift-off resist	svgcoat3	1 μm LOR-5A. Coat at 1000 rpm for 30 sec. 190°C contact softbake for 140 sec.
Coat i-line PR	picotrack1	2 μm AZ MiR 701. Hexamethyldisilazane (HMDS) adhesion promoter bake at 100°C for 30 seconds. 10 sec cool. Coat at 4000 rpm for 15 sec. 90°C contact softbake for 90 sec.
Expose i-line PR	ksaligner	15 mW/cm^2 exposure intensity for 12 sec.
Develop i-line PR	picotrack2	110°C post-exposure bake (PEB) for 90 sec. MF-26A puddle develop for 60 sec.
Descum PR	technics-c	180 mTorr O_2 process pressure. 50 W power for 1 min.
Hard bake i-line PR	oven	120°C hard bake for 30 min.

Table A.3: Thick Photoresist (PR) Lithography

Process Step	**Tool**	**Description**
Coat broadband PR	picotrack1	8 μm AZ P4620. HMDS adhesion promoter bake at 100°C for 30 seconds. 10 sec cool. Coat at 4150 rpm for 30 sec. 110°C proximity softbake for 80 sec. Rest at 20-70% humidity for 30 min.
Expose broadband PR	ksaligner	15 mW/cm^2 exposure intensity for 35 sec.
Develop broadband PR	picotrack2	Repeat MF-26A puddle develop for 60 sec twice.
Descum PR	technics-c	180 mTorr O_2 process pressure. 50 W power for 1 min.
Hard bake i-line PR	oven	90°C hard bake for 30 min.

Table A.4: Metal Evaporation and Lift-Off

Process Step	Tool	Description
Lift-off lithography	Various	See Table A.2.
Evaporate Ti	cha	10 nm Ti at 4 Å/s deposition rate
Evaporate Pt	cha	100 nm Pt at 2 Å/s deposition rate
Lift-off metals	asap-liftoff	N-Methyl-2-pyrrolidone (NMP) soak for 2 min. Pressurized NMP jet abrasion at 8 MPa and spin dry at 1000 rpm

Table A.5: Silicon Dioxide Plasma Enhanced Chemical Vapor Deposition (PECVD)

Process Step	Tool	Description
Lithography	Various	See Table A.2.
Deposit SiO_2	oxford2	800 sccm N_2O and 100 sccm 10% SiH_4/Ar gas flow and 900 mTorr process pressure. 25W power at 200°C. 15 minutes per 1 µm.
Wafer clean	Various	See Table A.1.

Table A.6: Chemical-Mechanical Polishing (CMP)

Process Step	Tool	Description
Planarize surface	gnpcmp	Silica nanoparticle and KOH slurry. Table spin speed 20 rpm, head spin speed 19 rpm, and 80 g/cm^2 pressure. 400 seconds per 800 nm.
Etch nanoparticles	msink16/18	Dilute 25:1 HF bath for 5 sec to remove native oxide.
Wafer clean	Various	See Table A.1.

Table A.7: SiO_2 Reactive Ion Etch (RIE)

Process Step	**Tool**	**Description**
Lithography	Various	See Table A.2.
RIE etch SiO_2	ptherm	4 sccm O_2 and 80 sccm CHF_3 gas flow and 0.9 Torr process pressure. 150 W for 150 seconds per 200 nm.
Wafer clean	Various	See Table A.1.

Table A.8: Si Deep Reactive Ion Etch (DRIE)

Process Step	**Tool**	**Description**
SiO_2 hard mask deposition	oxford2	See Table A.5.
Lithography	Various	See Table A.3.
SiO_2 hard mask etch	ptherm	See Table A.7.
DRIE etch Si	sts2	6 second C_4F_8 (80 sccm) passivation and 11 second SF_6/O_2 (200 sccm) etch cycles. 11 cycles per 10 μm.
Wafer clean	Various	See Table A.1.

Table A.9: Thermal Oxide Growth

Process Step	**Tool**	**Description**
Wafer clean	Various	See Table A.1.
Thermal oxide growth	tystar3/4	Wet oxide growth at 950°C. 23 hours per 2 μm.

Table A.10: Direct Wafer Bonding

Process Step	**Tool**	**Description**
Wafer clean	Various	See Table A.1.
Radical assisted direct bond	aml-bonder	750 mTorr O_2 process pressure. 5 minute plasma activation at 500 V, 150 mA. 280 N applied force at 350°C. 2 hour bond time.
Anneal	vacoven	200 Torr N_2 process pressure. 450°C for 3 hours bond time.

Table A.11: Vapor HF Release

Process Step	**Tool**	**Description**
Wafer bake	hotplate	Bake at 250°C for 2 min to drive off adsorbed polymers from wafer box.
Oxide etch	primaxx	400 sccm ethanol and 525 sccm HF gas flow at 125 Torr process pressure. 10 min etch cycles. 13 cycles per 11.7 μm.

Table A.12: Parylene-C Insulation

Process Step	**Tool**	**Description**
Parylene deposition	parylene	1 μm thick layer per 1.6 g of dimer. 135°C process temperature until all dimer pyrolyzed.

Appendix B

Comparison With Inchworm Motors

It is important to put the mechanical actuation force of hydrogels at these micron to millimeter scales in context of traditional MEMS actuation methods. Hydrogels force densities generated in this work are compared to those of inchworm motors powered with electrostatic gap closing actuators in air.

This work reports a typical chamber volume of 55 µm×4000 µm×3000 µm. A majority of this volume is required due to the stroke distance of the piston head. When this stroke distance and bulk piston head width is subtracted, the minimum chamber dimension are roughly 55 µm×1000 µm×3000 µm. However, the larger of these two volumes will be considered for chip area to provide a conservative force comparison.

The inchworm architecture used in this calculation will be similar to [93] with two pairs of gap closing actuators (GCAs) at each end of the fiber (Fig. B.1). All volume occupied by the silicon shuttle, drive pads, spring-anchors, sense stops, etc. will be ignored for simplicity: the entire chamber volume will be dedicated to the capacitive fingers. Other gap closing actuator parameters have been adapted from [144] (Fig. B.1). These parameters are shown in Table B.1.

The electrostatic capacitive force of each GCA is given as:

$$F = \frac{1}{2} N \epsilon_o \epsilon_r l_\mathrm{f} t_\mathrm{f} V^2 \Big(\frac{1}{(g_o - x)^2} - \frac{1}{(g_b + x)^2} \Big) \tag{B.1}$$

For the parameters assumed, this yields a maximum force of

$$F = 2.4\mathrm{mN} \tag{B.2}$$

Assuming that this entire force is applied to the fiber (though likely this force will be non-parallel at some angle θ and scaled at $F \sin\theta$), each pair of GCAs applies a total of 4.8 mN at 50 V. Given that the penetration force needed per fiber is 0.15 mN, a total of 32 fiber microelectrodes could be inserted. In Figure B.2, the force generated by a single GCA is plotted against the penetration force necessary for insertion. Note that a single fiber requires 0.15 mN and a 16 fiber array requires 2.4 mN insertion force. Given that a pair of

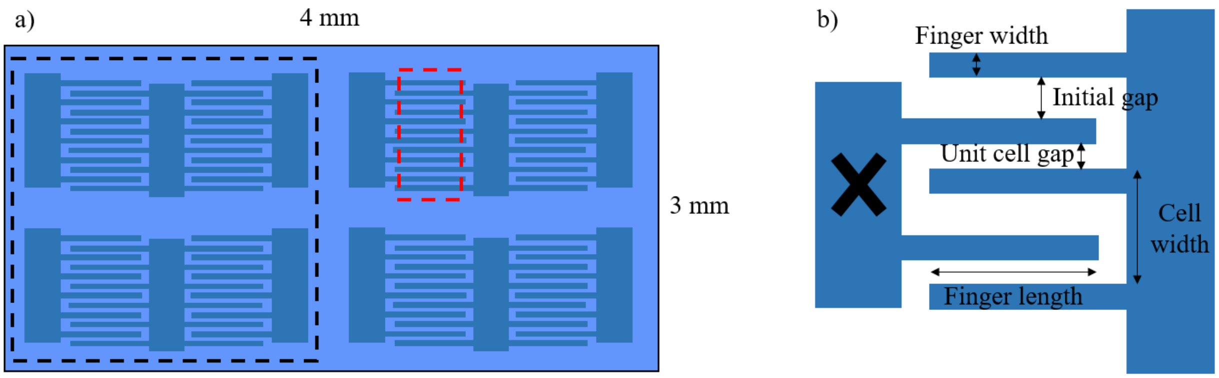

Figure B.1: Diagrams of inchworm motor and gap closing actuators. a) Chamber filled with two pairs of gap closing actuators to generate inchworm actuation. Black dashed box contains a single pair of GCAs. Red dashed box shows the capacitive interdigitated fingers. b) Two GCA unit cells shown with relevant parameters labelled.

GCAs together must generate this total force, each GCA needs to contribute 0.075 mN and 1.2 mN, respectively.

At this specific chamber size, hydrogels can generate a larger actuation force compared to a pair of GCAs for all voltages <67 V. Above this applied voltage, the inchworm motor can generate a larger electrostatic force. It is important to note that the total electrostatic force scales quadratically with voltage and linearly with any one chamber dimension (chamber width scales with finger length, chamber length scales with the number of GCA unit cells, and chamber depth scales with finger thickness). Hydrogel actuation scales linearly with chamber depth and length, but not width (1 mm wide and 5 mm wide mass of hydrogel particles will generate the same amount of force but varying actuation distances). Thus, if the chip can be fabricated at very small sizes, the hydrogel paradigm will generate large forces, but if the chip size is larger, the electrostatic paradigm will be advantageous.

Note that the electrostatic force of the GCA can be significantly increased by operating the motor in CSF as its relative permittivity is roughly 80. This can reduce the operating voltage requirement or chip area immensely, both by a factor of $\sqrt{80}$. Though it would increase squeeze film damping effects and increase pull-in time, these insertion speed considerations likely not affect overall recording and device performance. However, if electrodes are exposed to CSF, care must be taken to avoid excess current leakage due to several factors. First, this increases total power consumption of devices. Second, depending on the amplitude and frequency of the voltage, this could cause hydrolysis. This is relatively unlikely given that AC signals are being used and DC voltages primarily cause hydrolysis, but at lower frequencies and high voltages, AC signals can still evolve hydrogen and oxygen gas at electrode sites causing corrosion. Even if hydrolysis is avoided, current leakage could still affect

Table B.1: Inchworm Motor Parameters

Parameter	**Value**	**Description**
Chamber width, w_{ch}	3000 µm	Lateral dimension of chamber
Chamber length, l_{ch}	4000 µm	Longitudinal dimension of chamber
GCA width, w_{gca}	1500 µm	Half of chamber width. Lateral distance allotted to one GCA in each pair
GCA length, l_{gca}	2000 µm	Half of chamber length. Longitudinal distance allotted to one GCA
Finger width, w_{f}	5 µm	Width of each finger of the GCAs [144]
Finger thickness t_{f}	50 µm	Thickness of each finger of the GCAs determined by the chamber etch depth
Finger length, l_{f}	750 µm	Length of each finger of the GCAs, also assumed to be the overlap length
Initial gap, g_{o}	5 µm	Gap between finger and ground electrode when no voltage is applied [144]
Unit cell gap, g_{b}	8 µm	Gap between unit cells [144]
Cell width, w_{c}	23 µm	Width of each pair of fingers calculated as $2\times w_{\mathrm{f}} + g_{\mathrm{o}} + g_{\mathrm{b}}$
Number of GCA cells, n	118	Number of total cells per GCA calculated as $2\times l_{\mathrm{gca}}/w_{\mathrm{c}}$
Voltage, V	50 V	Zero to peak amplitude of AC signal applied to fingers [144]
Gap stop distance, x_{min}	1 µm	Minimum distance between finger and gap stop [144]

neurons in the vicinity of the electrodes though this effect still remains to be characterized precisely.

Electrostatic inchworm motors still have several clear cut advantages over hydrogels. These devices can be microfabricated monolithically, boosting better scalability over hand-loading hydrogels and piston heads. Especially at high channel counts and production-scale volumes, this can contribute to a large difference in device manufacturing. In addition, inchworm motors can generate a constant, controllable force over the course of actuation, but hydrogels have a non-linear force vs. distance curve. The self-deployment can be done

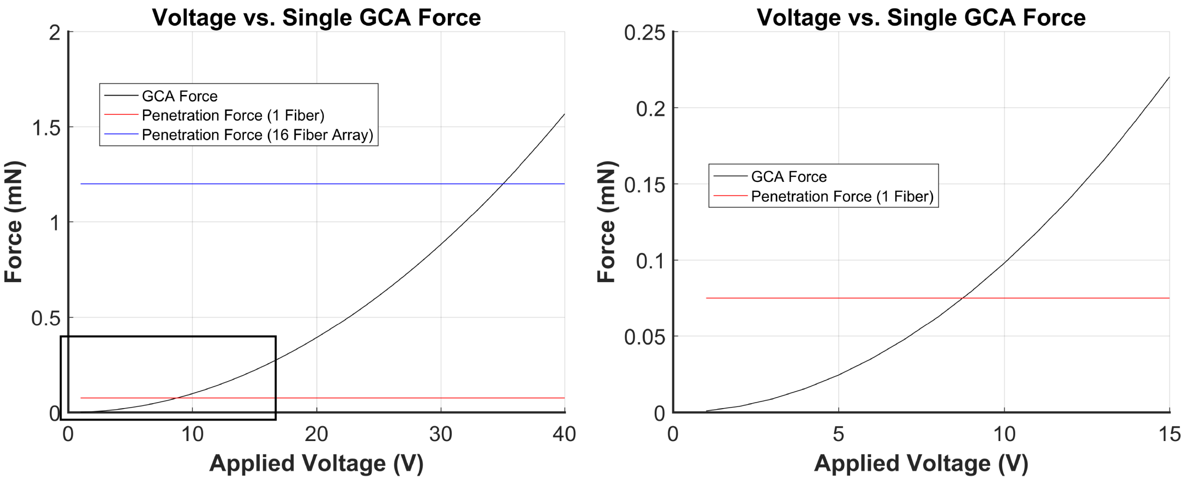

Figure B.2: The maximum electrostatic force generated by a single GCA scales quadratically with voltage. For the assumed parameter values in Table B.1, a voltage of 35 V is needed to actuated 16 fibers and 8.8 V for a single fiber. These voltages are derived noting that a pair of GCAs is used to actuate rather than just a single GCA.

at any time and at various speeds supported by the operating frequency compared to the hydrogel actuation mechanism which is much more difficult to control precisely.

Bibliography

[1] G. Buzsáki, “Large-scale recording of neuronal ensembles,” *Nature neuroscience*, vol. 7, no. 5, pp. 446–451, 2004.

[2] D. Tampellini, “Synaptic activity and alzheimer’s disease: A critical update,” *Frontiers in neuroscience*, vol. 9, p. 423, 2015.

[3] U. B. Eyo, M. Murugan, and L.-J. Wu, “Microglia–neuron communication in epilepsy,” *Glia*, vol. 65, no. 1, pp. 5–18, 2017.

[4] A. Sehgal and E. Mignot, “Genetics of sleep and sleep disorders,” *Cell*, vol. 146, no. 2, pp. 194–207, 2011.

[5] T. Andrillon, Y. Nir, C. Cirelli, G. Tononi, and I. Fried, “Single-neuron activity and eye movements during human rem sleep and awake vision,” *Nature communications*, vol. 6, no. 1, pp. 1–10, 2015.

[6] N. Y. Masse, M. C. Rosen, and D. J. Freedman, “Reevaluating the role of persistent neural activity in short-term memory,” *Trends in cognitive sciences*, vol. 24, no. 3, pp. 242–258, 2020.

[7] S. Mullen Raymond, “Neural foundations of creativity: A systematic review,” *Revista colombiana de psiquiatria*, vol. 46, no. 3, pp. 187–192, 2017.

[8] S. Herculano-Houzel, “The human brain in numbers: A linearly scaled-up primate brain,” *Frontiers in human neuroscience*, p. 31, 2009.

[9] J. W. Salatino, K. A. Ludwig, T. D. Kozai, and E. K. Purcell, “Glial responses to implanted electrodes in the brain,” *Nature biomedical engineering*, vol. 1, no. 11, pp. 862–877, 2017.

[10] K. L. Moore, A. F. Dalley, and A. M. Agur, *Clinically oriented anatomy*. Lippincott Williams & Wilkins, 2013.

[11] G. Hong and C. M. Lieber, “Novel electrode technologies for neural recordings,” *Nature Reviews Neuroscience*, vol. 20, no. 6, pp. 330–345, 2019.

[12] D. A. Henze, Z. Borhegyi, J. Csicsvari, A. Mamiya, K. D. Harris, and G. Buzsaki, “Intracellular features predicted by extracellular recordings in the hippocampus in vivo,” *Journal of neurophysiology*, vol. 84, no. 1, pp. 390–400, 2000.

[13] Y. Kajikawa and C. E. Schroeder, "How local is the local field potential?" *Neuron*, vol. 72, no. 5, pp. 847–858, 2011.

[14] J. Makarova, T. Ortuño, A. Korovaichuk, *et al.*, "Can pathway-specific lfps be obtained in cytoarchitectonically complex structures?" *Frontiers in systems neuroscience*, vol. 8, p. 66, 2014.

[15] S. Jäkel and L. Dimou, "Glial cells and their function in the adult brain: A journey through the history of their ablation," *Frontiers in cellular neuroscience*, vol. 11, p. 24, 2017.

[16] Y. Wu, L. Dissing-Olesen, B. A. MacVicar, and B. Stevens, "Microglia: Dynamic mediators of synapse development and plasticity," *Trends in immunology*, vol. 36, no. 10, pp. 605–613, 2015.

[17] H. K. Kimelberg and M. Nedergaard, "Functions of astrocytes and their potential as therapeutic targets," *Neurotherapeutics*, vol. 7, no. 4, pp. 338–353, 2010.

[18] L. F. Nicolas-Alonso and J. Gomez-Gil, "Brain computer interfaces, a review," *sensors*, vol. 12, no. 2, pp. 1211–1279, 2012.

[19] J. J. Shih, D. J. Krusienski, and J. R. Wolpaw, "Brain-computer interfaces in medicine," in *Mayo clinic proceedings*, Elsevier, vol. 87, 2012, pp. 268–279.

[20] M. B. Khalid, N. I. Rao, I. Rizwan-i Haque, S. Munir, and F. Tahir, "Towards a brain computer interface using wavelet transform with averaged and time segmented adapted wavelets," in *2009 2nd international conference on computer, control and communication*, IEEE, 2009, pp. 1–4.

[21] S. D. Stavisky, J. C. Kao, P. Nuyujukian, S. I. Ryu, and K. V. Shenoy, "A high performing brain–machine interface driven by low-frequency local field potentials alone and together with spikes," *Journal of neural engineering*, vol. 12, no. 3, p. 036 009, 2015.

[22] C. I. Penaloza and S. Nishio, "Bmi control of a third arm for multitasking," *Science Robotics*, vol. 3, no. 20, eaat1228, 2018.

[23] A. V. Nurmikko, J. P. Donoghue, L. R. Hochberg, *et al.*, "Listening to brain microcircuits for interfacing with external world—progress in wireless implantable microelectronic neuroengineering devices," *Proceedings of the IEEE*, vol. 98, no. 3, pp. 375–388, 2010.

[24] G. Buzsáki, C. A. Anastassiou, and C. Koch, "The origin of extracellular fields and currents—eeg, ecog, lfp and spikes," *Nature reviews neuroscience*, vol. 13, no. 6, pp. 407–420, 2012.

[25] J.-r. Choi, S.-M. Kim, R.-H. Ryu, S.-P. Kim, and J.-w. Sohn, "Implantable neural probes for brain-machine interfaces–current developments and future prospects," *Experimental neurobiology*, vol. 27, no. 6, p. 453, 2018.

[26] A. J. Casson, “Wearable eeg and beyond,” *Biomedical engineering letters*, vol. 9, no. 1, pp. 53–71, 2019.

[27] D. Shin, H. Watanabe, H. Kambara, *et al.*, “Prediction of muscle activities from electrocorticograms in primary motor cortex of primates,” *PloS one*, vol. 7, no. 10, e47992, 2012.

[28] P. Ledochowitsch, E. Olivero, T. Blanche, and M. M. Maharbiz, “A transparent μecog array for simultaneous recording and optogenetic stimulation,” in *2011 Annual International Conference of the IEEE Engineering in Medicine and Biology Society*, IEEE, 2011, pp. 2937–2940.

[29] R. Muller, H.-P. Le, W. Li, *et al.*, “A minimally invasive 64-channel wireless μecog implant,” *IEEE Journal of Solid-State Circuits*, vol. 50, no. 1, pp. 344–359, 2014.

[30] D. Khodagholy, J. N. Gelinas, T. Thesen, *et al.*, “Neurogrid: Recording action potentials from the surface of the brain,” *Nature neuroscience*, vol. 18, no. 2, pp. 310–315, 2015.

[31] P Ledochowitsch, R. Félus, R. Gibboni, A Miyakawa, S Bao, and M. Maharbiz, “Fabrication and testing of a large area, high density, parylene mems μecog array,” in *2011 IEEE 24th International Conference on Micro Electro Mechanical Systems*, IEEE, 2011, pp. 1031–1034.

[32] B. Rubehn, C. Bosman, R. Oostenveld, P. Fries, and T. Stieglitz, “A mems-based flexible multichannel ecog-electrode array,” *Journal of neural engineering*, vol. 6, no. 3, p. 036 003, 2009.

[33] C. A. Kuliasha and J. W. Judy, “In vitro reactive-accelerated-aging assessment of anisotropic conductive adhesive and back-end packaging for electronic neural interfaces,” in *2019 41st Annual International Conference of the IEEE Engineering in Medicine and Biology Society (EMBC)*, IEEE, 2019, pp. 3766–3769.

[34] E. Patrick, M. E. Orazem, J. C. Sanchez, and T. Nishida, “Corrosion of tungsten microelectrodes used in neural recording applications,” *Journal of neuroscience methods*, vol. 198, no. 2, pp. 158–171, 2011.

[35] E. McGlynn, V. Nabaei, E. Ren, *et al.*, “The future of neuroscience: Flexible and wireless implantable neural electronics,” *Advanced Science*, vol. 8, no. 10, p. 2 002 693, 2021.

[36] A Vanhoestenberghe and N Donaldson, “Corrosion of silicon integrated circuits and lifetime predictions in implantable electronic devices,” *Journal of neural engineering*, vol. 10, no. 3, p. 031 002, 2013.

[37] T. D. Y. Kozai, A. L. Vazquez, C. L. Weaver, S.-G. Kim, and X. T. Cui, “In vivo two-photon microscopy reveals immediate microglial reaction to implantation of microelectrode through extension of processes,” *Journal of neural engineering*, vol. 9, no. 6, p. 066 001, 2012.

[38] V. S. Polikov, P. A. Tresco, and W. M. Reichert, "Response of brain tissue to chronically implanted neural electrodes," *Journal of neuroscience methods*, vol. 148, no. 1, pp. 1–18, 2005.

[39] K. Pogoda and P. A. Janmey, "Glial tissue mechanics and mechanosensing by glial cells," *Frontiers in cellular neuroscience*, vol. 12, p. 25, 2018.

[40] A. Fang, Z. Hao, L. Wang, *et al.*, "In vitro model of the glial scar," *International Journal of Bioprinting*, vol. 5, no. 2, 2019.

[41] J. Turner, W Shain, D. Szarowski, *et al.*, "Cerebral astrocyte response to micromachined silicon implants," *Experimental neurology*, vol. 156, no. 1, pp. 33–49, 1999.

[42] C. Marin and E. Fernández, "Biocompatibility of intracortical microelectrodes: Current status and future prospects," *Frontiers in neuroengineering*, p. 8, 2010.

[43] L. Karumbaiah, T. Saxena, D. Carlson, *et al.*, "Relationship between intracortical electrode design and chronic recording function," *Biomaterials*, vol. 34, no. 33, pp. 8061–8074, 2013.

[44] T. G. Schuhmann Jr, T. Zhou, G. Hong, *et al.*, "Syringe-injectable mesh electronics for stable chronic rodent electrophysiology," *JoVE (Journal of Visualized Experiments)*, no. 137, e58003, 2018.

[45] H. S. Sohal, A. Jackson, R. Jackson, *et al.*, "The sinusoidal probe: A new approach to improve electrode longevity," *Frontiers in neuroengineering*, vol. 7, p. 10, 2014.

[46] H. Lee, R. V. Bellamkonda, W. Sun, and M. E. Levenston, "Biomechanical analysis of silicon microelectrode-induced strain in the brain," *Journal of neural engineering*, vol. 2, no. 4, p. 81, 2005.

[47] N. D'Ambrosi and S. Apolloni, "Fibrotic scar in neurodegenerative diseases," *Frontiers in Immunology*, p. 1394, 2020.

[48] S. Singh and N. Joshi, "Astrocytes: Inexplicable cells in neurodegeneration," *International Journal of Neuroscience*, vol. 127, no. 3, pp. 204–209, 2017.

[49] G. Hong, X. Yang, T. Zhou, and C. M. Lieber, "Mesh electronics: A new paradigm for tissue-like brain probes," *Current opinion in neurobiology*, vol. 50, pp. 33–41, 2018.

[50] J. L. Skousen, S. M. E. Merriam, O. Srivannavit, G. Perlin, K. D. Wise, and P. A. Tresco, "Reducing surface area while maintaining implant penetrating profile lowers the brain foreign body response to chronically implanted planar silicon microelectrode arrays," *Progress in brain research*, vol. 194, pp. 167–180, 2011.

[51] S. P. Lacour, G. Courtine, and J. Guck, "Materials and technologies for soft implantable neuroprostheses," *Nature Reviews Materials*, vol. 1, no. 10, pp. 1–14, 2016.

[52] P. Moshayedi, G. Ng, J. C. Kwok, *et al.*, "The relationship between glial cell mechanosensitivity and foreign body reactions in the central nervous system," *Biomaterials*, vol. 35, no. 13, pp. 3919–3925, 2014.

[53] J. K. Nguyen, D. J. Park, J. L. Skousen, *et al.*, "Mechanically-compliant intracortical implants reduce the neuroinflammatory response," *Journal of neural engineering*, vol. 11, no. 5, p. 056 014, 2014.

[54] T. Ware, D. Simon, C. Liu, *et al.*, "Thiol-ene/acrylate substrates for softening intracortical electrodes," *Journal of Biomedical Materials Research Part B: Applied Biomaterials*, vol. 102, no. 1, pp. 1–11, 2014.

[55] T. Ware, D. Simon, D. E. Arreaga-Salas, *et al.*, "Fabrication of responsive, softening neural interfaces," *Advanced Functional Materials*, vol. 22, no. 16, pp. 3470–3479, 2012.

[56] J. P. Seymour and D. R. Kipke, "Neural probe design for reduced tissue encapsulation in cns," *Biomaterials*, vol. 28, no. 25, pp. 3594–3607, 2007.

[57] J. Harris, J. Capadona, R. Miller, *et al.*, "Mechanically adaptive intracortical implants improve the proximity of neuronal cell bodies," *Journal of neural engineering*, vol. 8, no. 6, p. 066 011, 2011.

[58] C.-H. Chen, S.-C. Chuang, H.-C. Su, *et al.*, "A three-dimensional flexible microprobe array for neural recording assembled through electrostatic actuation," *Lab on a Chip*, vol. 11, no. 9, pp. 1647–1655, 2011.

[59] C. P. Foley, K. B. Neeves, W. M. Saltzman, and W. L. Olbricht, "Bioerodible scaffolds for implantable microfluidic probes in convection enhanced neural drug delivery," in *AIChE Annual Meeting*, 2006.

[60] D. Lewitus, K. L. Smith, W. Shain, and J. Kohn, "Ultrafast resorbing polymers for use as carriers for cortical neural probes," *Acta biomaterialia*, vol. 7, no. 6, pp. 2483–2491, 2011.

[61] F. Wu, M. Im, and E. Yoon, "A flexible fish-bone-shaped neural probe strengthened by biodegradable silk coating for enhanced biocompatibility," in *2011 16th International Solid-State Sensors, Actuators and Microsystems Conference*, IEEE, 2011, pp. 966–969.

[62] P. Fattahi, G. Yang, G. Kim, and M. R. Abidian, "A review of organic and inorganic biomaterials for neural interfaces," *Advanced materials*, vol. 26, no. 12, pp. 1846–1885, 2014.

[63] C. L. Kolarcik, D. Bourbeau, E. Azemi, *et al.*, "In vivo effects of l1 coating on inflammation and neuronal health at the electrode–tissue interface in rat spinal cord and dorsal root ganglion," *Acta biomaterialia*, vol. 8, no. 10, pp. 3561–3575, 2012.

[64] L. Rao, H. Zhou, T. Li, C. Li, and Y. Y. Duan, "Polyethylene glycol-containing polyurethane hydrogel coatings for improving the biocompatibility of neural electrodes," *Acta biomaterialia*, vol. 8, no. 6, pp. 2233–2242, 2012.

[65] L. W. Tien, F. Wu, M. D. Tang-Schomer, E. Yoon, F. G. Omenetto, and D. L. Kaplan, "Silk as a multifunctional biomaterial substrate for reduced glial scarring around brain-penetrating electrodes," *Advanced Functional Materials*, vol. 23, no. 25, pp. 3185–3193, 2013.

[66] W. He, G. C. McConnell, T. M. Schneider, and R. V. Bellamkonda, "A novel anti-inflammatory surface for neural electrodes," *Advanced Materials*, vol. 19, no. 21, pp. 3529–3533, 2007.

[67] A. Mercanzini, S. T. Reddy, D. Velluto, *et al.*, "Controlled release nanoparticle-embedded coatings reduce the tissue reaction to neuroprostheses," *Journal of Controlled Release*, vol. 145, no. 3, pp. 196–202, 2010.

[68] D. Bezuidenhout, A. Oosthuysen, N. Davies, *et al.*, "Covalent incorporation and controlled release of active dexamethasone from injectable polyethylene glycol hydrogels," *Journal of Biomedical Materials Research Part A*, vol. 101, no. 5, pp. 1311–1318, 2013.

[69] S. M. Gutowski, J. T. Shoemaker, K. L. Templeman, *et al.*, "Protease-degradable peg-maleimide coating with on-demand release of il-1ra to improve tissue response to neural electrodes," *Biomaterials*, vol. 44, pp. 55–70, 2015.

[70] M. Welkenhuysen, A. Andrei, L. Ameye, W. Eberle, and B. Nuttin, "Effect of insertion speed on tissue response and insertion mechanics of a chronically implanted silicon-based neural probe," *IEEE Transactions on Biomedical Engineering*, vol. 58, no. 11, pp. 3250–3259, 2011.

[71] A. A. Sharp, A. M. Ortega, D. Restrepo, D. Curran-Everett, and K. Gall, "In vivo penetration mechanics and mechanical properties of mouse brain tissue at micrometer scales," *IEEE transactions on biomedical engineering*, vol. 56, no. 1, pp. 45–53, 2008.

[72] A. Jackson and E. E. Fetz, "Compact movable microwire array for long-term chronic unit recording in cerebral cortex of primates," *Journal of neurophysiology*, vol. 98, no. 5, pp. 3109–3118, 2007.

[73] J. C. Williams, R. L. Rennaker, and D. R. Kipke, "Long-term neural recording characteristics of wire microelectrode arrays implanted in cerebral cortex," *Brain Research Protocols*, vol. 4, no. 3, pp. 303–313, 1999.

[74] J. E. Ferguson, C. Boldt, and A. D. Redish, "Creating low-impedance tetrodes by electroplating with additives," *Sensors and Actuators A: Physical*, vol. 156, no. 2, pp. 388–393, 2009.

[75] C. Kim and K. D. Wise, "A 64-site multishank cmos low-profile neural stimulating probe," *IEEE journal of solid-state circuits*, vol. 31, no. 9, pp. 1230–1238, 1996.

[76] K. Najafi, "Solid-state microsensors for cortical nerve recordings," *IEEE engineering in medicine and biology magazine*, vol. 13, no. 3, pp. 375–387, 1994.

[77] S. Schmidt, K. Horch, and R. Normann, "Biocompatibility of silicon-based electrode arrays implanted in feline cortical tissue," *Journal of biomedical materials research*, vol. 27, no. 11, pp. 1393–1399, 1993.

[78] K. D. Wise, D. J. Anderson, J. F. Hetke, D. R. Kipke, and K. Najafi, "Wireless implantable microsystems: High-density electronic interfaces to the nervous system," *Proceedings of the IEEE*, vol. 92, no. 1, pp. 76–97, 2004.

[79] B Fan and W Li, "Miniaturized optogenetic neural implants: A review," *Lab on a Chip*, vol. 15, no. 19, pp. 3838–3855, 2015.

[80] S. Kanno, R. Kobayashi, L. Sanghoon, *et al.*, "Development of si neural probe with microfluidic channel fabricated using wafer direct bonding," *Japanese journal of applied physics*, vol. 48, no. 4S, p. 04C189, 2009.

[81] D. Kipke, "Implantable neural probe systems for cortical neuroprostheses," in *The 26th Annual International Conference of the IEEE Engineering in Medicine and Biology Society*, IEEE, vol. 2, 2004, pp. 5344–5347.

[82] L. R. Hochberg, M. D. Serruya, G. M. Friehs, *et al.*, "Neuronal ensemble control of prosthetic devices by a human with tetraplegia," *Nature*, vol. 442, no. 7099, pp. 164–171, 2006.

[83] S.-P. Kim, J. D. Simeral, L. R. Hochberg, J. P. Donoghue, and M. J. Black, "Neural control of computer cursor velocity by decoding motor cortical spiking activity in humans with tetraplegia," *Journal of neural engineering*, vol. 5, no. 4, p. 455, 2008.

[84] S.-P. Kim, J. D. Simeral, L. R. Hochberg, J. P. Donoghue, G. M. Friehs, and M. J. Black, "Point-and-click cursor control with an intracortical neural interface system by humans with tetraplegia," *IEEE transactions on neural systems and rehabilitation engineering*, vol. 19, no. 2, pp. 193–203, 2011.

[85] R. Bhandari, S. Negi, L. Rieth, M. Topper, R. A. Normann, and F. Solzbacher, "Wafer level processing of silicon arrays for implantable medical devices," in *2007 Proceedings 57th Electronic Components and Technology Conference*, IEEE, 2007, pp. 1567–1572.

[86] J. P. Seymour, F. Wu, K. D. Wise, and E. Yoon, "State-of-the-art mems and microsystem tools for brain research," *Microsystems & Nanoengineering*, vol. 3, no. 1, pp. 1–16, 2017.

[87] P. R. Patel, P. Popov, C. M. Caldwell, *et al.*, "High density carbon fiber arrays for chronic electrophysiology, fast scan cyclic voltammetry, and correlative anatomy," *Journal of Neural Engineering*, vol. 17, no. 5, p. 056 029, 2020.

[88] P. R. Patel, H. Zhang, M. T. Robbins, *et al.*, "Chronic in vivo stability assessment of carbon fiber microelectrode arrays," *Journal of neural engineering*, vol. 13, no. 6, p. 066 002, 2016.

[89] T. Zhou, G. Hong, T.-M. Fu, *et al.*, "Syringe-injectable mesh electronics integrate seamlessly with minimal chronic immune response in the brain," *Proceedings of the National Academy of Sciences*, vol. 114, no. 23, pp. 5894–5899, 2017.

[90] X. Yang, T. Zhou, T. J. Zwang, *et al.*, "Bioinspired neuron-like electronics," *Nature materials*, vol. 18, no. 5, pp. 510–517, 2019.

[91] D. Egert and K. Najafi, "New class of chronic recording multichannel neural probes with post-implant self-deployed satellite recording sites," in *2011 16th International Solid-State Sensors, Actuators and Microsystems Conference*, IEEE, 2011, pp. 958–961.

[92] A. A. Sharp, H. V. Panchawagh, A. Ortega, *et al.*, "Toward a self-deploying shape memory polymer neuronal electrode," *Journal of neural engineering*, vol. 3, no. 4, p. L23, 2006.

[93] R. S. Zoll, C. B. Schindler, T. L. Massey, D. S. Drew, M. M. Maharbiz, and K. S. Pister, "Mems-actuated carbon fiber microelectrode for neural recording," *IEEE transactions on nanobioscience*, vol. 18, no. 2, pp. 234–239, 2019.

[94] C. Pang, Y.-C. Tai, J. W. Burdick, and R. A. Andersen, "Electrolysis-based parylene balloon actuators for movable neural probes," in *2007 2nd IEEE International Conference on Nano/Micro Engineered and Molecular Systems*, IEEE, 2007, pp. 913–916.

[95] H. Park and K. Park, "Hydrogels in bioapplications," in ACS Publications, 1996.

[96] C. Chang, B. Duan, J. Cai, and L. Zhang, "Superabsorbent hydrogels based on cellulose for smart swelling and controllable delivery," *European polymer journal*, vol. 46, no. 1, pp. 92–100, 2010.

[97] P. C. Nicolson and J. Vogt, "Soft contact lens polymers: An evolution," *Biomaterials*, vol. 22, no. 24, pp. 3273–3283, 2001.

[98] J. Li and D. J. Mooney, "Designing hydrogels for controlled drug delivery," *Nature Reviews Materials*, vol. 1, no. 12, pp. 1–17, 2016.

[99] J. Zhu and R. E. Marchant, "Design properties of hydrogel tissue-engineering scaffolds," *Expert review of medical devices*, vol. 8, no. 5, pp. 607–626, 2011.

[100] K. C. Spencer, J. C. Sy, K. B. Ramadi, A. M. Graybiel, R. Langer, and M. J. Cima, "Characterization of mechanically matched hydrogel coatings to improve the biocompatibility of neural implants," *Scientific reports*, vol. 7, no. 1, pp. 1–16, 2017.

[101] X. Le, W. Lu, J. Zhang, and T. Chen, "Recent progress in biomimetic anisotropic hydrogel actuators," *Advanced science*, vol. 6, no. 5, p. 1 801 584, 2019.

[102] C. Ma, X. Le, X. Tang, *et al.*, "A multiresponsive anisotropic hydrogel with macroscopic 3d complex deformations," *Advanced Functional Materials*, vol. 26, no. 47, pp. 8670–8676, 2016.

[103] C. Yao, Z. Liu, C. Yang, *et al.*, “Poly (n-isopropylacrylamide)-clay nanocomposite hydrogels with responsive bending property as temperature-controlled manipulators,” *Advanced Functional Materials*, vol. 25, no. 20, pp. 2980–2991, 2015.

[104] Y. Ma, Y. Zhang, B. Wu, W. Sun, Z. Li, and J. Sun, “Polyelectrolyte multilayer films for building energetic walking devices,” *Angewandte Chemie*, vol. 123, no. 28, pp. 6378–6381, 2011.

[105] X. Zhou, T. Li, J. Wang, *et al.*, “Shape morphing of anisotropy-encoded tough hydrogels enabled by asymmetrically-induced swelling and site-specific mechanical strengthening,” *Journal of Materials Chemistry B*, vol. 6, no. 29, pp. 4731–4737, 2018.

[106] Y. Osada, H. Okuzaki, and H. Hori, “A polymer gel with electrically driven motility,” *Nature*, vol. 355, no. 6357, pp. 242–244, 1992.

[107] M. Bassil, M. Ibrahim, and M. El Tahchi, “Artificial muscular microfibers: Hydrogel with high speed tunable electroactivity,” *Soft Matter*, vol. 7, no. 10, pp. 4833–4838, 2011.

[108] J. Wu, Y. Lin, and J. Sun, “Anisotropic volume change of poly (n-isopropylacrylamide)-based hydrogels with an aligned dual-network microstructure,” *Journal of Materials Chemistry*, vol. 22, no. 34, pp. 17 449–17 451, 2012.

[109] W. R. Illeperuma, J.-Y. Sun, Z. Suo, and J. J. Vlassak, “Force and stroke of a hydrogel actuator,” *Soft Matter*, vol. 9, no. 35, pp. 8504–8511, 2013.

[110] O. Chen and M. M. Maharbiz, “Hydrogel-actuated carbon fiber neural probe,” in *2019 9th International IEEE/EMBS Conference on Neural Engineering (NER)*, IEEE, 2019, pp. 879–882.

[111] M.-c. Lo, S. Wang, S. Singh, *et al.*, “Evaluating the in vivo glial response to miniaturized parylene cortical probes coated with an ultra-fast degrading polymer to aid insertion,” *Journal of neural engineering*, vol. 15, no. 3, p. 036 002, 2018.

[112] T. L. Massey, S. R. Santacruz, J. F. Hou, K. S. Pister, J. M. Carmena, and M. M. Maharbiz, “A high-density carbon fiber neural recording array technology,” *Journal of neural engineering*, vol. 16, no. 1, p. 016 024, 2019.

[113] R. K. Bose and K. K. Lau, “Mechanical properties of ultrahigh molecular weight phema hydrogels synthesized using initiated chemical vapor deposition,” *Biomacromolecules*, vol. 11, no. 8, pp. 2116–2122, 2010.

[114] S. H. Baxamusa, L. Montero, J. M. Dubach, H. A. Clark, S. Borros, and K. K. Gleason, “Protection of sensors for biological applications by photoinitiated chemical vapor deposition of hydrogel thin films,” *Biomacromolecules*, vol. 9, no. 10, pp. 2857–2862, 2008.

[115] K. Baysal, A. Z. Aroguz, Z. Adiguzel, and B. M. Baysal, “Chitosan/alginate crosslinked hydrogels: Preparation, characterization and application for cell growth purposes,” *International journal of biological macromolecules*, vol. 59, pp. 342–348, 2013.

[116] C. K. Kuo and P. X. Ma, "Ionically crosslinked alginate hydrogels as scaffolds for tissue engineering: Part 1. structure, gelation rate and mechanical properties," *Biomaterials*, vol. 22, no. 6, pp. 511–521, 2001.

[117] S. S. Co., *Spray performance data*, Brochure. [Online]. Available: `http://www.telespazio.it/docs/brodoc/GCC_eng.pdf`.

[118] H. Chandrakumar and D. Marković, "An 80-mvpp linear-input range, 1.6-gΩ input impedance, low-power chopper amplifier for closed-loop neural recording that is tolerant to 650-mvpp common-mode interference," *IEEE Journal of Solid-State Circuits*, vol. 52, no. 11, pp. 2811–2828, 2017.

[119] H. Chandrakumar and D. Marković, "5.5 a 2μw 40mvpp linear-input-range chopper-stabilized bio-signal amplifier with boosted input impedance of 300mΩ and electrode-offset filtering," in *2016 IEEE international solid-state circuits conference (ISSCC)*, IEEE, 2016, pp. 96–97.

[120] J. P. Neto, P. Baião, G. Lopes, *et al.*, "Does impedance matter when recording spikes with polytrodes?" *Frontiers in neuroscience*, vol. 12, p. 715, 2018.

[121] W. Franks, I. Schenker, P. Schmutz, and A. Hierlemann, "Impedance characterization and modeling of electrodes for biomedical applications," *IEEE Transactions on Biomedical Engineering*, vol. 52, no. 7, pp. 1295–1302, 2005.

[122] J. Kang, J. Wen, S. H. Jayaram, A. Yu, and X. Wang, "Development of an equivalent circuit model for electrochemical double layer capacitors (edlcs) with distinct electrolytes," *Electrochimica Acta*, vol. 115, pp. 587–598, 2014.

[123] R. Nelms, D. Cahela, and B. J. Tatarchuk, "Modeling double-layer capacitor behavior using ladder circuits," *IEEE Transactions on Aerospace and Electronic Systems*, vol. 39, no. 2, pp. 430–438, 2003.

[124] V. Lockett, M. Horne, R. Sedev, T. Rodopoulos, and J. Ralston, "Differential capacitance of the double layer at the electrode/ionic liquids interface," *Physical Chemistry Chemical Physics*, vol. 12, no. 39, pp. 12 499–12 512, 2010.

[125] M. J. Nelson, P. Pouget, E. A. Nilsen, C. D. Patten, and J. D. Schall, "Review of signal distortion through metal microelectrode recording circuits and filters," *Journal of neuroscience methods*, vol. 169, no. 1, pp. 141–157, 2008.

[126] N. V. Gupta and H. Shivakumar, "Investigation of swelling behavior and mechanical properties of a ph-sensitive superporous hydrogel composite," *Iranian journal of pharmaceutical research: IJPR*, vol. 11, no. 2, p. 481, 2012.

[127] P. J. Flory and J. Rehner Jr, "Statistical mechanics of cross-linked polymer networks i. rubberlike elasticity," *The journal of chemical physics*, vol. 11, no. 11, pp. 512–520, 1943.

[128] S. K. Fifanski, J. L. Rivera Gutiérrez, M. Clogenson, *et al.*, “Flexure-based multi-degrees-of-freedom in-vivo force sensors for medical instruments,” *Proceedings of Euspen 2016*, vol. 1, no. CONF, pp. 333–334, 2016.

[129] T. O. Akinyemi, O. M. Omisore, W. Duan, *et al.*, “Development of a millinewton fbg-based distal force sensor for intravascular interventions,” in *2020 16th International Conference on Control, Automation, Robotics and Vision (ICARCV)*, IEEE, 2020, pp. 511–515.

[130] C. B. Schindler, H. C. Gomez, D. Acker-James, D. Teal, W. Li, and K. S. Pister, “15 millinewton force, 1 millimeter displacement, low-power mems gripper,” in *2020 IEEE 33rd International Conference on Micro Electro Mechanical Systems (MEMS)*, IEEE, 2020, pp. 485–488.

[131] W. Chen, J. Jiang, J. Liu, and W. Chen, “A mems based sensor for large scale force measurement,” in *2013 IEEE/ASME International Conference on Advanced Intelligent Mechatronics*, IEEE, 2013, pp. 1278–1283.

[132] W. C. Young, R. G. Budynas, and A. M. Sadegh, *Roark’s formulas for stress and strain.* McGraw-Hill Education, 2012.

[133] R. G. Kelly, J. R. Scully, D. Shoesmith, and R. G. Buchheit, *Electrochemical techniques in corrosion science and engineering.* CRC Press, 2002.

[134] Y. Qiang, W. Gu, Z. Liu, *et al.*, “Crosstalk in polymer microelectrode arrays,” *Nano research*, vol. 14, no. 9, pp. 3240–3247, 2021.

[135] G. Rios, E. V. Lubenov, D. Chi, M. L. Roukes, and A. G. Siapas, “Nanofabricated neural probes for dense 3-d recordings of brain activity,” *Nano letters*, vol. 16, no. 11, pp. 6857–6862, 2016.

[136] A. Wang, D. Jung, D. Lee, and H. Wang, “Impedance characterization and modeling of subcellular to micro-sized electrodes with varying materials and pedot: Pss coating for bioelectrical interfaces,” *ACS Applied Electronic Materials*, vol. 3, no. 12, pp. 5226–5239, 2021.

[137] R. G. Budynas and A. M. Sadegh, *Roark’s formulas for stress and strain.* McGraw-Hill Education, 2020.

[138] N. Geramifard, B. Dousti, C. Nguyen, J. Abbott, S. F. Cogan, and V. D. Varner, “Insertion mechanics of amorphous sic ultra-micro scale neural probes,” *Journal of Neural Engineering*, vol. 19, no. 2, p. 026 033, 2022.

[139] R. Fiáth, A. L. Márton, F. Mátyás, *et al.*, “Slow insertion of silicon probes improves the quality of acute neuronal recordings,” *Scientific reports*, vol. 9, no. 1, pp. 1–17, 2019.

[140] M. Felisberto, L. Tzounis, L. Sacco, *et al.*, "Carbon nanotubes grown on carbon fiber yarns by a low temperature cvd method: A significant enhancement of the interfacial adhesion between carbon fiber/epoxy matrix hierarchical composites," *Composites Communications*, vol. 3, pp. 33–37, 2017.

[141] Y. M. Manawi, A. Samara, T. Al-Ansari, and M. A. Atieh, "A review of carbon nanomaterials' synthesis via the chemical vapor deposition (cvd) method," *Materials*, vol. 11, no. 5, p. 822, 2018.

[142] E. Musk *et al.*, "An integrated brain-machine interface platform with thousands of channels," *Journal of medical Internet research*, vol. 21, no. 10, e16194, 2019.

[143] T. L. Massey, J. H. Lee, M. Ray, *et al.*, "Open-source automated system for assembling a high-density microwire neural recording array," in *2016 International Conference on Manipulation, Automation and Robotics at Small Scales (MARSS)*, IEEE, 2016, pp. 1–7.

[144] A. M. Rauf, D. S. Contreras, R. M. Shih, C. B. Schindler, and K. S. Pister, "Nonlinear dynamics of lateral electrostatic gap closing actuators for applications in inchworm motors," *Journal of Microelectromechanical Systems*, vol. 31, no. 1, pp. 29–36, 2021.